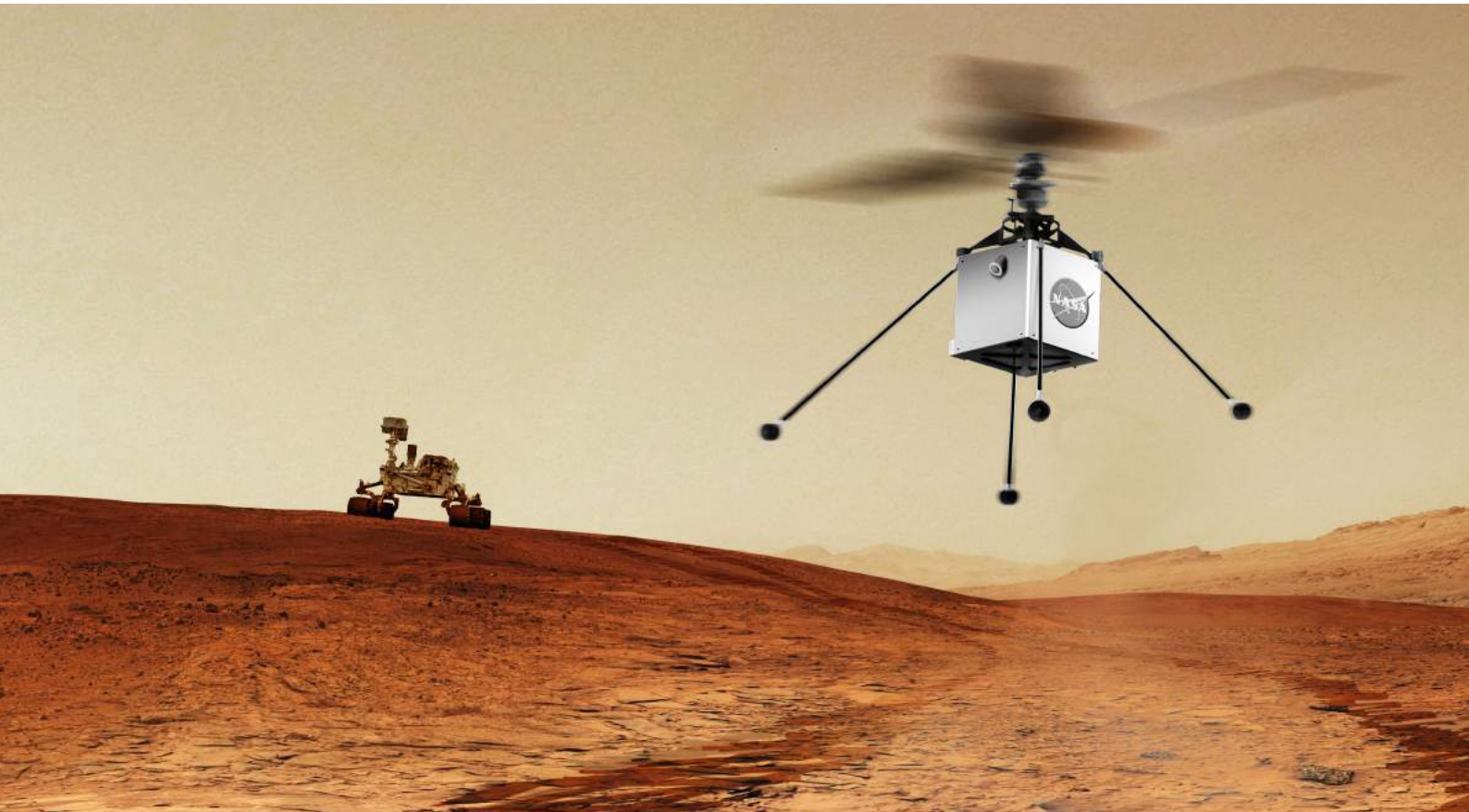




**CHALMERS**  
UNIVERSITY OF TECHNOLOGY

---



# **Experimental and Computational Evaluation of Capabilities of Predicting Aerodynamic Performance for a Mars Helicopter Rotor**

Master's thesis in Applied Mechanics

**MARCUS JOHANSSON**

---

Department of Applied Mechanics  
CHALMERS UNIVERSITY OF TECHNOLOGY  
Gothenburg, Sweden 2017



MASTER'S THESIS 2017:44

**Experimental and Computational Evaluation  
of Capabilities of Predicting Aerodynamic  
Performance for a Mars Helicopter Rotor**

MARCUS JOHANSSON



**CHALMERS**  
UNIVERSITY OF TECHNOLOGY

Department of Applied Mechanics  
*Division of Fluid Mechanics*  
CHALMERS UNIVERSITY OF TECHNOLOGY  
Gothenburg, Sweden 2017

Experimental and Computational Evaluation of Capabilities of Predicting Aerodynamic Performance for a Mars Helicopter Rotor

MARCUS JOHANSSON

© MARCUS JOHANSSON, 2017.

Supervisor: Dr. William Warmbrodt, Department of Aeromechanics, NASA Ames Research Center, Moffett Field, California

Examiner: Lars Davidson, Department of Applied Mechanics

Master's Thesis 2017:44  
Department of Applied Mechanics  
Division of Fluid Mechanics  
Chalmers University of Technology  
SE-412 96 Gothenburg  
Telephone +46 31 772 1000

Cover: Artist's impression of the Mars Helicopter Scout operating at Mars. Courtesy NASA/JPL-Caltech.

Typeset in L<sup>A</sup>T<sub>E</sub>X  
Printed by Chalmers Reproservice  
Gothenburg, Sweden 2017

# Experimental and Computational Evaluation of Capabilities of Predicting Aerodynamic Performance for a Mars Helicopter Rotor

MARCUS JOHANSSON

Department of Applied Mechanics  
Chalmers University of Technology

## **Abstract**

The interest in behavior and performance of autonomous rotary-wing aerial vehicles for Mars exploration has grown vastly. Exploring the challenging conditions will benefit both future planetary aerial vehicle missions as well as pushing the threshold of performance further for high tech aerodynamic vehicles on Earth.

This report describes a validated set of analysis tools for designing future Mars planetary vertical lift unmanned aircraft for various missions. The procedure involved experimental test campaigns under simulated Mars atmospheric conditions to further use the test data to correlate with analytical predictions using design tools currently being used by the rotorcraft community. The goal has been to understand the capability of the CFD analysis tool RotCFD to predict rotor aerodynamics under high Mach number and low Reynolds number circumstances with thrust variances at various pressures ranging from Terrestrial conditions down to 7 millibar corresponding to the Martian atmosphere.

The experimental test campaign has focused on forward flight rotor performance for a Mars Helicopter rotor. Due to Mars's different nature, as credible testing as possible was performed in the Martian Aeolian Wind Tunnel located in the Planetary Aeolian Laboratory at NASA Ames Research Center.

Keywords: Mars, Helicopter, Rotor, NASA, Aerodynamic, RotCFD



# Acknowledgements

To begin with, I want to direct my gratitude to Christer Fuglesang, first and only Swedish astronaut who initially hinted me about the International Intern (I<sup>2</sup>) program and the rest of the Swedish National Space Agency (SNSB). Without their advice and support, I would never had this extraordinary opportunity to go to NASA. Also I want to thank all people not to be mentioned in this acknowledgement that has been involved in my work and that I have met during my stay in the US. You all made my stay unique and joyful.

I want to emphasize gratitude to Kristen Kallstrom who always keeps the spirits of everyone in the Aeromechanics department up, organizing department trips that made the internship unforgettable and a memorable experience. Always supporting everyone despite her hectic life, combining work and studies.

Witold Koning, the person involved in every project at the department but still took time off to help me with my work. He possesses a self discipline I admire; from distinguished hard work to later turn completely over and being the joker in the group, as a combination lifting both work discipline and friendship at the department.

What would the department do without Geoff Ament? With a willingness to help others, sacrificing his own free time and staying late nights to help me and other interns on the department, he pushes experimental work on the department forward in a pace I wish everyone would be capable of.

A big shout-out to my old classmate, room mate, friend, and colleague Kasper Janehag, who supported me throughout the internship and my thesis work. Our intense and never-ending discussions that switched in the twinkle from deep scientific stuff to personal subjects, gave the internship that little extra.

I want to express my biggest gratitude lastly to Dr. William Warmbrodt, Chief of the Aeromechanics Branch at NASA Ames, that supported me from the first day. Despite his responsibility as Chief of the branch, we had hours of long interactions, to guide me throughout my internship and thesis. With huge knowledge and an ability always knowing what is the next step for me, you have been extraordinary valuable for me and without you, my thesis would never be.

Marcus Johansson, Gothenburg, June 2017



# Nomenclature

Symbols	Description	Unit (metric)
$A$	Projected wing area	$[m^2]$
$A_0$	Upper control surface, helicopter flow field	$[m^2]$
$A_\infty$	Lower control surface, helicopter flow field	$[m^2]$
$c$	Chord	$[m]$
$C_{d0}$	Profile drag coefficient	$[-]$
$C_d$	Sectional drag coefficient	$[-]$
$C_D$	Drag coefficient	$[-]$
$C_l$	Sectional lift coefficient	$[-]$
$C_L$	Lift coefficient	$[-]$
$C_m$	Sectional pitching moment coefficient	$[-]$
$C_M$	Pitching moment coefficient	$[-]$
$C_P$	Power coefficient	$[-]$
$C_{P0}$	Profile power coefficient	$[-]$
$C_Q$	Rotor shaft torque coefficient	$[-]$
$D$	Profile drag	$[N]$
$F_D$	Drag force	$[N]$
$F_L$	Lift force	$[N]$
$G$	Gravitational constant	$[m^3/kg s^2]$
$g$	Gravitational acceleration	$[m/s^2]$
$k$	Turbulent kinetic energy	$[J/kg]$
$L_c$	Characteristic length scale	$[m]$
$L_s$	Length domain in streamwise direction	$[m]$
$M_x$	Roll moment	$[Nm]$
$M_y$	Pitching moment	$[Nm]$
$m$	Mass	$[kg]$
$\dot{m}$	Mass flow	$[kg/s]$
$N_b$	Number of blades	$[-]$
$n_{cs}$	Number of cells in streamwise direction	$[-]$
$P$	Rotor power	$[W]$
$p$	Pressure	$[Pa]$
$p_\infty$	Free flow fluid pressure	$[Pa]$
$Q$	Torque	$[Nm]$
$q$	Dynamic pressure	$[Pa]$
$r$	Radial station	$[m]$
$r_{ref}$	Refinement level	$[-]$
$R$	Rotor radius	$[m]$
$R_{spec}$	Specific gas constant	$[J/kgK]$
$Re$	Reynolds number	$[-]$
$T$	Rotor thrust	$[N]$
$t$	Time	$[s]$
$u_1$	Velocity in $x$ -direction	$[m/s]$
$u_2$	Velocity in $y$ -direction	$[m/s]$

---

<b>Symbols</b>	<b>Description</b>	<b>Unit (metric)</b>
$u_3$	Velocity in $z$ -direction	$[m/s]$
$V_c$	Helicopter vertical velocity	$[m/s]$
$V_h$	Rotor induced velocity	$[m/s]$
$V_\infty$	Free field velocity	$[m/s]$
$V_{tip}$	Wing tip velocity	$[m/s]$
$w$	Wake velocity	$[m/s]$

<b>Greek symbols</b>	<b>Description</b>	<b>Unit (metric)</b>
$\alpha$	Angle of Attack	$[^\circ]$
$\epsilon$	Turbulent Dissipation	$[J/kg s]$
$\gamma$	Specific Heat Ratio	$[-]$
$\kappa$	Induced power correction factor	$[-]$
$\lambda_h$	Induced flow ratio coefficient	$[-]$
$\phi$	Instantaneous flow variable	$[-]$
$\phi'$	Fluctuating part flow variable	$[-]$
$\bar{\phi}$	Mean part flow variable	$[-]$
$\Omega$	Angular velocity	$[rad/s]$
$\theta_{Btw}$	Built-in twist	$[^\circ]$
$\mu$	Dynamic viscosity	$[kg/ms]$
$\nu$	Kinematic viscosity	$[m^2/s]$
$\rho$	Density	$[kg/m^3]$
$\sigma$	Solidity Ratio	$[-]$
$\tau$	Viscous shear stress	$[N/m^2]$

<b>Abbreviations</b>	<b>Description</b>
BEM	Blade Element Model
C81 Gen	C81 Generator
CFD	Computational Fluid Dynamics
CFL	Courant–Friedrichs–Lewy
FM	Figure of Merit
JPL	Jet Propulsion Laboratory
LC	Load Cell
MAWT	Martian Aeolian Wind Tunnel
MHS	Mars Helicopter Scout
NASA	National Aeronautics and Space Administration
NS	Navier-Stokes
PAL	Planetary Aeolian Laboratory
RANS	Reynolds Averaged Navier-Stokes
RPM	Revolutions Per Minute
RotCFD	Rotorcraft Computational Fluid Dynamics
RotUNS	RotCFD Unstructured solver
SIMPLE	Semi-Implicit Method for Pressure-Linked Equations
TDN	Thrust Down
TUP	Thrust Up

# Contents

<b>List of Figures</b>	<b>xiii</b>
<b>List of Tables</b>	<b>xvii</b>
<b>1 Introduction</b>	<b>1</b>
1.1 Mars Helicopter Flight in Martian Atmosphere . . . . .	1
1.2 Purpose and goal . . . . .	3
1.3 Clarifications . . . . .	3
<b>2 Literature Study and Background</b>	<b>5</b>
2.1 Computational Fluid Dynamics . . . . .	5
2.1.1 Reynolds Averaged Navier-Stokes equations (RANS) . . . . .	6
2.2 Helicopter Hover Momentum Theory . . . . .	7
2.2.1 Non ideal effects . . . . .	10
2.3 Rotorcraft Comtutational Fluid Dynamics . . . . .	11
2.3.1 RotUNS - Flow Solver . . . . .	12
2.3.2 RotCFD Rotor Model . . . . .	12
2.3.3 Rotor Disc Fixed Cartesian system . . . . .	13
2.3.4 Rotor Based Cylindrical Polar System . . . . .	13
<b>3 Simulating Martian Flight on Earth</b>	<b>15</b>
3.1 Difficulties and limitations . . . . .	15
3.1.1 Gravity . . . . .	16
3.1.2 Pressure and Density . . . . .	16
3.1.3 Reynolds number . . . . .	17
3.1.4 Atmospheric composition . . . . .	17
3.1.5 Temperature . . . . .	18
3.1.6 JPL 25-ft Space Simulator . . . . .	18
<b>4 Aeolian Wind Tunnel Testing</b>	<b>21</b>
4.1 Facility Description . . . . .	21
4.2 Mars Rotor Test Configuration . . . . .	22
4.2.1 Rotor selection . . . . .	23
4.3 Measurements . . . . .	25
4.3.1 Thrust . . . . .	25
4.3.2 Chamber temperature and pressure . . . . .	27

4.3.3	Accelerometers . . . . .	27
4.3.4	Data Acquisition . . . . .	28
4.4	Test Procedure . . . . .	29
4.5	Test Matrix . . . . .	29
<b>5</b>	<b>Load Cell Validation</b>	<b>31</b>
5.1	Weight tare validation . . . . .	34
<b>6</b>	<b>Numerical Prediction of Rotor Performance</b>	<b>37</b>
6.1	Grid Generation . . . . .	37
6.1.1	Time grid . . . . .	37
6.1.2	Domain size . . . . .	38
6.2	Airfoil Tables . . . . .	41
6.2.1	Angle of Attack . . . . .	42
6.2.2	Lift coefficient . . . . .	42
6.2.3	Drag coefficient . . . . .	43
6.2.4	Moment coefficient . . . . .	43
6.3	RotCFD Setup . . . . .	43
6.3.1	Flow properties . . . . .	44
6.3.2	Boundary conditions . . . . .	44
6.4	Correlation Matrix . . . . .	45
<b>7</b>	<b>Results</b>	<b>47</b>
7.1	Experimental Results . . . . .	47
7.1.1	Load cell drifts . . . . .	47
7.1.2	Pressure effects . . . . .	52
7.1.3	Temperature effects . . . . .	55
7.2	RotCFD Results . . . . .	56
7.2.1	Airfoil Tables comparison . . . . .	57
7.2.2	Airfoil tables validation . . . . .	58
7.2.3	Free field hover . . . . .	59
7.2.4	Tunnel effects . . . . .	62
7.3	Wind tunnel correlation . . . . .	63
<b>8</b>	<b>Conclusions and Recommendations</b>	<b>67</b>
8.1	Conclusions . . . . .	67
8.2	Recommendations . . . . .	68
	<b>Bibliography</b>	<b>69</b>
<b>A</b>	<b>Appendix 1 - RotCFD Run Overview</b>	<b>I</b>
A.1	1013 millibar, free field - rpm sweep . . . . .	II
A.2	Airfoil Tables comparison . . . . .	VII
<b>B</b>	<b>Appendix 2 - Airfoil Tables Validation</b>	<b>XI</b>
B.1	Free field hover . . . . .	XI
B.2	Airfoil comparison . . . . .	XIV
B.3	Tunnel effects . . . . .	XV

# List of Figures

1.1	Point design of the Mars Helicopter Scout [13]. . . . .	2
2.1	Notations of a helicopter in hover flight [4] . . . . .	8
2.2	Flow fields, pressure and velocity distribution [4] . . . . .	9
3.1	Atmospheric composition comparison - Earth and Mars [13] . . . . .	18
3.2	Temperature comparison - Earth and Mars [13] . . . . .	18
4.1	MAWT test configuration . . . . .	22
4.2	Rotational motor stand . . . . .	23
4.3	Mounting the rotors . . . . .	23
4.4	3D model of 40x22 propeller . . . . .	24
4.5	Chord distribution along the radius of the blade, 40x22 Propeller . . . . .	24
4.6	Twist distribution along the radius of the blade, 40x22 Propeller . . . . .	25
4.7	Load cell positions and coordinate system definition. . . . .	26
4.8	Mounting load cells to the motor hub. . . . .	27
4.9	Static banking test . . . . .	28
5.1	50 pounds in load stacked on the hub . . . . .	32
5.2	Repeatability analysis. Total load, stacking weights on the hub . . . . .	33
5.3	Repeatability analysis. Individual load cell gain, stacking weights on the hub . . . . .	33
5.4	Weight tares for each load cell, rotor shaft angle changing within the range -14 to 15 degrees. . . . .	35
6.1	Grid used for free field simulations, side view . . . . .	39
6.2	Grid used for free field simulations, top view . . . . .	40
6.3	Grid used mimicking the wind tunnel simulation, side view . . . . .	40
6.4	Grid used mimicking the wind tunnel simulation, front view . . . . .	41
6.5	Angle of attack visualization [15] . . . . .	42
7.1	Thrust against pressure. <i>Left:</i> Corrected load cell and thrust zero points. <i>Right:</i> Uncorrected individual load cell zero points. . . . .	48
7.2	Thrust against motor temperature, heat run - run 71 . . . . .	49
7.3	Thrust drift during RPM sweep at 7 millibar . . . . .	50
7.4	Thrust against motor temperature. <i>Left:</i> Corrected load cell and thrust zero points. <i>Right:</i> Uncorrected individual load cell zero points. . . . .	51

7.5	Thrust against chamber temperature. <i>Left</i> : Corrected load cell and thrust zero points. <i>Right</i> : Uncorrected individual load cell zero points.	51
7.6	Depressurization, total thrust, 2 prop., 1250 RPM . . . . .	52
7.7	Depressurization, rate of change in thrust against pressure, 2 prop., TUP, 1250 RPM . . . . .	53
7.8	Thrust variation during low pressure RPM sweeps . . . . .	54
7.9	Thrust variation during low pressure RPM sweeps, zero pt. correction every RPM sweep . . . . .	55
7.10	Temperature against pressure when pumping down and held pressure constant at 7 millibar . . . . .	56
7.11	Over time averaged angle of attack, blade 1 and blade 2. . . . .	59
7.12	Velocity vectors with pressure contours between the rotors, free field hover . . . . .	60
7.13	Velocity vectors with pressure contours from side, free field hover . . . . .	60
7.14	Free field, hover RPM sweep, RotCFD . . . . .	61
7.15	Velocity magnitude visualization, free field hover . . . . .	62
7.16	Velocity magnitude at $p=13.73$ millibar, $t=4$ s, $\alpha = 14^\circ$ , $V_\infty=3.5$ m/s, 3000 RPM . . . . .	63
7.17	Velocity vectors with pressure contours at $p=13.73$ millibar, $t=4$ s, $\alpha = 14^\circ$ , $V_\infty=3.5$ m/s, 3000 RPM . . . . .	64
7.18	Experimental and numerical thrust prediction, tunnel at low pressure, RPM sweep, RotCFD . . . . .	65
A.1	2 props, free field, $p = 1013$ mbar, $RPM = 1868$ , $\alpha = 0^\circ$ . . . . .	II
A.2	2 props, free field, $p = 1013$ mbar, $RPM = 2100$ , $\alpha = 0^\circ$ . . . . .	III
A.3	2 props, free field, $p = 1013$ mbar, $RPM = 2500$ , $\alpha = 0^\circ$ . . . . .	IV
A.4	2 props, free field, $p = 1013$ mbar, $RPM = 2800$ , $\alpha = 0^\circ$ . . . . .	V
A.5	2 props, free field, $p = 1013$ mbar, $RPM = 3000$ , $\alpha = 0^\circ$ . . . . .	VI
A.6	2 props, free field, $p = 7$ millibar, $RPM = 3000$ , $\alpha = 0^\circ$ . . . . .	VII
A.7	2 props, free field, $p = 7$ millibar, $RPM = 3000$ , $\alpha = 0^\circ$ , using 1013 mbar irfoil tables . . . . .	VIII
A.8	2 props, free field, $p = 1013$ millibar, $RPM = 3000$ , $\alpha = 0^\circ$ , using 7 mbar airfoil tables . . . . .	IX
B.1	Angle of attack plot for a free field simulation at $p =1013$ millibar, 1868 RPM . . . . .	XI
B.2	Angle of attack plot for a free field simulation at $p =1013$ millibar, 2100 RPM . . . . .	XII
B.3	Angle of attack plot for a free field simulation at $p =1013$ millibar, 2500 RPM . . . . .	XII
B.4	Angle of attack plot for a free field simulation at $p =1013$ millibar, 2800 RPM . . . . .	XIII
B.5	Angle of attack plot for a free field simulation at $p =1013$ millibar, 3000 RPM . . . . .	XIII
B.6	Angle of attack plot for a free field simulation at $p =1013$ millibar using 7 millibar airfoil tables, 3000 RPM . . . . .	XIV

---

B.7	Angle of attack plot for a free field simulation at $p = 7$ millibar using 7 millibar airfoil tables, 3000 RPM . . . . .	XIV
B.8	Angle of attack plot for a free field simulation at $p = 1013$ millibar using 1013 millibar airfoil tables, 3000 RPM . . . . .	XV
B.9	Angle of attack plot for a free field simulation at $p = 7$ millibar, $\alpha = 14^\circ$ , $V_\infty = 3.5$ m/s, 3000 RPM . . . . .	XV
B.10	Angle of attack plot for a tunnel simulation at $p = 7$ millibar, $\alpha = 14^\circ$ , $V_\infty = 3.5$ m/s, 3000 RPM . . . . .	XVI



# List of Tables

6.1	Terrestrial flow properties . . . . .	44
6.2	Martian flow properties . . . . .	44
6.3	Correlation matrix, experimental data to be compared to numerical .	45
7.1	Airfoil comparison, free field hover at $p = 7mbar$ , 3000 RPM . . . . .	57
7.2	Airfoil comparison, hover at $p = 1013mbar$ , 3000 RPM . . . . .	58
7.3	Thrust at various rotor speeds, free field hover at $p = 1013 mbar$ . . .	61
7.4	Tunnel effects, $V_\infty=3.5$ m/s at $p = 7mbar$ , 3000 RPM . . . . .	63
7.5	Correlation study, including numerical predicted thrust . . . . .	64



# 1

## Introduction

Exploring Mars and putting mankind on another planet has been an ongoing discussion and goal since the 1950's. Planning human missions has been undertaken multiple times by organizations and space agencies worldwide. Scientists have speculated whether terraformation is possible and how to utilize both Mars's surface and its moons Phobos and Deimos. Currently Curiosity and Opportunity perform ongoing research on Mars and the next exploration milestone is the Mars 2020 rover, hopefully with support from the Mars Helicopter Scout.

### 1.1 Mars Helicopter Flight in Martian Atmosphere

Mars's challenging environment comes with large temperature changes, sandstorms, and a challenging surface composition which yields many unreachable spots for Mars rovers to date. The Mars helicopters main purpose is, besides a proof-of-concept to prove the ability to generate enough lift to fly autonomously on Mars, map the surrounding terrain, equipped with a high-resolution camera to provide simplifications of road choices for current and future rover missions. If the mission is successful, it could benefit both future planetary aerial vehicle missions as well push the threshold of performance further of high tech aerodynamic vehicles on Earth. Fig.(1.1) describes the MHS design and functions.

## 1. Introduction

---

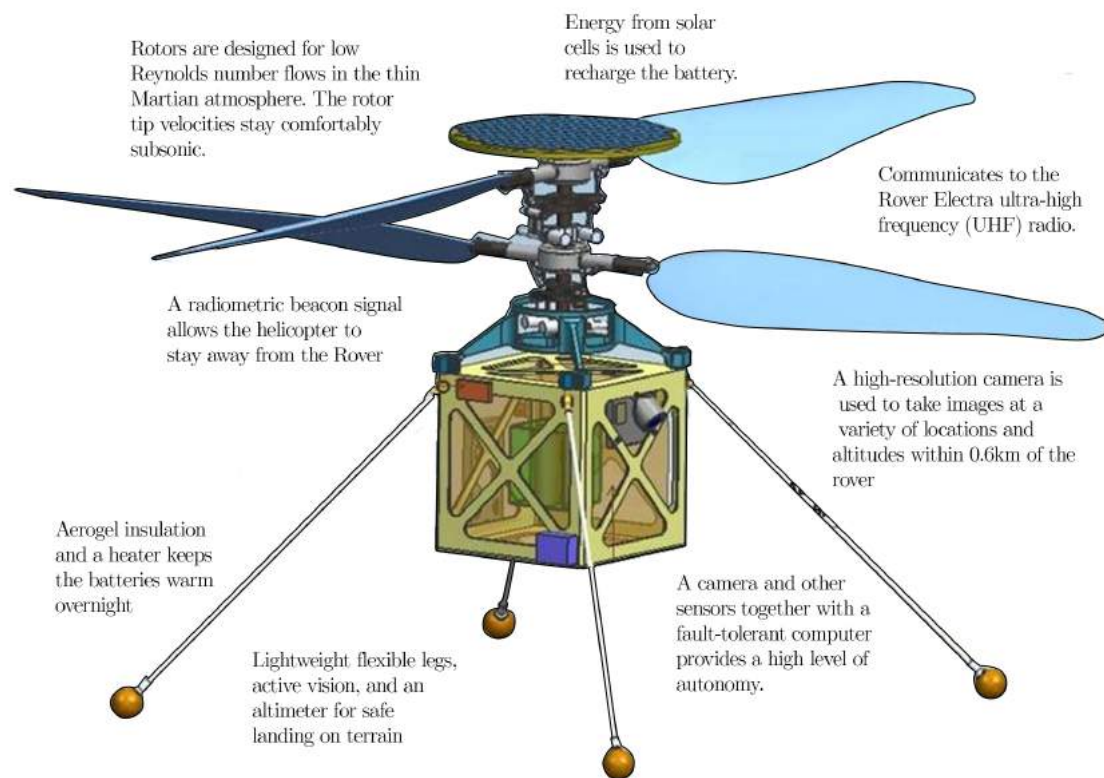


**Figure 1.1:** Point design of the Mars Helicopter Scout [13].

The Mars Helicopter rotor will operate under high Mach number and low Reynolds numbers conditions on Mars. For a rotor, it is critical that subsonic velocities are maintained, strong shock waves can cause serious damage to the rotor blades and make lift production inefficient. Due to the thin atmosphere on Mars, wing tip velocities stays subsonic and the requirement of high rotational speed of the rotors on Mars will not be an issue. The symmetrical designed Mars Helicopter with its co-axial rotor system will autonomously use upper and lower collective and a lower cyclic to navigate forward. The reduced gravity improves the stability of the helicopter and hence reduces the frequency of unstable phugoids and translational sensitivity to gusting [17]. With a proposed rotor diameter of approximately 1.2 meters and a total weight of about 1.7 kilograms, the size of the rotor will be large relative fuselage and body. The MHS is supposed to fly 1-2 minutes a day with a top of climb of 5 meters, using a solar powered system. Remaining non-operative time it will stand on the ground and recharge its batteries. It is purposed to fly on less gusty days to avoid sandstorms since wind is the number one challenge on Mars. Wind creates faster instabilities and necessitates control deflections [17]. As a proof of concept, the helicopter is purposed to give understanding whether there is flying capabilities on Mars and therefore has to be extremely lightweight and little room left for redundancy.

## 1.2 Purpose and goal

The main goal of the research is to conduct experimental low pressure wind tunnel tests and evaluate the validity of data acquired to predict the aerodynamic performance of a Mars rotor. The conducted experimental test campaigns are performed under various pressures, ranging from Earth's atmospheric conditions to corresponding Mars pressure - 7 millibar.

Additionally, aim towards is also evaluating possibilities to reproduce experimental data with numerical predictions, using design tools currently being used by the rotorcraft community. The purpose of this research is to contribute to a better knowledge for designing future Mars planetary vertical lift unmanned aircrafts for different missions.

## 1.3 Clarifications

The rotor that has been used is not the same rotor nor have the same design as the rotor that will go to Mars in 2020. Also, the used hardware setup are not able to simulate a co-axial rotor configuration as well collective and cyclic controls. Hence, results conducted are to be compared relatively. Thus, this research will not conclude whether the Mars Helicopter Scout is capable of flying on Mars or not!



# 2

## Literature Study and Background

A brief introduction to the related theory of fluid mechanics and helicopters is necessary. The Mars Helicopter is proposed to operate under incompressible conditions, thus the incompressible set of Navier-Stokes equations applies. For numerical prediction, CFD software RotCFD was used which uses a flow solver based on Reynolds Averaged Navier-Stokes (RANS) set of equations to resolve the flow for numerical solutions. To implement momentum generated by the spinning rotors, RotCFD uses momentum sources, why the momentum theory is described in detail.

### 2.1 Computational Fluid Dynamics

Computational Fluid Dynamics (CFD) is solely based on the Navier-Stokes set of partial differential equations whose main purpose is, through numerical solutions, simulate flow behavior and its interactions with solid bodies. This will help the user to get a perception of fluid mechanical experiments, without actually performing the experiment in reality. A huge advantage from an economical and time perspective. With time the computers computational power has increased vastly, good enough that CFD has become a very common tool in fluid mechanics communities.

The Navier-Stokes set of equations are since long known and describe the evolution equation of the instantaneous velocities  $u_i(x_i, t)$  and the instantaneous pressure  $p(x_i, t)$ . Based on three simple physical phenomenons, conservation of mass, Newton's second law and the conservation of energy, Navier-Stokes equations creates a closed set of partial differential equations. Flow solver RotUNS is developed for incompressible flows where it is sufficient to use the conservation of mass and momentum to solve for primary flow variables - velocity and pressure. The energy equation is only necessary in compressible flow simulations and will not be further discussed.

Mass can never be destroyed nor created and when incompressibility condition applies, net flow in each control volume in the grid is assumed to equal the net flow out.

$$\frac{\partial \rho}{\partial t} + \frac{\partial}{\partial x_i}(\rho u_i) = 0 \quad (2.1)$$

Eq.(2.1) is referred to as the continuity equation and is stated using index notation where  $i = 1, 2, 3$ . Since the flow is assumed to be incompressible, density do not change over time,  $\frac{\partial \rho}{\partial t} = 0$ , and the final mass equation becomes

$$\frac{\partial u_i}{\partial x_i} = 0 \quad (2.2)$$

Newton's second law states that the force equals the the change in momentum over time. The momentum equations for a control volume is in a Cartesian coordinate system defined in  $x$ -  $y$ - and  $z$ -direction.

$$\frac{\partial(\rho u_i)}{\partial t} + \frac{\partial}{\partial x_j}(\rho u_i u_j) = -\frac{\partial p}{\partial x_i} + \frac{\partial \tau_{ij}}{\partial x_j} + \rho f_i \quad (2.3)$$

### 2.1.1 Reynolds Averaged Navier-Stokes equations (RANS)

An instantaneous solution is not applicable or rarely seen in special cases, why proposition is to describe the turbulent flow field statistically. By taking the expected value of both sides on all four equations and simplify as far as possible according to the rules of expectation, the RANS set of equations is governed as

$$\frac{\partial \bar{u}_i}{\partial x_i} = 0 \quad (2.4)$$

$$\frac{\partial \bar{u}_i}{\partial t} + \bar{u}_j \frac{\partial \bar{u}_i}{\partial x_j} = -\frac{1}{\rho} \frac{\partial \bar{p}}{\partial x_i} + \frac{\partial}{\partial x_j} \left[ \nu \frac{\partial \bar{u}_i}{\partial x_j} - \overline{u'_i u'_j} \right] \quad (2.5)$$

where  $\bar{u}_i$  denotes the averaged value of velocities in  $x$ -  $y$ - and  $z$ -direction for instance [14]. Note that all primary flow variables can be divided individually as

$$\phi(x_i, t) = \bar{\phi}(x_i, t) + \phi'(x_i, t) \quad (2.6)$$

where  $\phi(x_i, t)$  denotes the instantaneous variable,  $\bar{\phi}(x_i, t)$  denotes the mean part of the variable and  $\phi'(x_i, t)$  denotes the fluctuating part of the variable.  $\phi(x_i, t)$  and  $\phi'(x_i, t)$  are varying randomly while  $\bar{\phi}(x_i, t)$  is not random, together representing a mean and fluctuating based decomposition called Reynolds decomposition.

However, this new set of equations referred to as RANS set of equations introduces six new unknown variables due to the symmetric Reynolds stress tensor  $R_{ij} = \overline{\rho u'_i u'_j}$ . The unclosed set of equations now contains in total ten unknown variables but only four equations. To get the amount of equations needed, the evolution equations of the stress tensor needs to be derived. Deriving these evolution equations as well describing the turbulence model, including evolution equation of turbulent kinetic energy  $k$  and turbulent dissipation  $\epsilon$  is indeed a part relevant when discussing RANS simulations. Although it has been chosen to be excluded to stick only to the basics of the underlying theory. However, this new set will enable unsteady simulations and is implemented and used in RotCFD.

## 2.2 Helicopter Hover Momentum Theory

The prime difference between other aerial vehicles and helicopters is the helicopter's ability to hover. In addition to the ability to hover, a helicopter's rotor has three main functions; generate lift, generate a propulsive force for forward flight and the ability to control altitude and position. Proper modeling is necessary to understand how a rotor is generating thrust and lift and how related variables such as power and torque depend on each other. Initially, the momentum theory will be described under ideal conditions using conservation of mass, momentum and energy in addition to Bernoulli's equation, to be further considered under non-ideal circumstances.

Assumptions have to be made as always. For hover flight it is assumed that there is no forward nor vertical speed. The flow field is axisymmetrical, meaning that velocities are constant at a constant radius along azimuthal direction. The flow outside the wake boundaries is relatively still and assumed to have a velocity close to zero, while the flow in the wake region can reach quite high velocities.

Global conservation of mass, momentum and energy is considered in momentum theory. Those conservation assumptions are not applied at the flow close to the blades but instead an imaginary actuator disk is considered, adding momentum and energy due to the moving blade. The flow that is generated is assumed to be incompressible, steady, inviscid and irrotational. The flow that passes through the actuator disk is assumed one-dimensional and uniform and similarly assumed to follow these conditions in the far wake with no swirl present.

Fig.(2.1) describes the notations of the aerodynamic variables in order to describe the hover flight regime for a helicopter. From an axisymmetrical perspective, the total control volume is divided into three control surfaces. An upper control surface denoted  $A_0$  and a lower denoted  $A_\infty$  with a surrounding side surface about the axis of rotation where no mass can flow through. Velocity at upper surface, denoted as the vertical velocity  $V_c$  is defined zero under hover conditions while lower surface velocity denoted wake velocity  $w$  added with the ascend velocity. The conservation of mass applies for the total control volume, the inflow massflow  $\dot{m}_0$  must equal  $\dot{m}_\infty$

and

$$\dot{m} \cdot d\vec{s} = 0 \quad (2.7)$$

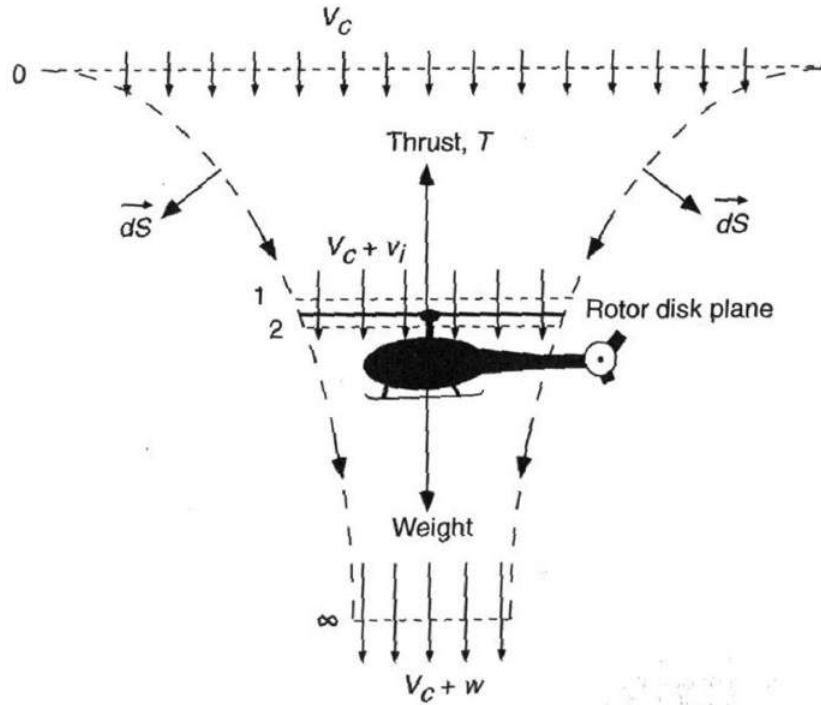


**Figure 2.1:** Notations of a helicopter in hover flight [4]

In order to get the velocity in the far wake and the induced velocity over the rotor, momentum and energy equations are used. The rate of momentum change over upper and lower boundaries equals the applied force, the thrust  $T$ .

$$T = \dot{m}w \quad (2.8)$$

since the velocity at the upper boundary  $V_c$  is zero during hover. The energy rate of change is the work done per unit time by the rotor as

$$T v_i = \frac{1}{2} \dot{m} w^2 \quad (2.9)$$

Eqs.(2.8) and (2.9) yield the relation  $w = 2V_h$  where  $V_h$  denotes the rotor induced velocity during hover. Using this relation and knowing that mass is always conserved, this will yield that  $A_\infty = \frac{1}{2}A$  that states that the far wake area is half the size of the rotor disk. Then, by using Bernoulli's equation for a particle that is

travelling vertically from the top of the control volume, through the rotor disk and down the wake, two equations can be set up,

$$p_\infty = p_1 + \frac{1}{2}\rho V_h^2 \quad p_2 + \frac{1}{2}\rho V_h^2 = p_\infty + \frac{1}{2}\rho w^2 \quad (2.10)$$

Note that the pressure is assumed to be atmospheric at the inlet and outlet, decreasing until it reaches the rotor where a pressure jump occurs. Highest pressure is seen at the lower part of the rotor disk and will fade back to atmospheric down the wake. See Fig.(2.2)

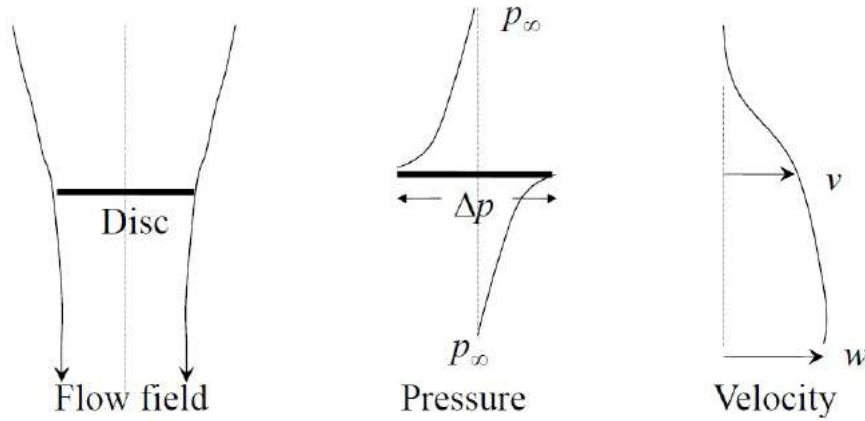


**Figure 2.2:** Flow fields, pressure and velocity distribution [4]

Continuously, the delta pressure over the rotor and the induced velocity as a function of the thrust be expressed as

$$\Delta p = \frac{1}{2}\rho w^2 \quad T = A\Delta p \Rightarrow V_h = \sqrt{\frac{T}{2A\rho}} \quad (2.11)$$

A very important feature in helicopter performance is to obtain a high figure of merit,  $FM$ . The figure of merit is defined as the ideal power over the actual measured power to generate thrust to maintain hover. The ideal power is the theoretically consumed power to move the air through the rotor to generate the desired thrust under ideal conditions. The actually measured power is taking into consideration non-ideal conditions such as profile drag of the rotating blades, the number of blades etc. The ideal power is calculated by the energy balance and using Eq.(2.11)

$$P_{ideal} = \frac{1}{2}\dot{m}w^2 - 0 = TV_h = T\sqrt{\frac{T}{2A\rho}} \quad (2.12)$$

## 2. Literature Study and Background

---

To non-dimensionalize the induced velocity at the rotor in hover, the induced flow ratio coefficient is used  $\lambda_h$  as  $V_h = \lambda_h \Omega R = \lambda_h V_{tip}$  where  $\Omega$  is the angular velocity. This convention is also used to non-dimensionalize other variables with the blade tip speed, such as thrust, power and torque in same order as

$$C_T = \frac{T}{\rho A V_{tip}^2} \quad C_P = \frac{P}{\rho A V_{tip}^3} \quad C_Q = \frac{Q}{\rho A V_{tip}^2 R} \quad (2.13)$$

Thrust coefficient is the ratio of thrust over dynamic pressure force, yielding a relation between induced flow ratio coefficient and the thrust coefficient as

$$\lambda_h = \sqrt{\frac{C_T}{2}} \quad (2.14)$$

The relation between power and torque is  $P = \Omega Q$  which by insertion will yield that the power and torque coefficient are equal,  $C_P = C_Q$ . Now the induced flow ratio is related to the thrust coefficient and the power is related to the torque using non-dimensionalized coefficients. The power depends therefore of the thrust as

$$C_P = \frac{P}{\rho A V_{tip}^3} = \frac{T V_h}{\rho A V_{tip}^3} = C_T \frac{V_h}{V_{tip}} = C_T \lambda_h = \frac{C_T^{3/2}}{\sqrt{2}} \quad (2.15)$$

### 2.2.1 Non ideal effects

So far only ideal conditions has been assumed. Considering situations like non-uniform flow, tip losses, wake swirl will make the derivation more realistic but more complex. To determine the actual rotor power required the profile drag needs to be considered. The profile drag of the blades moving through the air, assuming no twist and that the blades are not tapered, is expressed by integrating over the blade length and will yield the necessary power to overcome the drag for each blade where  $N_b$  is the amount of blades and  $D$  is the profile drag for each blade as  $D = 1/2 \rho (\Omega y)^2 c C_{d0}$ .

$$P_0 = \Omega N_b \int_0^R D y dy = \frac{1}{8} \rho N_b \Omega^3 c C_{d0} R^4 \quad (2.16)$$

where  $C_{d0}$  is the profile drag coefficient and  $c$  the chord line. Using the same conversion as for the power earlier, similarly the profile power coefficient can be derived from above expression as

$$C_{P_0} = \frac{1}{8} \left( \frac{N_b c R}{A} \right) C_{d0} = \frac{1}{8} \sigma C_{d0} \quad (2.17)$$

where  $\sigma$  is the solidity ratio which is the blade area over the total rotor disk area defined as

$$\sigma = \left( \frac{N_b c R}{A} \right) \quad (2.18)$$

To compute the actual measured power that the rotor requires to hover can be done from the actual power coefficient  $C_{P,actual}$ . When the drag is taken into consideration the actual power coefficient for the rotor is defined as

$$C_{P,actual} = C_{P,i} + C_{P,0} = \kappa \frac{C_T^{3/2}}{\sqrt{2}} + \frac{1}{8} \sigma C_{d0} \quad (2.19)$$

with  $C_{P,i}$  is the induced power coefficient corrected by an induced power correction factor  $\kappa$  which is typically about 1.15 and helps the power consumed (due to the induced flow field) to be more realistic and therefore slightly increased, for the same thrust generated. Now the approximated rotor figure of merit can be expressed using a non ideal approximation for the rotor power [4]

$$FM = \frac{C_{P,ideal}}{C_{P,actual}} = \frac{\frac{C_T^{3/2}}{\sqrt{2}}}{\kappa \frac{C_T^{3/2}}{\sqrt{2}} + \frac{1}{8} \sigma C_{d0}} \quad (2.20)$$

Regarding the tip losses, the cause of less lift on the wing tips due to leakage from bottom of the blade to top. The tip losses can be considered by computing the effective blade radius the produces lift;  $R_e = BR < R$  where  $B < 1$ . Propositions of calculation of the factor  $B$  is both due to theoretical derivations such as Prandtl theory, as well empirical (Gessow and Meyers) [4].

## 2.3 Rotorcraft Computational Fluid Dynamics

To conduct numerical simulations, RotCFD has been used, whose strength is its capacity of integrating rotorcrafts in an aerodynamic environment, such as hover, forward flight and dust simulations. RotCFD as software is written to only be used on desktop computers instead of supercomputers which makes it very less computationally demanding, although a trade-off is computational time increase and solution accuracy decrease. The Reynolds Averaged Navier-Stokes set of equations

discussed in previous section are implemented in the RotCFD flow solver. The RotCFD solver was developed and documented by Sukra HeliTek [5].

### 2.3.1 RotUNS - Flow Solver

RotCFD offers a wide range of different flow solvers. The choice of solver depends on each specific case and necessary requirements, such as body integration and its complexity, unstructured/structured grid and need for unsteady simulation for instance. Flow solver RotUNS (RotCFD Unstructured solver) discretize the finite volumes using the Semi-Implicit Method for Pressure-Linked Equations (SIMPLE/SIMPLER) approach with implicit time integration. RotUNS uses the two equation turbulence model  $k - \epsilon$  based on the unsteady Reynolds Averaged Navier-Stokes (RANS) set of equations and applies for all rotor flows, where  $k$  is the turbulent kinetic energy and  $\epsilon$  is turbulent dissipation [5]. RotCFD and RotUNS will be used synonymously from here.

### 2.3.2 RotCFD Rotor Model

RotUNS uses a three dimensional time accurate momentum source model - BEM (Blade element model) where the rotor is treated as a distribution of momentum sources. This eliminates the need to use a body-fitted grid about the rotor, but only for external bodies. The imparted rotor momentum source term,  $S'_i$ , depends on geometry of the airfoil and surrounding flow characteristics as a multi-variable function, and allows calculation of characteristic rotorcraft performance [5]. Also a steady rotor model can be used, that average the rotor momentum over time, without considering the instantaneous position of the rotor as it turns. This simplified approach was not used however.

$$S'_i = S'_i(C_l, C_d, \alpha, V_{abs}, \omega, x, y, z, t, c, \rho, B) \quad (2.21)$$

Using these source terms, the momentum equations can then be coupled. To implement the blade, the blade is divided in elements in spanwise direction. To reach a solution along the entire blade, interpolation is used between the solutions for the cross sections corresponding to the used airfoil tables, see Sec.(6.2) for content of airfoil tables. The momentum is only inserted in a grid cell whenever the rotor blade element intersects with it. The position of the momentum applied is defined by the position vector. Located spanwise from the axis of rotation and components expressed in normal coordinates as

$$R_r = \int_0^R dS \cos \delta \quad R_\theta = 0 \quad R_n = \int_0^R dS \sin \delta \quad (2.22)$$

where  $dS$  is the distance from the origin to the source point. In a summary this yields a relation between the global system and the normal coordinates by multiplying the transformation matrices with each other from the left as

$$\begin{bmatrix} V_n \\ V_\theta \\ V_s \end{bmatrix} = M_3 M_2 M_1 \begin{bmatrix} U \\ V \\ W \end{bmatrix} \quad (2.23)$$

Local coordinate systems are implemented to express body location, rotor location and different motions. Local coordinate systems used in this research are the rotor disc fixed Cartesian system and the rotor based cylindrical polar system along with the global Cartesian coordinate system  $(x, y, z)$ .

### 2.3.3 Rotor Disc Fixed Cartesian system

The rotor disc fixed Cartesian system  $(\xi, \eta, \zeta)$  follows the rotor motions as it implies.  $\eta$  is located along the blade radius and fixed on the rotor blade with  $\zeta$   $90^\circ$  offset while the  $\xi$  coordinate is located perpendicular to the tip path plane. The rotor disc fixed Cartesian system relates to the global system by a transformation matrix as

$$\begin{bmatrix} \xi \\ \eta \\ \zeta \end{bmatrix} = \begin{bmatrix} \cos B & \sin A \sin B & -\cos A \sin B \\ 0 & \cos A & \sin A \\ \sin B & -\sin A \cos B & \cos A \cos B \end{bmatrix} \begin{bmatrix} X - X_c \\ Y - Y_c \\ Z - Z_c \end{bmatrix} = M_1 \begin{bmatrix} X - X_c \\ Y - Y_c \\ Z - Z_c \end{bmatrix} \quad (2.24)$$

where  $A$  and  $B$  is the Euler angles that represents the pitch and lateral angles. Index notation  $c$  represents center in the global system.

### 2.3.4 Rotor Based Cylindrical Polar System

The rotor based cylindrical polar system  $(\xi, \eta, \zeta)$  is mainly used to describe the blade rotation path as the rotor spins. The  $z$  coordinate is intersecting with the  $\xi$  coordinate and moves perpendicular to the tip path plane in the inflow direction. To define the position of the blade, the azimuth angle  $\psi$  is used. The azimuth angle is measured from an axis which is parallel to tip path plane and the free stream.

why the the following relation between the rotor disc fixed and rotor based cylindrical coordinates is related

$$\xi = z \quad \eta = r \cos \theta \quad \zeta = r \sin \theta \quad (2.25)$$

## 2. Literature Study and Background

---

where  $\theta$  is defined as  $\theta = \frac{\pi}{2} - \psi$ . There is a pure rotation clockwise in the tip path plane between the two local coordinate systems. An ordinary linear transformation matrix is valid.

$$\begin{bmatrix} \hat{e}_r \\ \hat{e}_\theta \\ \hat{e}_z \end{bmatrix} = \begin{bmatrix} 0 & \cos\theta & \sin\theta \\ 0 & -\sin\theta & \cos\theta \\ 1 & 0 & 0 \end{bmatrix} \begin{bmatrix} \hat{e}_\xi \\ \hat{e}_\eta \\ \hat{e}_\zeta \end{bmatrix} = M_2 \begin{bmatrix} \hat{e}_\xi \\ \hat{e}_\eta \\ \hat{e}_\zeta \end{bmatrix} \quad (2.26)$$

# 3

## Simulating Martian Flight on Earth

The experimental testing is limited in the way that not all parameters are possible to replicate on Earth and if, there might be facility limitations as well. Attempting to mimic the atmospheric conditions at Mars is a challenging task and comes with a lot of limitations and required simplifications to be made. Reducing the pressure, obtaining a similar atmospheric density as Mars is one thing, but reproducing variables such as the atmospheric composition, temperature changes, speed of sound, unexpected winds and sandstorms and radiation are almost an impossible task, and yet the difference in gravity has not even been mentioned. In summary, whatsoever results that are acquired during Earth simulations, flight abilities for unmanned aerial vehicles on Mars can never be concluded certainly.

### 3.1 Difficulties and limitations

NASA Ames possesses an outstanding facility for disposal (see Sec.4.1), where most of the limitations can be faced as good as possible, while some can not be replicated but kept in mind for further post-processing and analysis. The rotor that has been used in this research is not the same as the final rotor and whatsoever results this rotor design will yield is mainly to be compared to its own experimental and numerical data. Also, the Mars Helicopter is proposed to be equipped with upper and lower collective as well lower cyclic controls [17], something that has not been able to replicate during the test campaign. Instead, part of the goal is to investigate how different factors affect the capability of flight on Mars compared to Earth, as well how limited wind tunnel testing are on Earth.

#### 3.1.1 Gravity

The mass of Mars,  $m_{Mars}=6.39E23$  kilograms compared to the mass of Earth,  $m_{Earth}=5.972E24$  kilograms is almost an order of magnitude less. Thus the gravitational pull will be significantly less on Mars, but also the distance to the sun affects the gravitation.

$$F_g = \frac{GMm}{r^2} \quad \rightarrow \quad \frac{g_{Earth}}{g_{Mars}} \approx 3 \quad (3.1)$$

where  $G$  is the gravitational constant,  $M$  the mass of the Sun and  $r$  the distance between the Sun and respective object. This means that the gravitational pull on Mars is only about a third of what it is on Earth. At first, this might seem promising for aerial vehicles operating on Mars, but the composition of the thin atmosphere on Mars ( $\sim 1\%$ ) in combination with the high gravity (about  $\sim 38\%$ ) will require an outstanding performance and sophisticated design of the Mars Helicopter. Gravity has for obvious reasons not been able to be replicated during the experimental testing.

#### 3.1.2 Pressure and Density

The pressure on Mars is very low compared to Earth. It ranges from slightly below 7 millibar up to almost 30 millibar, depending on location, season and temperature, while atmospheric pressure on Earth is about 1013 millibar. Although what is important is to match a corresponding density of the Martian atmospheric surface. The proposed landing sites for the Mars Helicopter on Mars all has an atmosphere with a pressure that corresponds best to the targeted density within the range 7 to 14 millibar [6].

According to the ideal gas law the interaction between the molecules in a gas needs to be considered small or that the molecules has completely elastic collisions if interaction occurs, which never occurs for a real gas but tend to be insignificant if the temperature is high and the pressure is low, why it can be applied on air. Although the temperature on Mars is significantly lower compared to Earth, the pressure is close to vacuum. Therefore, it may be possible to assume that the ideal gas law is approximately valid on Mars since the Martian atmosphere tend to behave as an ideal gas due to its low pressure. The pressure of Mars is about 0.7% of Earth while the density is about 1.3%. The ideal gas law is defined  $p = \rho RT$  where  $R$  is the specific gas constant.

A low density means that less molecules is present in the atmosphere. To generate lift for a helicopter, the main idea is to push molecules downwards and use Newton's third law in order to generate lift upwards - lower density gives less lift. As a result,

Mars comes with a huge disadvantage when it comes to generate propulsive lift. The low pressure and density could be well replicated and has been able to take into consideration due to the possibility of depressurization.

### 3.1.3 Reynolds number

The Mars Helicopter is proposed and will be designed to fly on as windless days as possible. Therefore, the Reynolds number can be mainly calculated from the angular velocity of the rotor. Reynolds number is a function of, except the geometry of the wing and the rotational velocity, the density and the dynamic viscosity. The dynamic viscosity is almost the same on Mars ( $\mu_{Mars}=1.79e-05$  while  $\mu_{Earth}=1.75e-05$ ) and the density is possible to mimic, meaning the Reynolds number is possible to replicate moderately. Due to the low density on Mars, the Mars Helicopter rotor will experience low Reynolds numbers. The rotor Reynolds number and the dynamic viscosity is defined as

$$Re = \frac{\rho V_{tip} L_c}{\mu} \qquad \mu = \nu \rho \qquad (3.2)$$

where  $\rho$  is the density of the atmospheric gas,  $V_{tip}$  is the velocity of the rotor blade,  $L_c$  represents the characteristic length of the airfoil session (typically the chord line),  $\mu$  is the dynamic viscosity of the fluid and  $\nu$  is the kinematic viscosity of the fluid.

### 3.1.4 Atmospheric composition

The composition of Mars's atmosphere is about 96 % carbon dioxide and  $\sim 2\%$  dinitrogen [12]. The heat specific ratio ( $\gamma = \frac{C_p}{C_v}$ ) will remain almost constant ( $\gamma_{Mars}=1.3$  while  $\gamma_{Earth}=1.4$ ). This will in turn affect the speed of sound. The speed of sound depends on the molecular collisions and by so the state and kind of the gas as well its temperature. The speed of sound, denoted  $a$ , is defined as

$$a = \sqrt{\gamma RT} \qquad (3.3)$$

where  $T$  is the surrounding temperature and  $R$  the gas constant. Due to low temperatures and the different atmospheric composition, the speed of sound will decrease, which will yield relatively high Mach numbers on Mars. The experienced Mach number by the rotor, based on the wing tip velocity, is defined  $M = V_{tip}/a$  [13]. Replicating the speed of sound effect during this project was not possible.

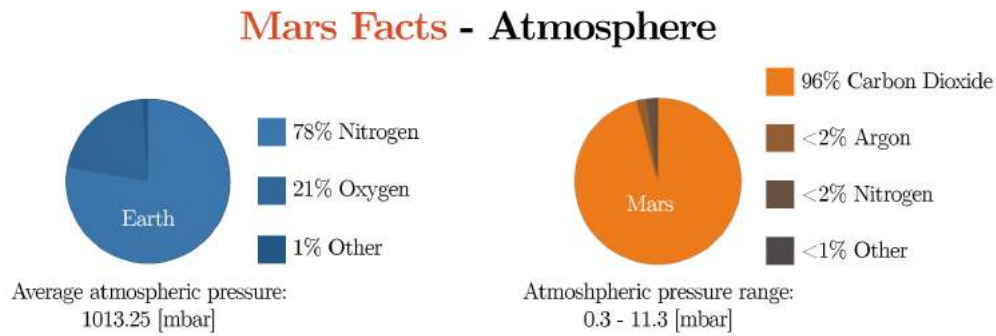


**Figure 3.1:** Atmospheric composition comparison - Earth and Mars [13]

### 3.1.5 Temperature

Mars is farther away from the sun and comes with a very harsh and cold environment. The temperatures on Mars is changing more drastically than on Earth ranging from  $30\text{ }^{\circ}\text{C}$  to  $-140\text{ }^{\circ}\text{C}$ , with an average temperature about  $-63\text{ }^{\circ}\text{C}$ . The Mars Helicopter will most likely operate under considerably colder circumstances, compared to what is possible to achieve during the experimental testing, as well to operate at slightly constant temperatures. Due to pressure changes and to ambient temperatures, the temperature will alter a lot during testing. Mars temperatures was not possible to replicate in a trustworthy manner.

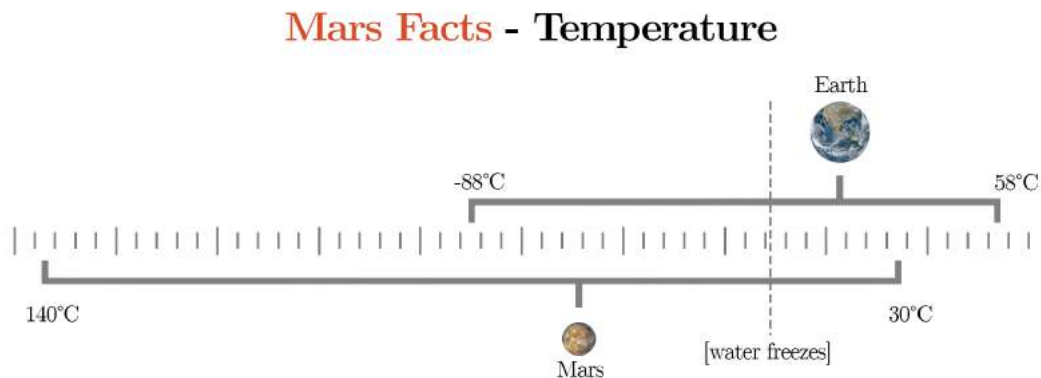


**Figure 3.2:** Temperature comparison - Earth and Mars [13]

### 3.1.6 JPL 25-ft Space Simulator

Not only NASA Ames conducts experimental testing for the Mars Helicopter, but also NASA's Jet Propulsion Laboratory (JPL). JPL possesses a 25-foot Space Simulator that allows depressurization (pressure control) and the ability to change at-

mospheric composition. The space simulator can fill up the chamber with carbon dioxide ( $CO_2$ ) to mimic a corresponding Martian atmosphere (96%  $CO_2$ ). To control temperature effects the walls have inside liquid nitrogen flowing to maintain a constant temperature to minimize heat and temperature effects [11].

### 3. Simulating Martian Flight on Earth

---

# 4

## Aeolian Wind Tunnel Testing

The first entry of wind tunnel testing were already conducted during Fall 2016. All data were corrected and compressed to be analyzed, acquired at different running conditions such as varying wind speeds, shaft angles and rotor speeds throughout a broad range of pressures.

### 4.1 Facility Description

All experimental testing has been conducted in the Martian Aeolian Wind Tunnel (MAWT) in the Planetary Aeolian Laboratory (PAL) facility at NASA Ames Research Center. MAWT is one of the worlds largest low-pressure wind tunnels, capable of simulating pressures ranging from 1 atmosphere down to 5.5 millibar and is an open-circuit tunnel with dimensions 1.3x1.3x13 meters. Initially it was used for sand dust simulations but are today used for propulsive flight testing at different pressures. In addition to the Martian Aeolian Wind Tunnel, the Titan Aeolian Wind Tunnel is also facilitated in the PAL, mainly re-purposed for aeolian research at the moon Titan. In the 1960's, PAL was used to depressurize spacecraft's and spacecraft instruments but presently the facility is solely dedicated for low and high pressure wind tunnel testing [13].

At atmospheric conditions, the MAWT generates wind by a fan at the end of the tunnel, hence sucks the air and creates a wind flow. At low pressures, the Mars wind tunnel uses a different approach to generate wind in the tunnel. Due to the lack of flowing air molecules at low pressures, the motor of the fan tends to be overheated. Instead several pipes are mounted horizontally at the end of the wind tunnel, connected to a pressure chamber with compressed air which supplies the wind tunnel with an airflow through small holes in the pipes. This creates a sucking effect and yield velocities up to 100 meters per second. Whenever higher pressures are simulated, this method is less favorable due to a lesser pressure difference. When compressed air is added into a depressurized chamber, the chamber pressure increases successively and has to be taken into account. Therefore the pressure has to be manually controlled continuously, to maintain desired simulation conditions.

Although, the PAL are not controlling the pressure itself since the vacuum ability is dependent upon operation of the neighboring facility, the NASA ARC-Jet Complex.

### 4.2 Mars Rotor Test Configuration

The Mars Helicopter will use a co-axial rotor configuration, designed for forward flight. To simplify the testing, a 40x22 propeller (see Fig.4.4) has been used as a two rotor setup, both turning in the same direction. It should be emphasized that a propeller were used. However, the experiment corresponded to edgewise flight why the propeller could be treated as a rotor. Also note that the actual Mars Helicopter rotor design is not yet set and is not the design that has been used. The setup consists of the propellers which are mounted on a shaft connected to the rotor hub and the motor.

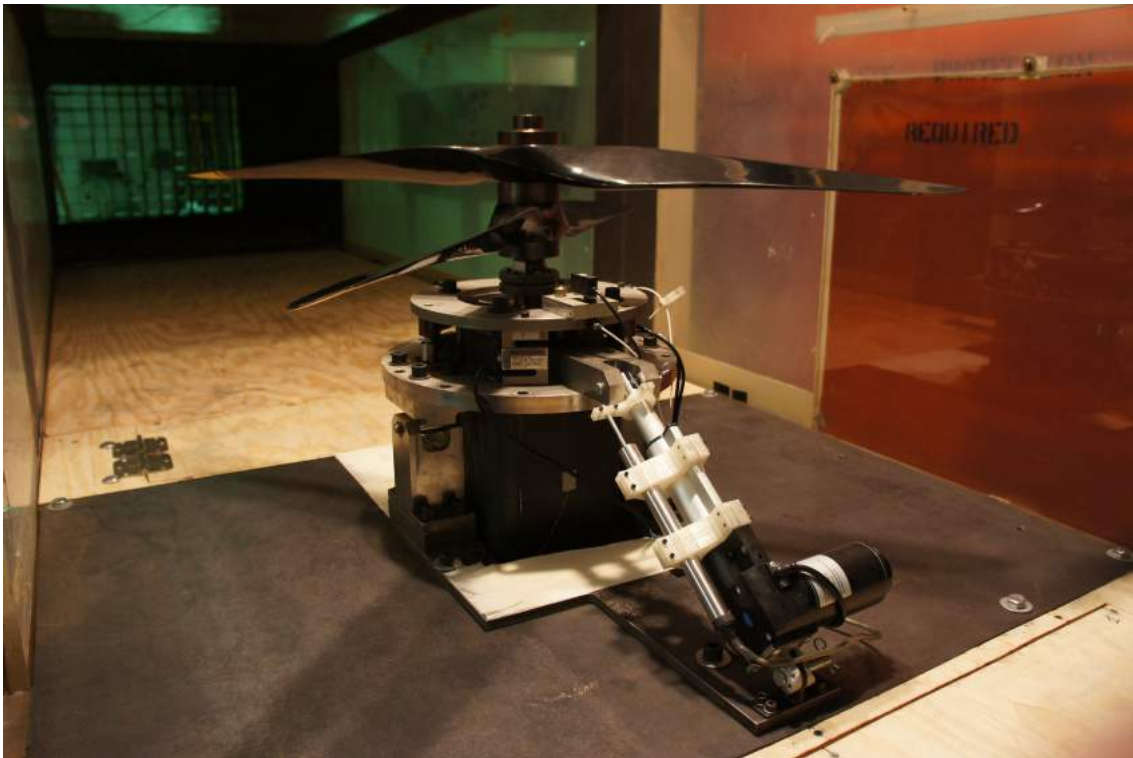


**Figure 4.1:** MAWT test configuration

A connecting arm were installed (seen in the front of Fig.(4.1)) to enable change of rotor tilt angle. The range of possible test angles range from  $-15^\circ$  to  $14^\circ$ , enabling both hover and forward flight testing. The axis which the rotor system were rotating about, was located 5.75 inches above the floor, see Fig.(4.2). The distance between the rotors were 2.77 inches with the center point, between the rotors, located 16.88 inches above the wind tunnel floor. To attach the propellers, eight smaller bolts

were used and a large bolt placed in the center of the rotational shaft, Fig.(4.3). All bolts were glued before assemblage in order for the bolts to resist vibrations.



**Figure 4.2:** Rotational motor stand



**Figure 4.3:** Mounting the rotors

### 4.2.1 Rotor selection

The 40x22 propeller had a radius of 20.115 inches which let the rotor tips come very close to the walls in the tunnel with only four inches in margin. Facility effects may occur such as wall and wake effects. Attempts have been conducted to deepen the understanding of how present those effects are, see Sec.(7.2.4).

The numbering description of propellers consists of four digits representing two numbers. The first two digits describes the diameter of the propeller in inches and the last two integers describes the pitch rate. Pitch rate refers to the distance in inches, that the propeller pulls for each revolution. Pitch rate symbolizes an ideal case, but due to blade slippage, the actual pulled distance tend to be less in reality.

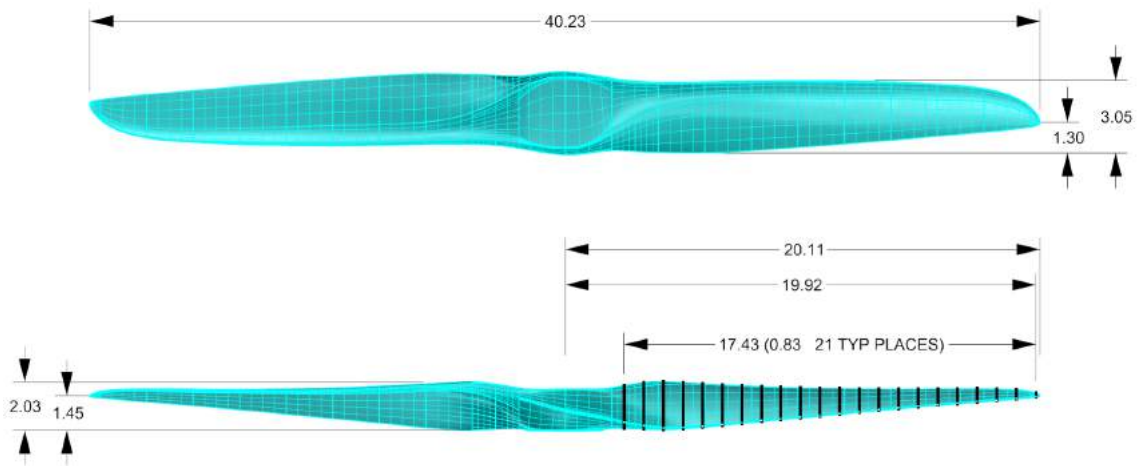


**Figure 4.4:** 3D model of 40x22 propeller

Laser scanning were used to obtain exact dimensions of the propeller blade. Fig.(4.5) displays the blade tapering while the steep slope of the built-in twist is displayed in Fig.(4.6). Note that the built-in twist at 70 % of the radius is  $16.63^\circ$  with a total twist rate of  $17.08^\circ$ . In addition, the cut-out radius were  $r/R = 0.1651$ . Due to edgewise flight testing, the 40x22 propeller will be referred to as rotor from here.

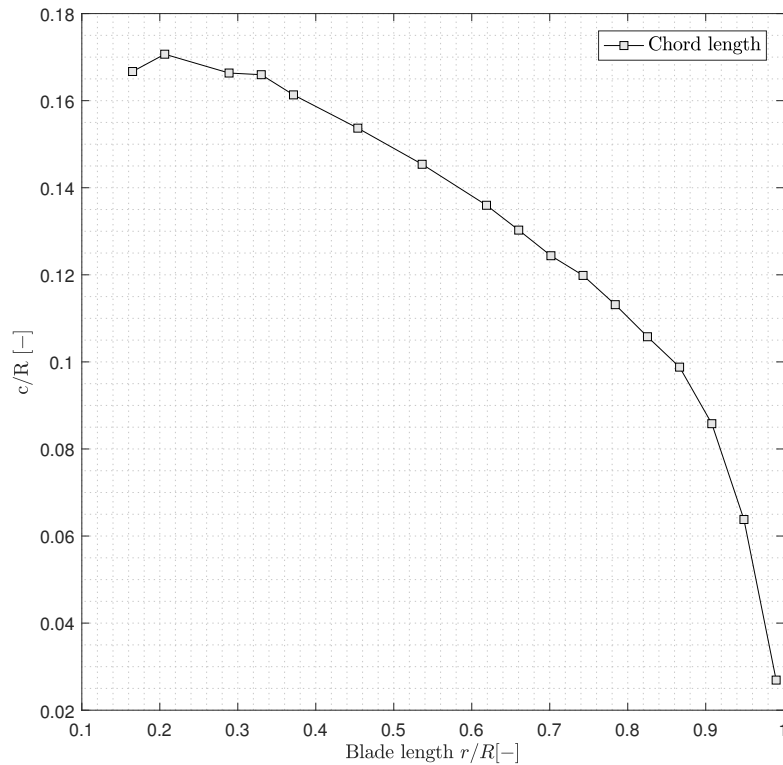


**Figure 4.5:** Chord distribution along the radius of the blade, 40x22 Propeller

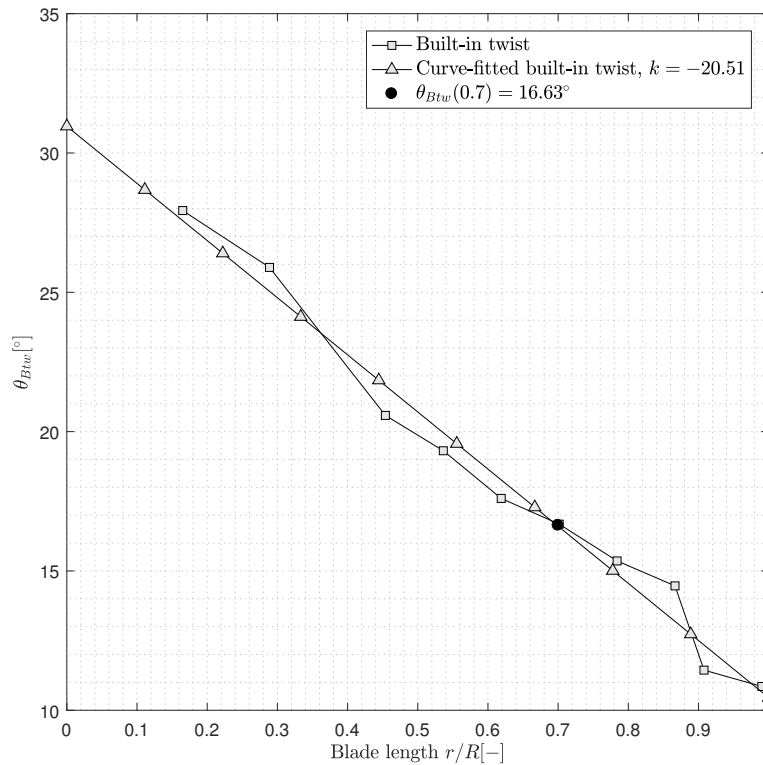


**Figure 4.6:** Twist distribution along the radius of the blade, 40x22 Propeller

## 4.3 Measurements

During wind tunnel testing, flow properties and chamber condition quantities are measured and recorded. A lot of properties are desired to monitor, for instance surrounding temperature and pressure using sensors inside the chamber. Velocities, both at the inlet and in the wake of the rotors, is measured using pitot tubes. However, measuring the thrust will be explained more in detail for its importance in this thesis.

### 4.3.1 Thrust

The total dead load contains the load of the motor, motor plate, motor shaft and propellers, placed on top of three strain-gauge pressure sensors, from now referred to as the load cells, which initially carry all the weight, see Fig.(4.1). The three load cells are axisymmetrically placed with a  $120^\circ$  spacing, third load cell approximately located on the axis of rotor tilt rotation. Whenever the motor is spinning, lift will be generated and the thrust is measured parallel to the load cells, independent

of the shaft angle. The loads measured will help to perceive the rotor's roll and pitch moments ( $M_x$  and  $M_y$  respectively) whose directions are shown in Fig.(4.7), including load cell positions.

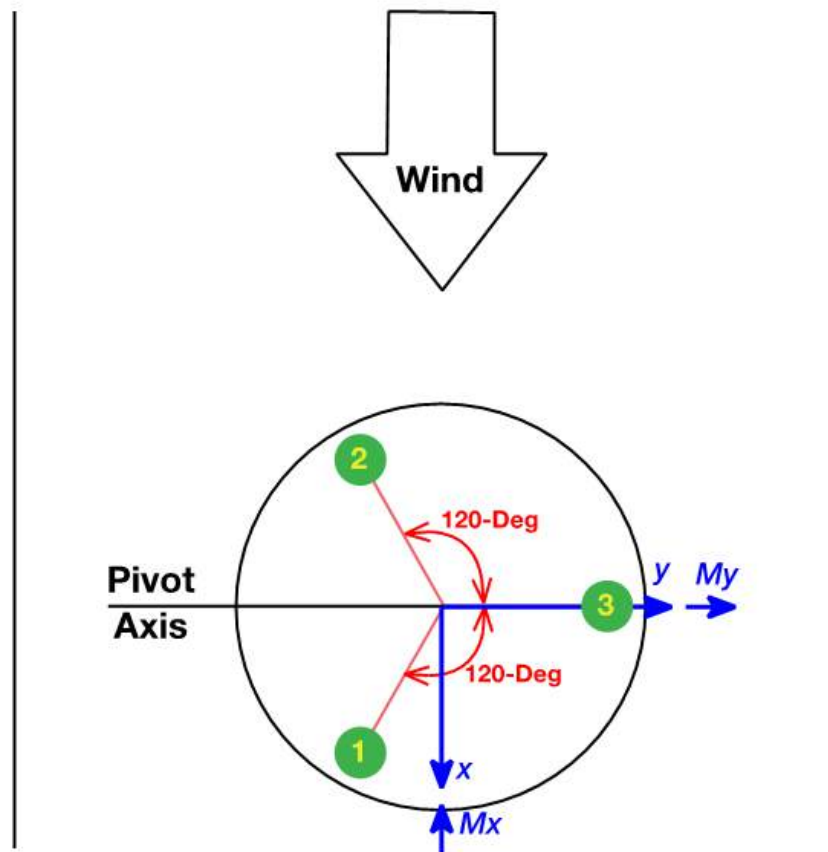


**Figure 4.7:** Load cell positions and coordinate system definition.



Figure 4.8: Mounting load cells to the motor hub.

### 4.3.2 Chamber temperature and pressure

The temperature and pressure is measured by sensors, placed inside the vacuum chamber, and connected from inside the chamber to the control room, connected to a LABVIEW system located in the control room, independent of the AstroMed system, explained in Sec.(4.3.4).

### 4.3.3 Accelerometers

For any rotating system, it is crucial to avoid resonance frequencies why a banking test had to be performed. For such a test, accelerometers were used and placed on the rotor shaft to measure its acceleration, the rate of change of velocity, which can

be static or dynamic in nature.

Initially static acceleration was tested. A frequency spectrum for the static hardware were generated using an impulse impact hammer, see Fig.(4.9), while the motor was turned off; once generated, the resonant frequencies of the static system could be identified, and subsequently converted to RPM. This knowledge is important, by using this method, RPM's that may create resonance in the system could be identified and avoided to prevent damage to the hardware while testing.

Secondly the dynamic acceleration was investigated to measure how much the rotating system were vibrating while actively testing. During the tests, two accelerometers were monitored to make sure they would stay below a certain vibratory threshold, vibrations due to the motor spinning the rotors.

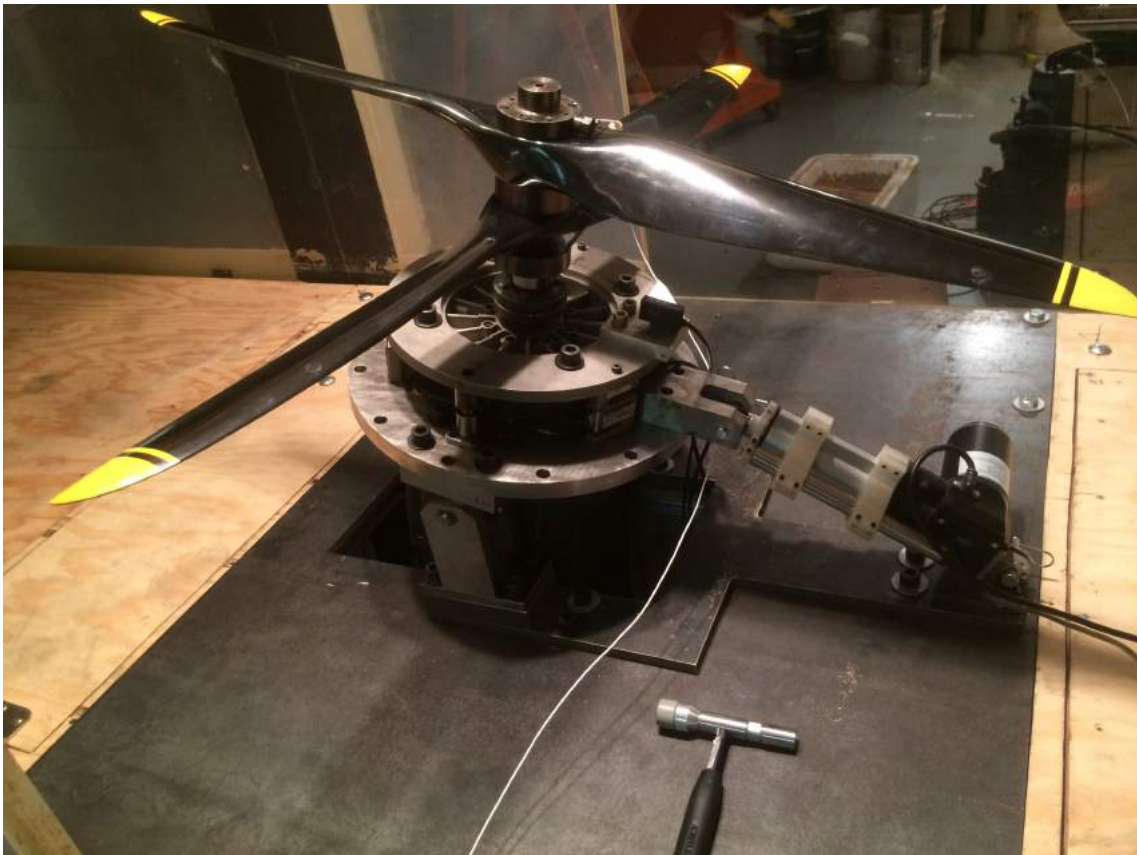


**Figure 4.9:** Static banking test

### 4.3.4 Data Acquisition

The data was acquired using an AstroMed Dash 18-X. Basically, a device that reads in a voltage signal, and converts the signal into engineering units by calculation off manufacturer calibration. For instance, to spin the motor faster, the electric current needs to be increased. If current increases, so do the voltage, and the

increase in voltage is converted into a corresponding RPM by the AstroMed. The AstroMed collects data at various sample rates. Since noise generation most of the time were recorded, the sample rate collected 100.000 samples each second due to the microphone analysis. An exaggerated amount for load cell data for which 200 samples per second would be sufficient. The acquired data was later averaged and became the main source of data for this project. The devices of interest in this thesis that were connected to the AstroMed were the following; motor to read motor RPM, pitot tubes to measure wind speeds in the wind tunnel and the load cells to measure rotor thrust.

### 4.4 Test Procedure

The Fall 2016 testing included a multitude of changing variables, including RPM, pressure, shaft angle, and tunnel wind speed, making it difficult to develop trends in the data collected. For the Spring 2017 testing, from which the data in this report was reduced, many of the said variables were held constant, allowing for better deduction in the post processed data. For instance, in the spring forward flight testing, the shaft angle was held constant at  $14^\circ$ , which reduced hysteresis effects in the actuator. While pressure were held constant, errors in thrust collected could be reduced.

### 4.5 Test Matrix

The Spring 2017 test matrix included RPM sweeps at various pressures. Once the vacuum facility was depressurized to a specific pressure, the following RPM sweep was executed: 0, 1868, 2100, 2500, 2800, 3000, 2800, 2500, 2100, 1868, 0. That being said, holding a particular pressure for an extended period of time depending on constant monitoring and physically maintaining of the vacuum facility, as the facility naturally increase in pressure at about 1 millibar per minute. Each data point was 15 seconds, which implies that for each collected point, the pressure may have drifted by a maximum of 0.25 millibar. From here, RPM sweeps will refer to the above mentioned RPM's.



# 5

## Load Cell Validation

For any experimental testing performed, it is crucial to use reliable equipment to ensure that the measurements are made correctly. A lot of data were acquired during Fall 2016 testing and a validation analysis had to be made to confirm the equipment worked as expected before proceeding to the next entry. An overall challenge simulating Martian conditions is to capture the small thrusts generated at the low pressures with a minimized standard deviation. Effort has been put into investigating and determining how valid the acquired data are.

When the entire test configuration were mounted, the three load cells always carried a total load of about 110 pounds. The capacity of each load cell was 50 pounds which yields a total preferable thrust not to exceed 40 pounds. Due to the fact that the configuration always required the load cells to take up the dead load, more sensitive load cells with lesser capacity could not have been used. For a valid post analysis, independently of pressure, the load cells are required to capture the actual thrust. In an attempt to confirm the load cells validity, repeatability analysis has been done under both static and dynamic circumstances. Dynamic load cell validation is discussed in Sec.(7.1.1).

For the static case, weights were stacked on top of the rotor system under static conditions (motor turned off at zero wind speed), and successively the load was increased. For each point, all loads were noted, further corrected by relating each load to the unloaded first point - the zero point. Initially starting with two pound weights to later increasing with ten pounds weights, finally reaching 50 pounds in total stacked load upon the system. In the same manner the weights were removed back to zero.



**Figure 5.1:** 50 pounds in load stacked on the hub

Ideally the line in Fig.(5.2) would follow the same path back to zero but due to mechanical hysteresis, the ability to measure the load gives a slight error. Fig.(5.3) shows the increase in load for each load cell respectively, for each weight added. Ideally the three lines in Fig.(5.3) should align. Note,  $x$  is not to be confused with positional direction, but denotes the point number.

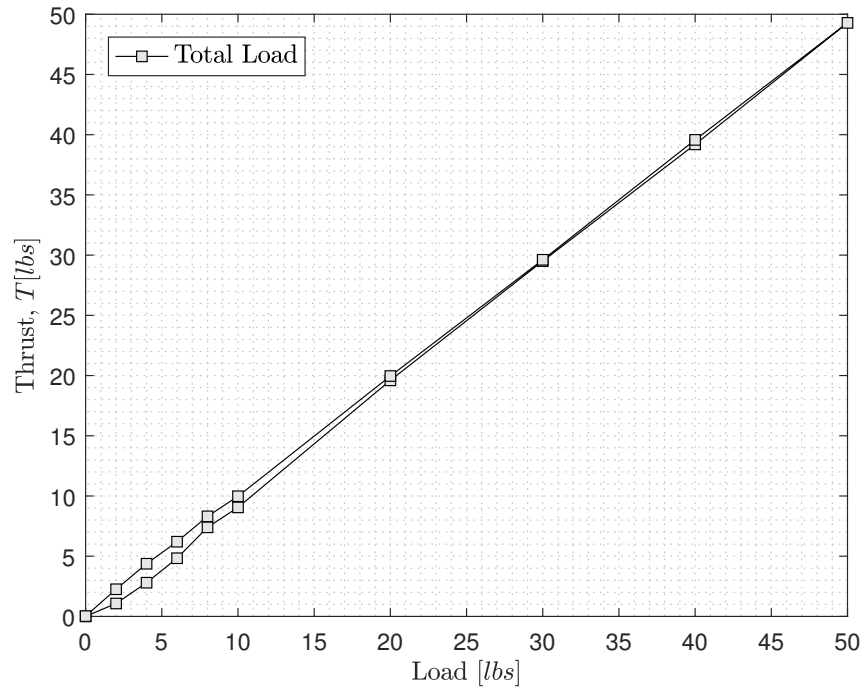


**Figure 5.2:** Repeatability analysis. Total load, stacking weights on the hub

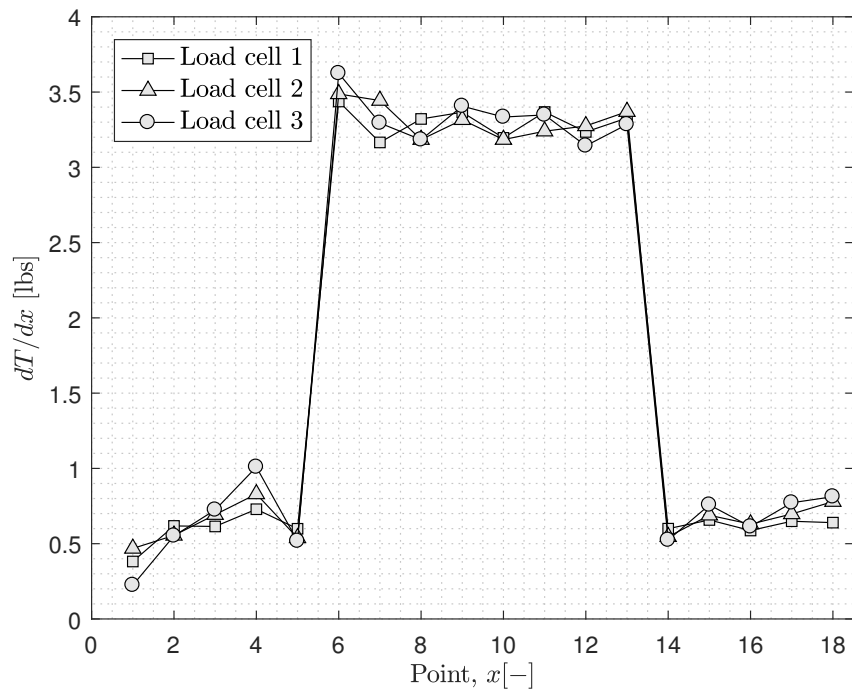


**Figure 5.3:** Repeatability analysis. Individual load cell gain, stacking weights on the hub

In a static case, the load cells seem to read properly with a maximum residual of about a pound. However, the first point taken (see Fig.(5.2)) when the system went from unloaded to loaded, about one pound error occurs. This might be due to initial vibrations and friction and might cause the system to read less good.

The dynamic evaluation were done during a pump up drift, comparing the zero points throughout a four hour long run (run 75) completing eighteen RPM sweeps. Ideally, the load cells should read the same each time the rotor stops spinning. Although smaller drifts occurred, see Sec.(7.1.1).

### 5.1 Weight tare validation

The load cells can only capture the vertical loads due to the experimental setup. In order to understand the correct thrust at each angle, as well from a repeatability perspective, a weight tare validation was done. Tilting the rotor system one degree per point, covering the motor tilt angle range ( $0^\circ$  to  $-15^\circ$  to  $14^\circ$  and back to  $0^\circ$ ), the load at each angle can be captured. Small mechanical hysteresis occurred as seen in Fig.(5.4). An expected result since the same behavior was seen in previous section.

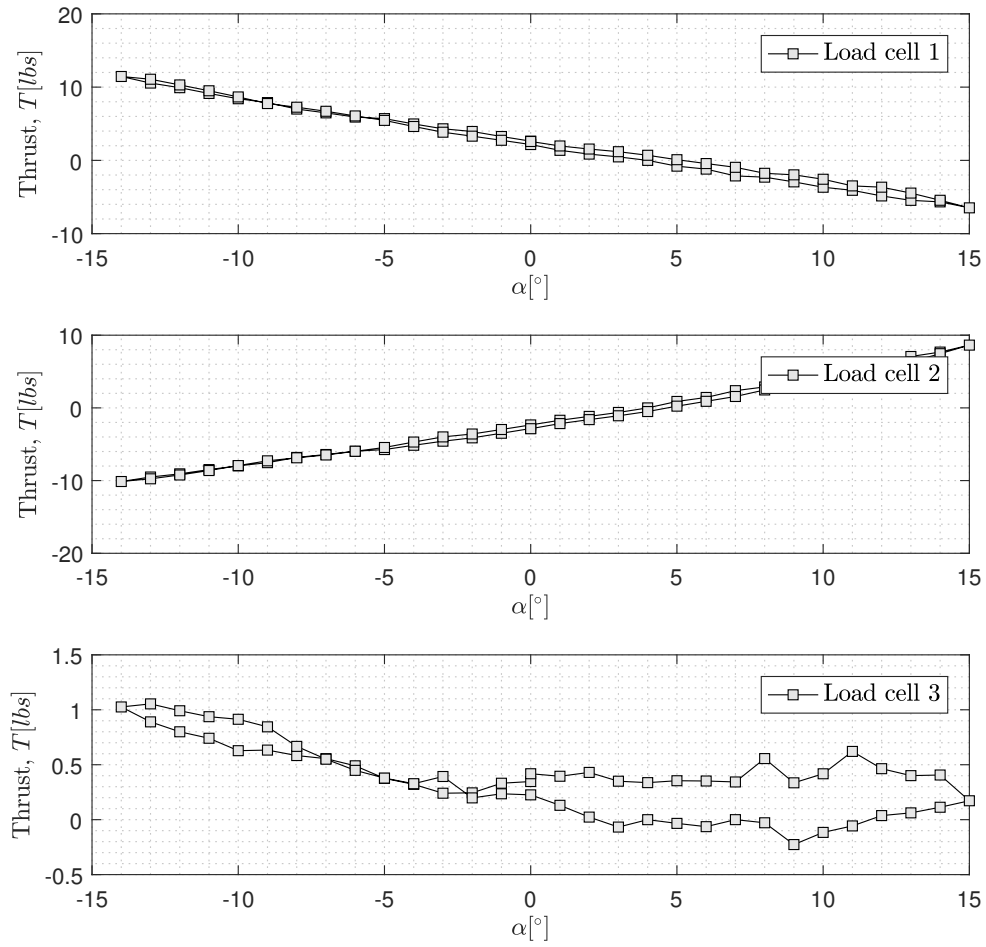


**Figure 5.4:** Weight tares for each load cell, rotor shaft angle changing within the range -14 to 15 degrees.



# 6

## Numerical Prediction of Rotor Performance

To investigate the capability to reproduce low pressure simulations, correlating experimental data to the testing sessions done, RotCFD has been used. Not only for correlation purposes, but also for evaluating wall effects, comparing free field (open air) simulations to tunnel prediction results. Since depressurization till almost vacuum is quite a time-consuming and costly process, it would be of great value to be able to predict aerodynamic performance of rotorcrafts at low pressures. If possible, RotCFD could become a very valuable tool, not only for the Mars Helicopters purpose, but also future missions.

### 6.1 Grid Generation

RotCFD divides the domain into a Cartesian octree grid where the user chooses the amount of cells in each direction. The Cartesian octree grid sub-divides into tetrahedral cells close to the boundaries of any solid body. Although this has not been used in this research since the rotors are implemented through the beam element model.

#### 6.1.1 Time grid

To determine cell sizes and the time grid, several basic guidelines have been followed. As a thumb rule, to determine the time grid settings, at least fifty rotor revolutions should be simulated as a minimum, to ensure convergence in a free field hover case, while in a tunnel case, about three hundred.

The time step is based on the time it takes for the rotor to rotate  $3^\circ$ , thus the time step becomes a function of RPM. Although different RPM's have been simulated, the time step should be proportional to the angular velocity to prevent the solution to be

altered. Roughly, the amount of time steps set for each simulation has been between 28.000 and 40.000 with flow times about five to seven seconds. A higher amount of time steps is required for tunnel simulations due to longer convergence time for a flow in a tunnel compared to an open free field. For reference, the CFL-number has been calculated based on the wing tip velocity, time step and the smallest cell width in the grid.

$$CFL = \frac{V_{tip}\Delta t}{\Delta x_{min}} \qquad \Delta x_{min} = \frac{L_s}{2^{r_{ref}-1}n_{cs}} \qquad (6.1)$$

$L_s$  denotes the length of the domain in streamwise direction,  $n_{cs}$  the number of cells in streamwise direction and  $r_{ref}$  the refinement level. Although, for the unsteady simulations, the time step used was solely based on the time it takes for the rotor wing tip to cover a rotation of  $3^\circ$ , with the CFL-number criteria kept in mind.

### 6.1.2 Domain size

To determine the flow field domain size, a good thumb rule for a free field simulation is that the domain should be at least five rotor diameters wide in all directions and ten times in the rotor wake direction [3]. For tunnel simulations, the domain was sized the same dimensions as the actual wind tunnel (for dimensions, see Sec.(4.1)), to mimic the experiment as good as possible.

Figs.(6.1),(6.2) displays the grid used for free field simulations (835.816 cells) from side and top view respectively. Two refinement boxes were used to concentrate the cell amount around the rotors and in the rotor wake. Fig.(6.2) shows how the grid is symmetrical in  $z$ -direction.

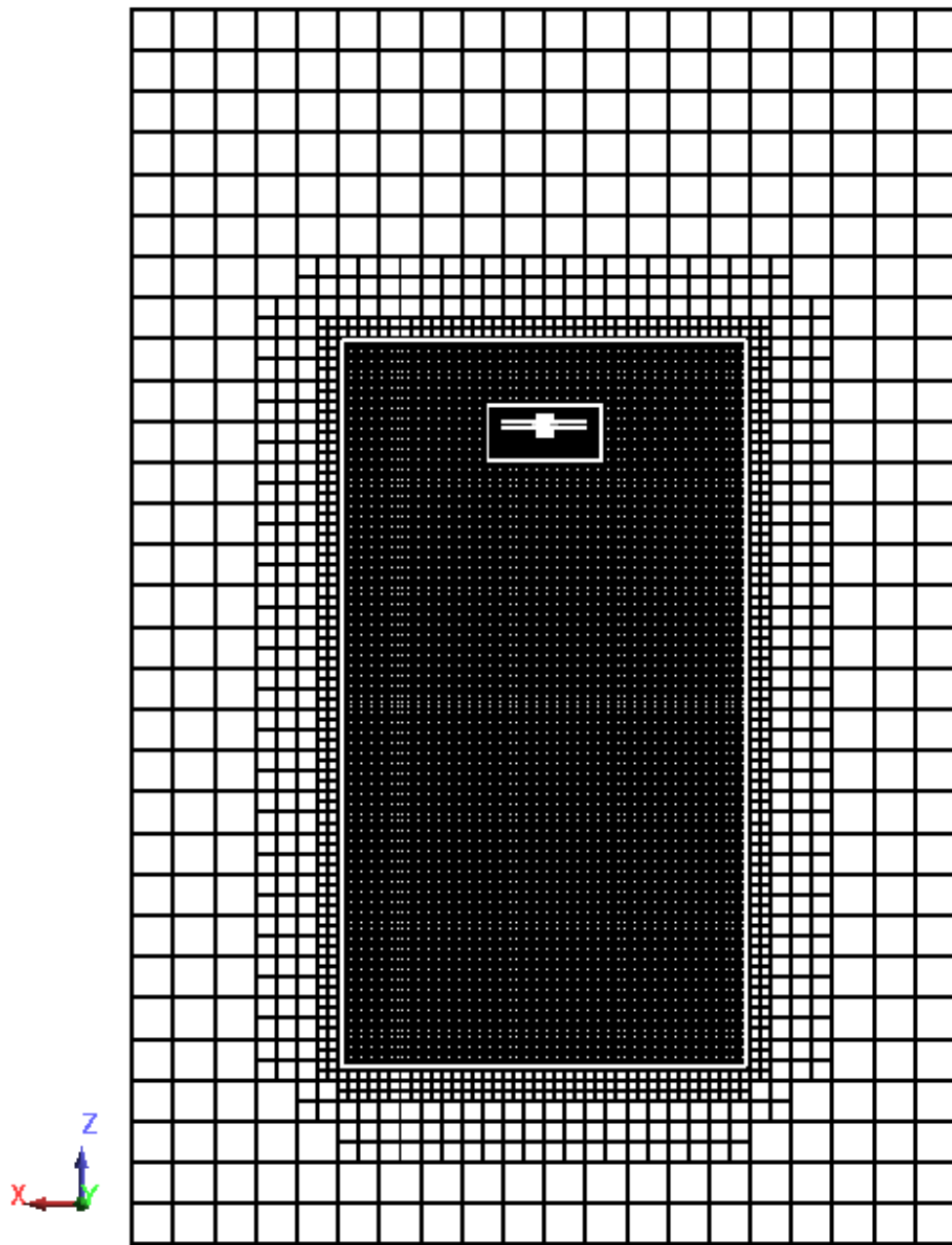


**Figure 6.1:** Grid used for free field simulations, side view

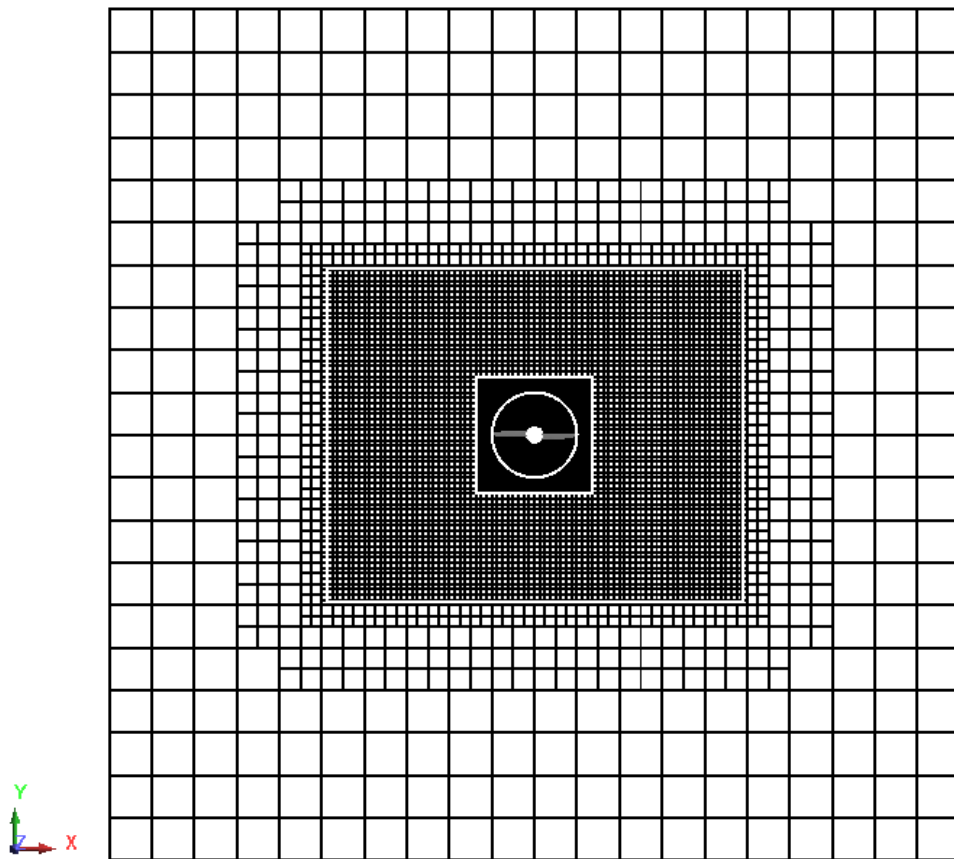


**Figure 6.2:** Grid used for free field simulations, top view

Figs.(6.3),(6.4) displays the grid used for the tunnel simulations (1.115.156 cells) from a side and front view. Two refinement boxes were used for the tunnel grid as well. In addition, boundary refinement were used along the walls, in hope to capture boundary layers and wall effects better. The grid is symmetrical in  $x$ -direction.

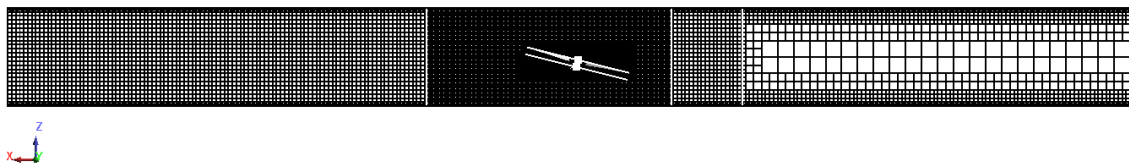


**Figure 6.3:** Grid used mimicking the wind tunnel simulation, side view

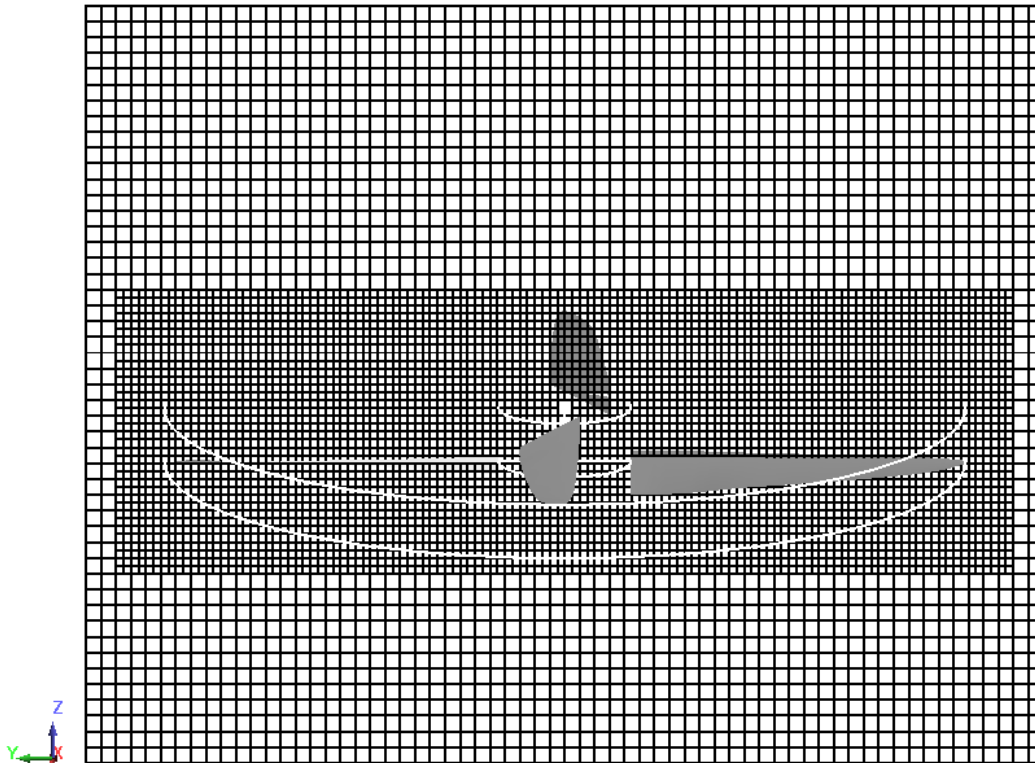


**Figure 6.4:** Grid used mimicking the wind tunnel simulation, front view

RotCFD is developed for use on desktop computers and do not support the use of super computers. The user can either choose to run on the Graphics Processor Unit (GPU) or the Central Processing Unit (CPU). GPU is preferable and approximately three times faster. Although, the user is still limited in computational power and can not use finer grids than approximately 1.2 million cells, which requires the cells to be wisely distributed in the domain.

## 6.2 Airfoil Tables

The Beam Element Model approach requires a predefined solution of  $C_l$ ,  $C_d$  and  $C_m$  (sectional coefficients of lift, drag and moment) before starting the simulation. Lower case subscripts denotes coefficients for a sectional 2D airfoil. These solutions are stored in so called airfoil tables, generated in C81 Gen and corresponds to different Mach numbers and Reynolds numbers at all possible angles of attack  $\alpha$ . Each airfoil table is determined for a specific airfoil location along the rotor blade, in this research at radial stations  $r/R = 0.29$ ,  $r/R = 0.58$  and  $r/R = 0.78$ . Although, solutions are only generated within a certain range of angle of attacks ( $-14^\circ < \alpha < 30^\circ$ ) while the remaining angles will correspond to the NACA 0012 airfoil. If an angle of attack is between two already prescribed values, the solution will be interpolated.

### 6.2.1 Angle of Attack

Angle of attack, denoted  $\alpha$ , represents the angle between the airfoil chord and the incoming relative wind, see Fig.(6.5). When the angle of attack increases, it becomes more difficult for the air to flow smoothly around the airfoil, and at a certain critical point the airflow will begin to separate over the airfoil, creating turbulence [15].

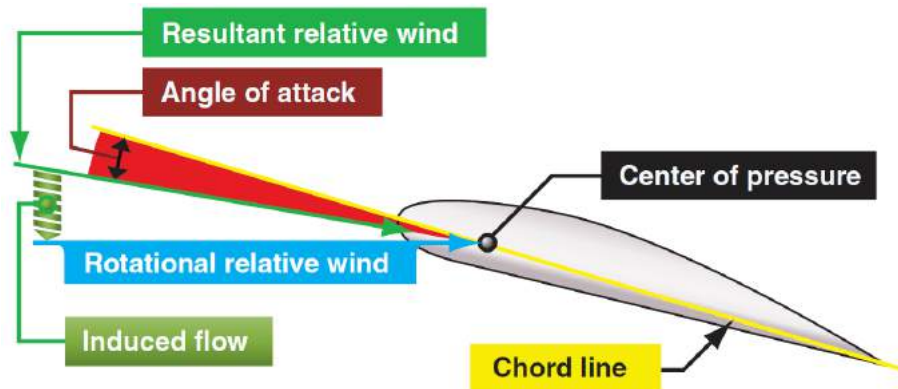


Figure 6.5: Angle of attack visualization [15]

### 6.2.2 Lift coefficient

The amount of lift depends on the shape of the airfoil, the density of the surrounding fluid, the relative incoming wind speed and the angle of attack, why the airfoil tables for all three coefficients contains a wide range of angles of attack, from  $-180^\circ$  to  $180^\circ$ . At small angles of attack, intuition tells that higher angle of attack, the more lift is generated. When blade inclination increases for larger angles, the lift depends more significantly of the above mentioned variables. Having a too large angle of attack will create stall of the wing, forcing the boundary layer to separate. When stall occurs, the airfoil suddenly loses its lift. The sectional lift coefficient denoted  $C_l$  is defined as

$$C_l = \frac{F_l}{qA} \quad (6.2)$$

where  $F_l$  denotes lift force,  $q$  the dynamic pressure and  $A$  the projected wing area, and is by so a ratio generated lift to the force generated by the dynamic pressure on the affected wing area. In an experimental environment such as a wind tunnel, dynamic pressure and area can be controlled and then the thrust measured. Consequently the thrust can be estimated at different conditions when wind speed or density is changed for instance [13].

### 6.2.3 Drag coefficient

The sectional drag coefficient, denoted  $C_d$  depends similarly as the sectional lift coefficient and represents the ratio of drag force and dynamic pressure force. Dependent of the shape of the airfoil, the angle of attack, density of the air, the incoming relative wind speed as well the drag force created by the rotor moving through the air, defined as

$$C_d = \frac{F_d}{qA} \quad (6.3)$$

where  $F_d$  denotes drag force. When the airflow starts to separate, turbulence is created and will result in a huge increase in drag and decrease in lift which is why an increased inclination will reach a stall state at a critical angle of attack. [15]

### 6.2.4 Moment coefficient

The sectional pitching moment coefficient, denoted  $C_m$ , defines in general any pitching moment acting on the pitch axis of a moving body. The sectional pitching moment on an airfoil is the moment produced by the aerodynamic force on the airfoil. At two percent of the chord line, the pivot is located. From here the moment is taken. The amount of moment the wing profile feels, will itself affect the rotation of the airfoil and change angle of attack.

## 6.3 RotCFD Setup

Beyond setting up a valid time and space grid and generating correct airfoil tables, additional things has to be set before starting a simulation in RotCFD. To implement the rotors correctly, besides the use of airfoil tables, twist and chord along the rotors radius has to be defined. This was done using the laser-scanned design data from Figs.(4.5),(4.6), along with the wing tip speed which is calculated from the given RPM

$$V_{tip} = \frac{2\pi RPM}{60} R \quad (6.4)$$

where  $R$  is the rotor blade radius. When rotor settings has properly been set, the surrounding environment such as the flow properties of the air and boundary conditions has to be defined. The turbulence model is already set (RANS), only

optional to vary in either steady or unsteady flow, where unsteady option has been used for all simulations.

### 6.3.1 Flow properties

The flow properties let the user to define the surrounding conditions in the domain. Since there will always be air in the tunnel, the specific gas constant for air,  $R_{spec}=287.05$  and the specific heat ratio  $\gamma$  will be constant, independent of pressure.

<b>Static Density</b>	1.225	$[kg/m^3]$
<b>Static Temperature</b>	288.16	$[K]$
<b>Gas Constant</b>	287.05	$[m^2/(s^2K)]$
<b>Specific Heat Ratio</b>	1.4	$[-]$
<b>Dynamic Viscosity</b>	1.75e-05	$[Ns/m^2]$
<b>Static Pressure</b>	101325	$Pa$

**Table 6.1:** Terrestrial flow properties

<b>Static Density</b>	0.008	$[kg/m^3]$
<b>Static Temperature</b>	288.16	$[K]$
<b>Gas Constant</b>	287.05	$[m^2/(s^2K)]$
<b>Specific Heat Ratio</b>	1.4	$[-]$
<b>Dynamic Viscosity</b>	1.79e-05	$[Ns/m^2]$
<b>Static Pressure</b>	700	$Pa$

**Table 6.2:** Martian flow properties

The temperature varies a lot during depressurization, always affected due to surrounding temperatures as well. Therefore the temperature was assumed to be room tempered for simplicity, independent of simulation case. The dynamic viscosity  $\mu$  differs slightly from 7 to 1013 millibar, while the density, which depends on the surrounding pressure, were calculated for all low pressure simulations using the ideal gas law, assumed to apply for such low pressures.

### 6.3.2 Boundary conditions

The simulated cases can roughly be divided into two categories; free field and tunnel simulations. Free field means no walls are present where the rotor configuration were simulated in open air. The boundaries must not interfere with the flow and therefore a mass outflow boundary condition is set at the outlet and a velocity restriction at remaining boundaries where air is allowed to pass through. In all hover cases a small velocity,  $V_\infty=0.1 m/s$ , was set to get the air moving at the velocity boundaries, all in downward direction.

While simulating the wind tunnel, same boundary condition were used at the outflow to replicate the open circuit wind tunnel used. To create an airflow, the inlet condition uses the velocity restriction, with an inlet velocity in streamwise direction into the tunnel. Unlike the free field case, air can not pass through the walls in the

tunnel, why remaining boundaries were set as viscous walls. Viscous wall applies the no-slip condition at the boundary, as well that no air can pass the boundary. In addition, a boundary refinement were added to all walls to capture boundary layers. However as mentioned, there are limitations in how fine grid that can be used, as well using Reynolds Averaged Navier-Stokes to model the turbulence, it is hard to capture such effects and were barely seen.

## 6.4 Correlation Matrix

An aim in this project was to understand RotCFD's capability to reproduce experimental results from the wind tunnel testing at Martian pressure - 7 millibar. During the depressurization run, using two rotors, the facility were not able to hold the pressure steady at 7 millibar. When 7 millibar were reached, the pressure started to drift while data were acquired. Therefore, the five points chosen to be correlated instead was captured at pressures 9.99, 10.93, 12.27, 13.33 and 13.73 millibar, see Tab.(6.3). The idea is to run RotCFD under as similar conditions as possible as these points were taken for, and compare the generated thrusts. See result in Sec.(7.3)

Run	Seq.	Pt.	RPM	LC 1 [N]	LC 2 [N]	LC 3 [N]	T [N]	p (mbar)
75	32	32	1860	0.43	1.20	-0.02	1.61	9.99
75	33	33	2089	0.58	1.53	0.10	2.21	10.93
75	35	35	2483	0.98	2.14	0.26	3.38	12.27
75	36	36	2780	1.30	2.72	0.56	4.58	13.33
75	37	37	2976	1.88	3.00	0.82	5.70	13.73

**Table 6.3:** Correlation matrix, experimental data to be compared to numerical



# 7

## Results

The result chapter is roughly divided in experimental testing results, post processed in MATLAB, RotCFD results and lastly a correlation section, comparing experimental and numerical data as mentioned in Sec.(6.4).

### 7.1 Experimental Results

#### 7.1.1 Load cell drifts

The dynamic load cell validation were done during wind tunnel run 75, a four hour long low pressure run. Run 75 acquired eighteen RPM sweeps at pressures ranging from 8 to 200 millibars with a two rotor configuration and a motor tilt at  $\alpha = 14[^\circ]$ , thrusting up. Possible reasons why a drift were seen is believed to be due to either pressure, motor temperature and chamber temperature. Fig.(7.1) shows thrust against pressure. Clearly load cell 2 shows the most non-consistent behavior. The horizontal lines refers to the initial value and acts as a reference. Load cell 2 varies with more than a pound, while load cell 1 and 3 varies in a more reasonable way, about 0.25-0.5 pounds. Note that the uncorrected load appears as negative in all subplots since positive direction is defined upwards in the tunnel.

## 7. Results

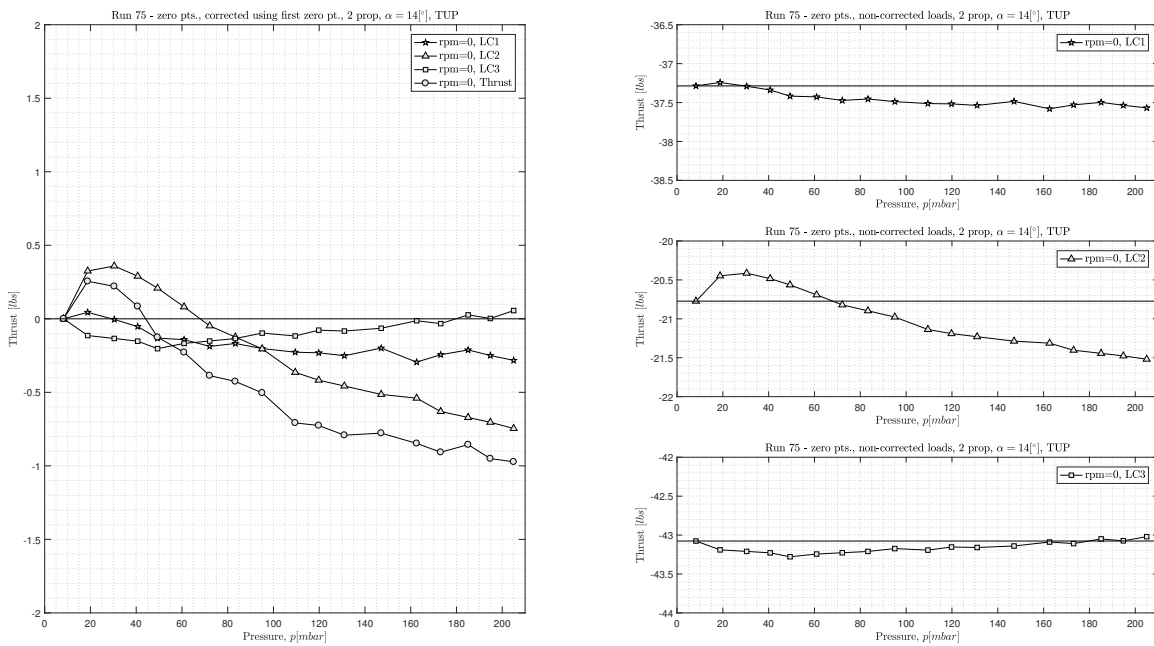


**Figure 7.1:** Thrust against pressure. *Left:* Corrected load cell and thrust zero points. *Right:* Uncorrected individual load cell zero points.

A jump occurs surprisingly at load cell 2 between 8 and 18 millibar. This corresponds to about a 5 degrees rise in motor temperature between points, unlike all the other data points. The load cells are located very close to the motor, see Fig.(4.1) and by its increase in temperature it may affect the performance of the load cells. A heat run (run 71) were done at 1013 millibar atmosphere where Fig.(7.2) shows an attempt to show if thrust is affected by the motor temperature during constant wing speed and pressure, but no effect were seen. It is likely to believe that at high pressures, the motor is cooled sufficiently but at 7 millibar, the cooling effects are significantly less. Unfortunately there were no heat run done at 7 millibar.

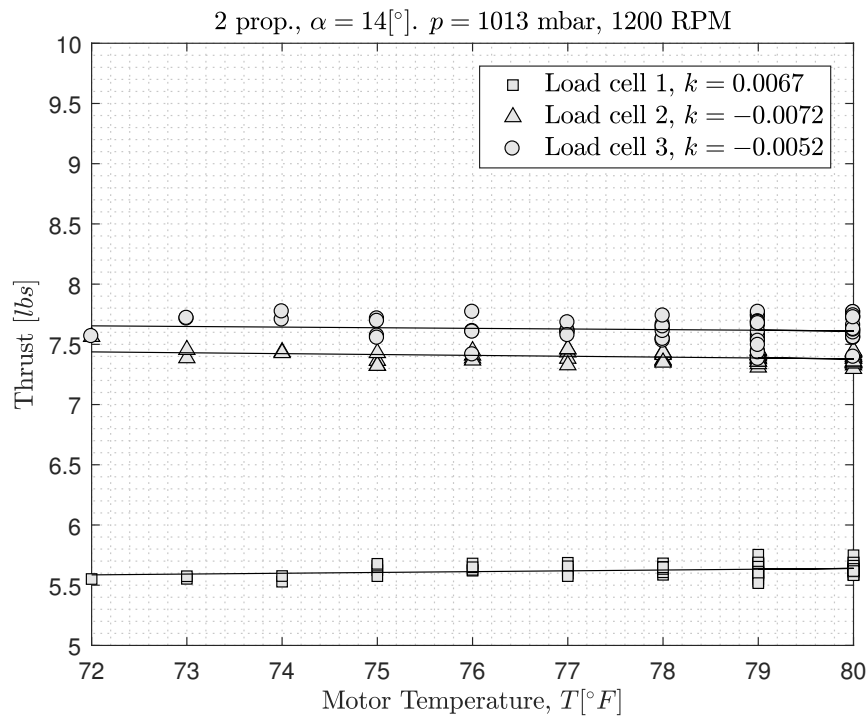


**Figure 7.2:** Thrust against motor temperature, heat run - run 71

Another interesting finding was the drift in thrust when the pressure were held constant at 7 millibar during run 26 and 34 respectively. A huge drift in thrust could be seen in Fig.(7.3) while the pressure was constant. This gives a clue that the load cell drifts are not or not only, due to pressure. This confirms the challenges in measuring the thrust at low pressures during the first testing in Fall 2016 that was discussed in Sec.(4.4). Due to results as these, is why the Spring testing occurred and the changes in test procedures.

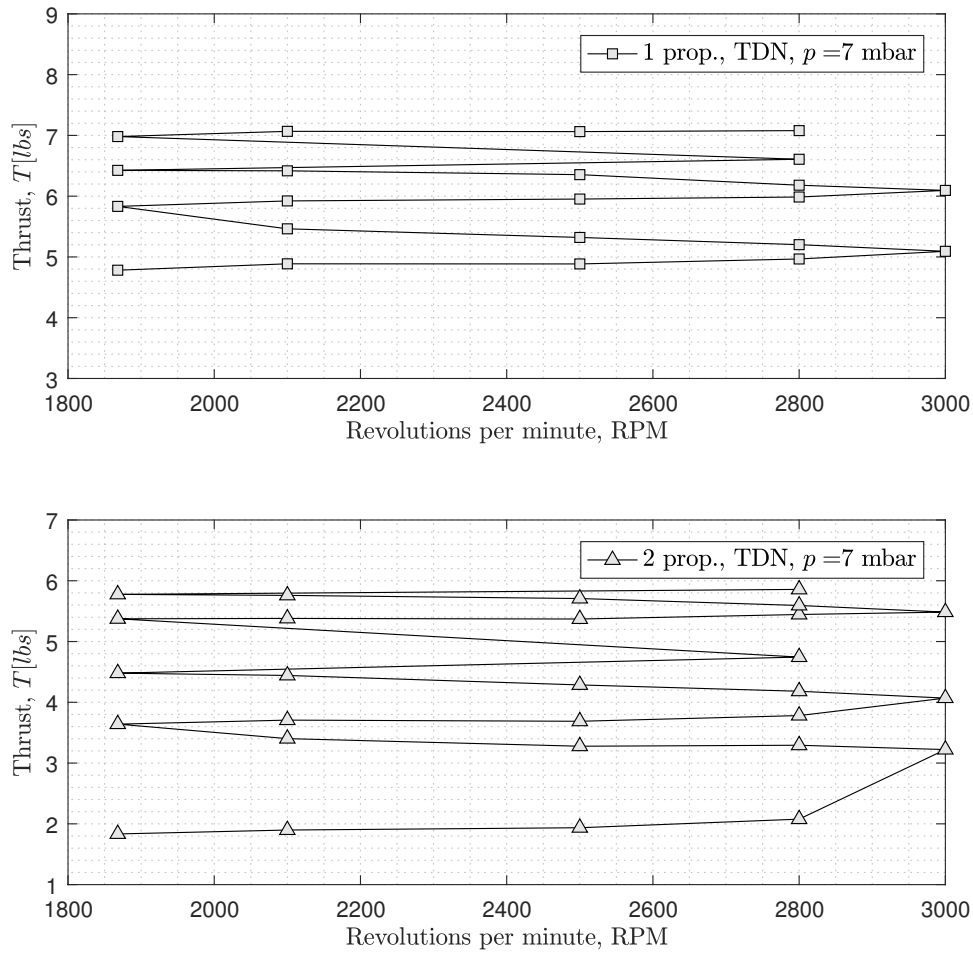


**Figure 7.3:** Thrust drift during RPM sweep at 7 millibar

A similar analysis as was done for pressure against thrust (Fig.(7.1)) was done for motor temperature and chamber temperature. Fig.(7.4) has motor temperature variation between 114 to 138 degrees Fahrenheit, and shows a similar behavior but is not very consistent looking at thrust from degree to degree. At 120 and 134 degrees Fahrenheit respectively, there is about 0.5 pounds in difference while barely no difference in thrust is seen at the two end points at 114 F and 120 F, a six degree difference. The chamber temperature shows a similar effect as well. The load cells shows barely no difference in thrust between 15-18 °C while the thrust decreases heavily between 18 and 20 °C.

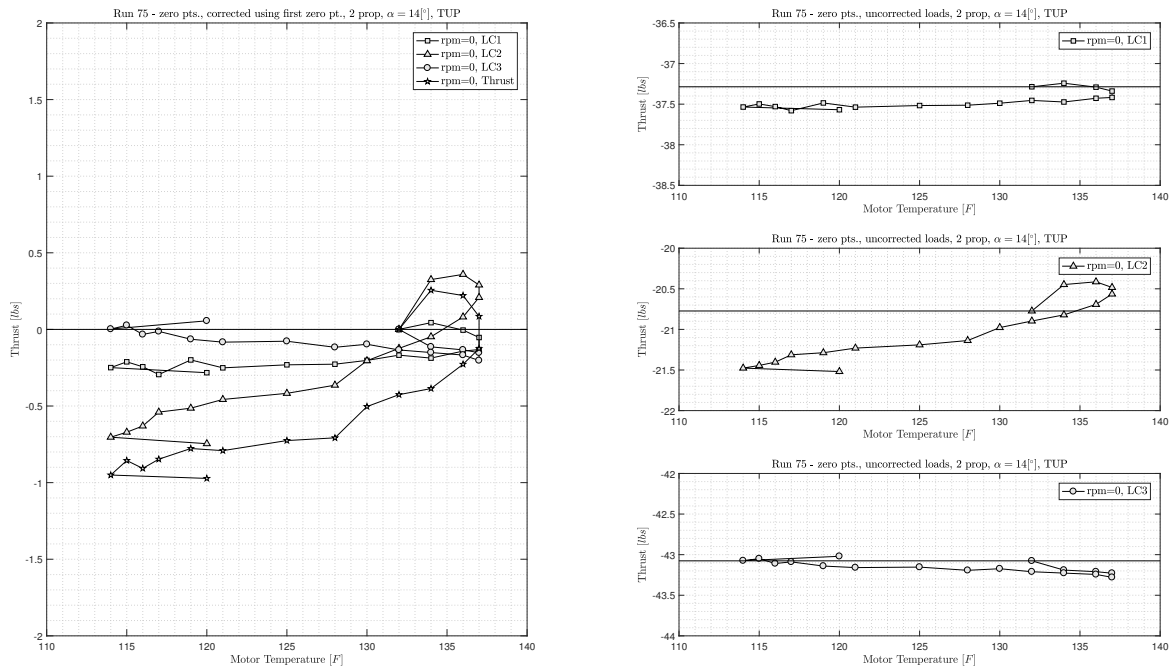


**Figure 7.4:** Thrust against motor temperature. *Left:* Corrected load cell and thrust zero points. *Right:* Uncorrected individual load cell zero points.

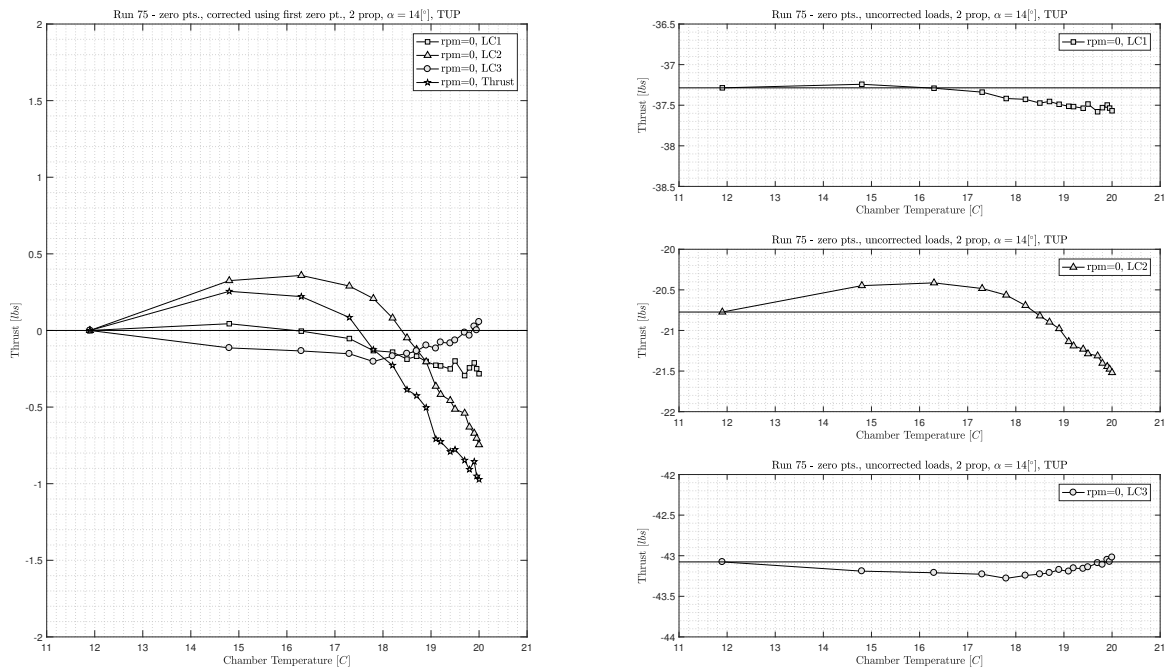


**Figure 7.5:** Thrust against chamber temperature. *Left:* Corrected load cell and thrust zero points. *Right:* Uncorrected individual load cell zero points.

### 7.1.2 Pressure effects

Two pump down runs using two rotors has been done, run 25 and 72. Run 25 was executed during the Fall testing and had the rotor configuration flipped by 180 degrees and was thrusting down with a rotor tilt of  $\alpha=-14$  [°], which is equivalent to  $\alpha=14$  [°] when thrusting up. The pressure was successfully dropped down to 7 millibar and covered the entire pressure range. Run 72 used a thrusting up configuration with a motor tilt of  $\alpha=14$  [°]. This run were less successful in pumping down the pressure but managed to pump down to 49 millibar. The reason why data is missing between 105 to 58.6 millibar is due to the data system's sudden inability to measure pressure below 103.5 millibar. Pressure were instead measured manually using a pressure gauge.

Fig.(7.6) shows that thrust approximately depends linearly on pressure. An important behavior is that the thrust turns negative when pressure drops below about 30-50 millibar, a behavior that is seen during both Fall and Spring testing. Also, TUP-configuration gives a steeper thrust curve, likely due to the presence of the motor setup located in the wake, whilst TDN-configuration avoid such effect.

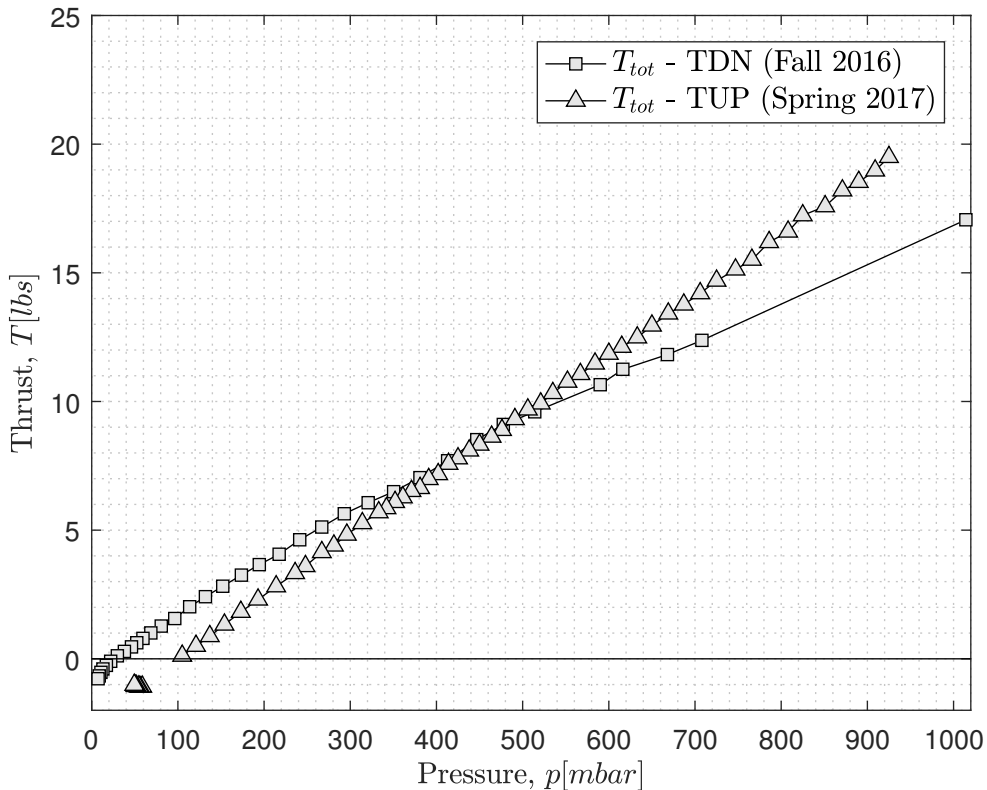


**Figure 7.6:** Depressurization, total thrust, 2 prop., 1250 RPM

Fig.(7.7) shows the rate of change in thrust against pressure and shows an almost

constant, close to zero, behavior except when pressure goes below about 50 millibar. Low pressure tendencies during Spring testing could not be fully evaluated since 7 millibar were never reached. Again difficulties is seen to measure the load near vacuum.

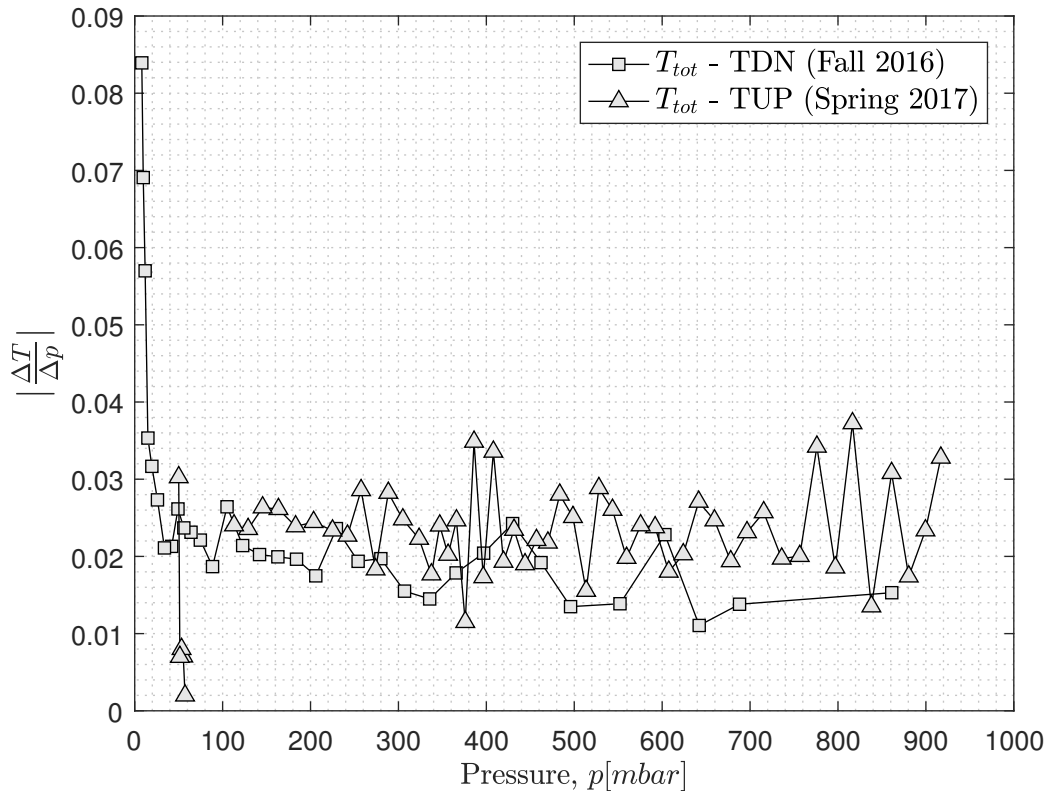


**Figure 7.7:** Depressurization, rate of change in thrust against pressure, 2 prop., TUP, 1250 RPM

Furthermore, as mentioned in Sec.(7.1.1) the pressure was successfully pumped down to 8 millibar during run 75, but could not be held constant. While the pressure were drifting up at a low pace, eighteen RPM sweeps were done ranging pressures from 8 to 200 millibar. There are two ways of correcting the data points. To see drift tendencies with validation over time, data is corrected using the initial starting point as reference to correct all remaining data points. To measure the actual values at the time, the reference point needs to be updated and a new reference point will be chosen each sweep. Fig.(7.8) used thrust data corrected using the first zero point in run 75. Besides a drift in consistency for all zero points, what is important, is that the roll moment,  $M_x$  is magnified. The roll moment value depends on the load cells output, and if the load cell readings are not valid at low pressures, the roll moment error will be magnified.

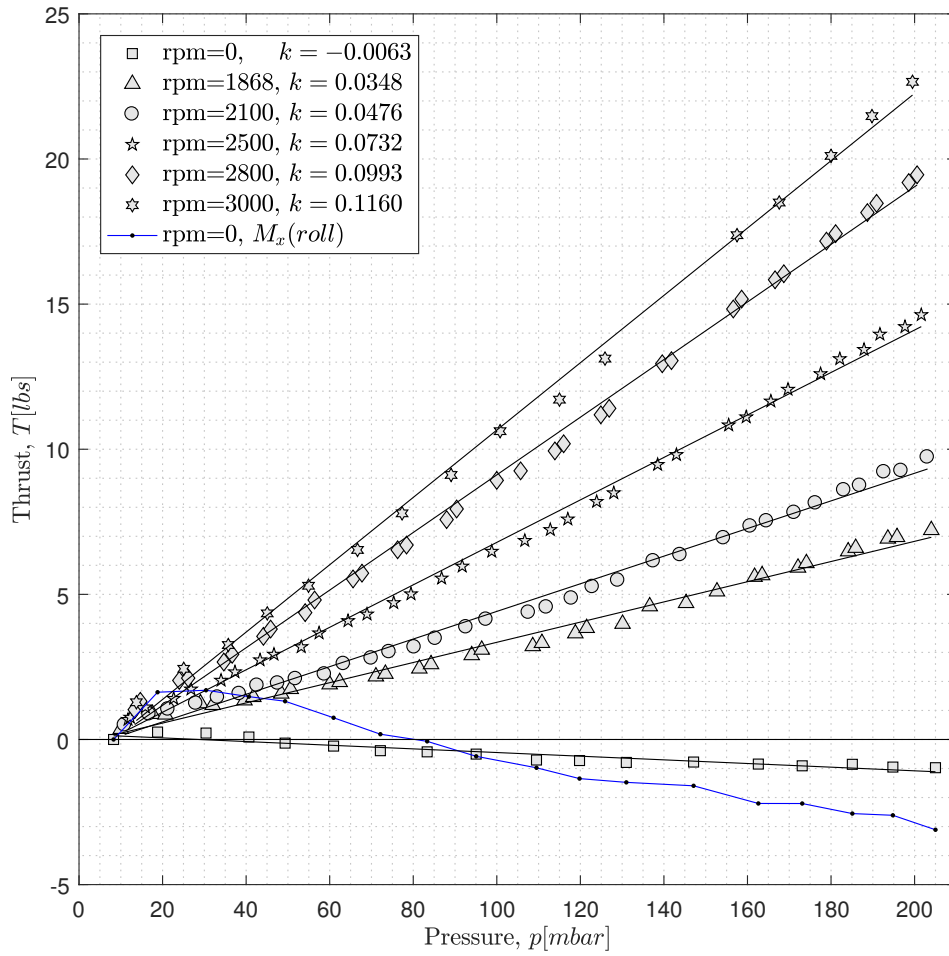


**Figure 7.8:** Thrust variation during low pressure RPM sweeps

When a new reference point is chosen for every RPM sweep, a more updated thrust is obtained. The thrust seems to be fairly linear against the pressure, and the delta thrust between the different RPM's is getting smaller the lower pressure it gets. The right picture in Fig.(7.9) is a zoomed in view of the left picture, pressure ranging from 8 to 50 millibar. Note the wave-like behavior of thrust as RPM changes.

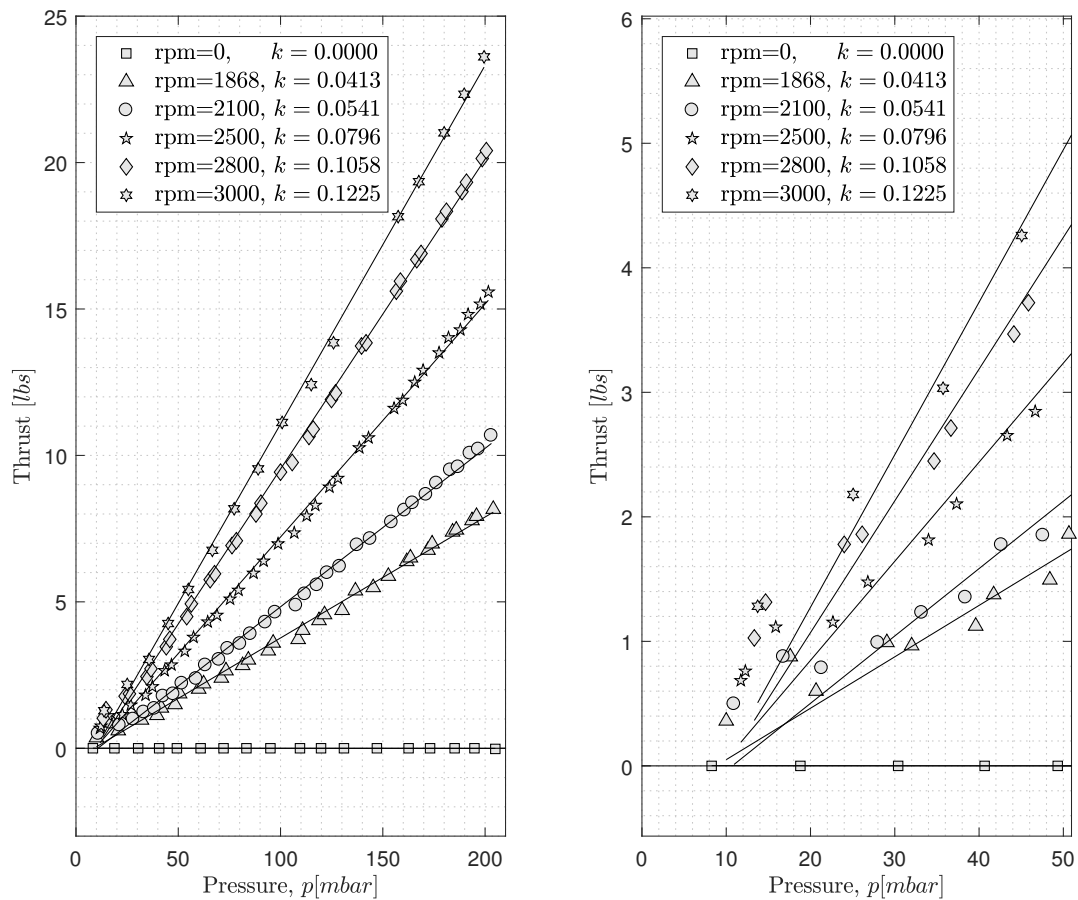


**Figure 7.9:** Thrust variation during low pressure RPM sweeps, zero pt. correction every RPM sweep

### 7.1.3 Temperature effects

When the pressure is decreased rapidly, the temperature do as well. Depressurization runs, 25 and 33, were both followed by a successful next run when the pressure was held at 7 millibar. RPM was held constant at 1250 during the two rotor run (run 26) and held constant at 1930 during the one rotor run (run 34). RPM sweeps were done during the latter mentioned runs, when pressure were held at 7 millibar. When the pressure is held, the temperature will not change due to pressure difference, but due to surrounding temperatures. Fig.(7.10) shows how temperature as well thrust decreases when the pressure is lowered from 1013 to 7 millibar at a  $\alpha = -14^\circ$  motor tilt, two and one rotors used respectively. The vertical line symbolizes the temperature when 7 millibar were reached, at 0 and 1.2  $^\circ C$  respectively. The thrust is still varying even after 7 millibar is reached, and proposes that temperature affects the load cells. Also strange and unexplained jumps was seen during both runs, which

occurred at different testing days, at about 8-10 °C for all load cells, especially for the one rotor run, seen in the right picture in Fig.(7.10).

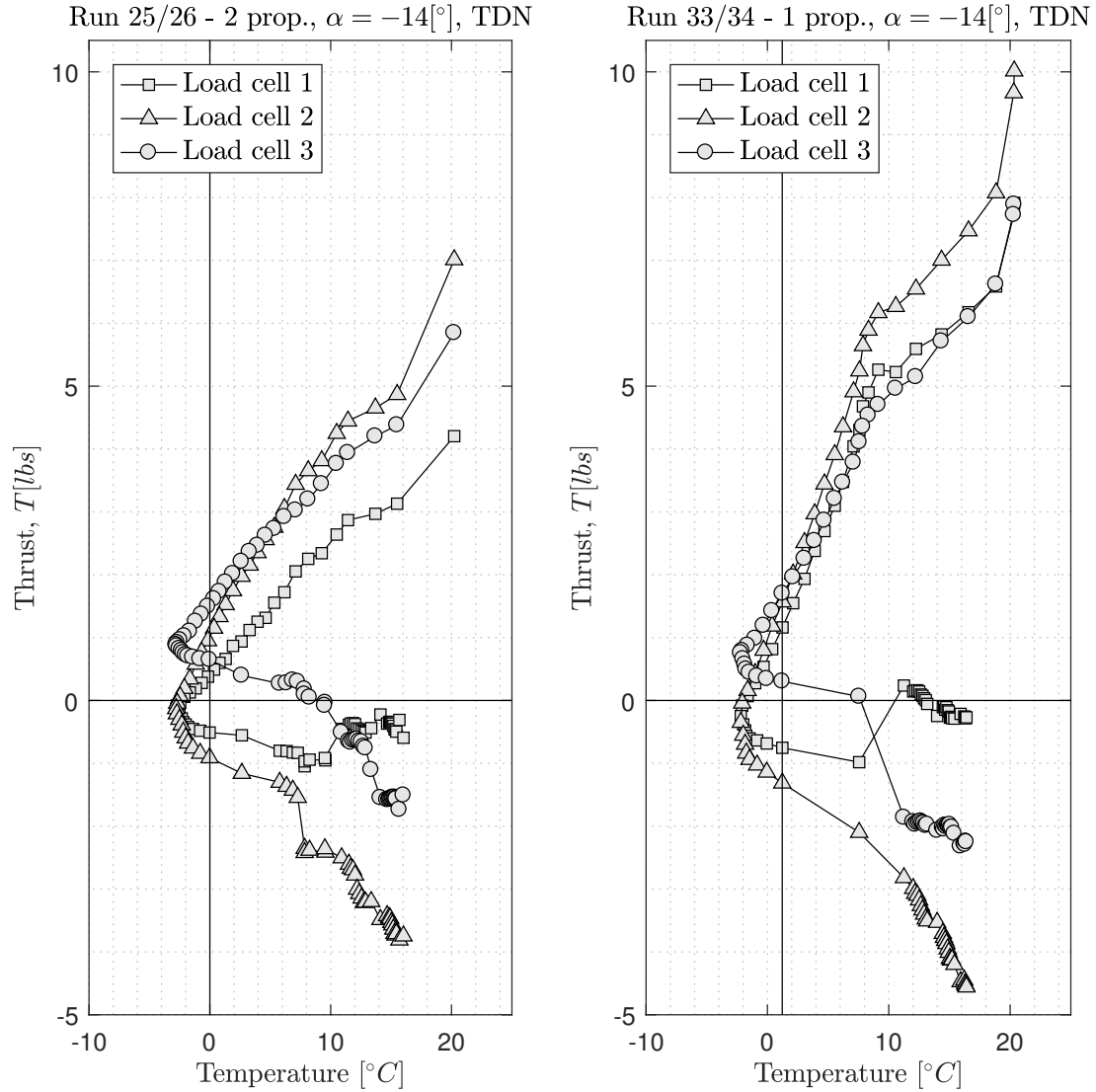


**Figure 7.10:** Temperature against pressure when pumping down and held pressure constant at 7 millibar

## 7.2 RotCFD Results

To understand RotCFD’s capability to reproduce low pressure simulations results and its validity, validation of the airfoil tables had to be done, to clarify their implementation correctly. Also comparing free field simulations to tunnel simulations to

spot potential wall effects and to see if RotCFD is capable of capturing such effects. Lastly the attempt to correlate a few points (see Sec.(6.4)) from the tunnel testing at Martian pressures with numerical results from RotCFD will be discussed.

### 7.2.1 Airfoil Tables comparison

A crucial part to get valid and reasonable results in RotCFD is to have valid airfoil tables. Sec.(6.2) covers what the airfoil tables contain. Each airfoil table is made for a specific pressure, meaning that Martian conditions requires its own airfoil table while Terrestrial atmosphere another. For comparison, four simulations were done to investigate what impact on the result the airfoil tables has. Two simulations for 7 millibar, one with the correct airfoil tables while the other with airfoil tables for 1013 millibar. Same approach for the 1013 millibar comparison. Tabs.(7.1),(7.2) displays converged variables of rotor performance, comparing the airfoil tables at 7 and 1013 millibar respectively.

Variable	7 mbar airfoil tables	1013 mbar airfoil tables	Delta
$C_{T1}$	0.0049	0.0121	0.0072
$C_{T2}$	0.0032	0.0078	0.0046
$T_1[N]$	0.84	2.058	1.218
$T_2[N]$	0.54	1.315	0.775
$Q_1[Nm]$	-0.121	-0.137	-0.016
$Q_2[Nm]$	-0.096	-0.115	-0.019
$P_{tot1}[W]$	38.06	43.26	5.2
$P_{tot2}[W]$	30.24	36.16	5.92
$P_{id1}[W]$	9.58	36.51	26.93
$P_{id2}[W]$	7.82	28.92	21.1
$P_{tot}/P_{ideal1}[\%]$	397	118	-279
$P_{tot}/P_{ideal2}[\%]$	387	125	-262

**Table 7.1:** Airfoil comparison, free field hover at  $p = 7mbar$ , 3000 RPM

Looking at the differences the tables, it can immediately be concluded that the airfoil tables affect the result significantly. The thrust generated using the 7 millibar airfoil tables is about 245% more and about 60% less for the 1013 millibar airfoil tables. Torque,  $Q$ , is less affected but still significant enough to give invalid results.

Variable	7 mbar airfoil tables	1013 mbar airfoil tables	Delta
$C_{T1}$	0.005	0.0122	0.0072
$C_{T2}$	0.003	0.0077	0.0047
$T_1[N]$	128.6	316.7	188.4
$T_2[N]$	83.4	203.1	119.7
$Q_1[Nm]$	-18.56	-21.05	-2.49
$Q_2[Nm]$	-14.7	-17.6	-2.9
$P_{tot1}[W]$	5830	6620	790
$P_{tot2}[W]$	4620	5532	912
$P_{id1}[W]$	1469	5588	4119
$P_{id2}[W]$	1198	4420	3222
$P_{tot}/P_{ideal1}[\%]$	397	118	-279
$P_{tot}/P_{ideal2}[\%]$	386	125	-261

**Table 7.2:** Airfoil comparison, hover at  $p = 1013mbar$ , 3000 RPM

## 7.2.2 Airfoil tables validation

In general, to decide whether the simulation is valid or not, it is possible to look at the different angles of attacks along the blades. The airfoil tables used are only valid for angles between  $-14^\circ$  to  $30^\circ$ , and for all other angles, the result will be based on the NACA 0012 airfoil. This requires, that the angle of attacks stays within this range during the simulation to conclude that the result obtained applies to the actual used rotor. See Sec.(6.2) for details. Since the blade performance values are calculated from a reference azimuth angle, and then averaged over the time, blade one and blade two give the same output, see Fig.(7.11). For a complete airfoil validation of the cases simulated, see Appendix B.

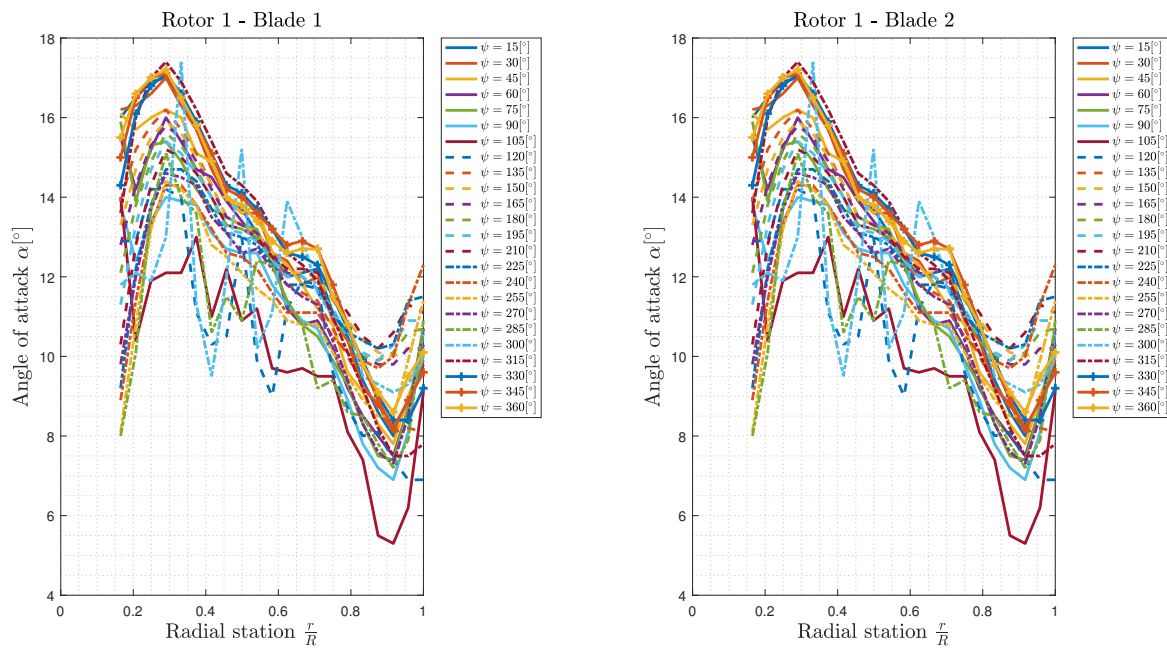


**Figure 7.11:** Over time averaged angle of attack, blade 1 and blade 2.

### 7.2.3 Free field hover

Simulating hover in an open air environment is useful for comparison to tunnel results, in the search for tunnel effects as well flow behavior. An RPM sweep free field hover case was simulated at 1013 millibar,  $0^\circ$  rotor tilt. The free field hover case simulated at 1868 RPM was chosen to show velocity vectors and pressure contours in the flow field about the rotors and is displayed in a plane between the two rotors, viewed from top, Fig.(7.12) and from the side, Fig.(7.13) to expose the rotor wake. The pressure contours clearly shows how the pressure is high below the upper rotor and low above the lower rotor in Fig.(7.12). The velocity vectors displays the circulating flow and how the magnitude of the velocity is greater outwards the radius compared to close to the center of rotation.

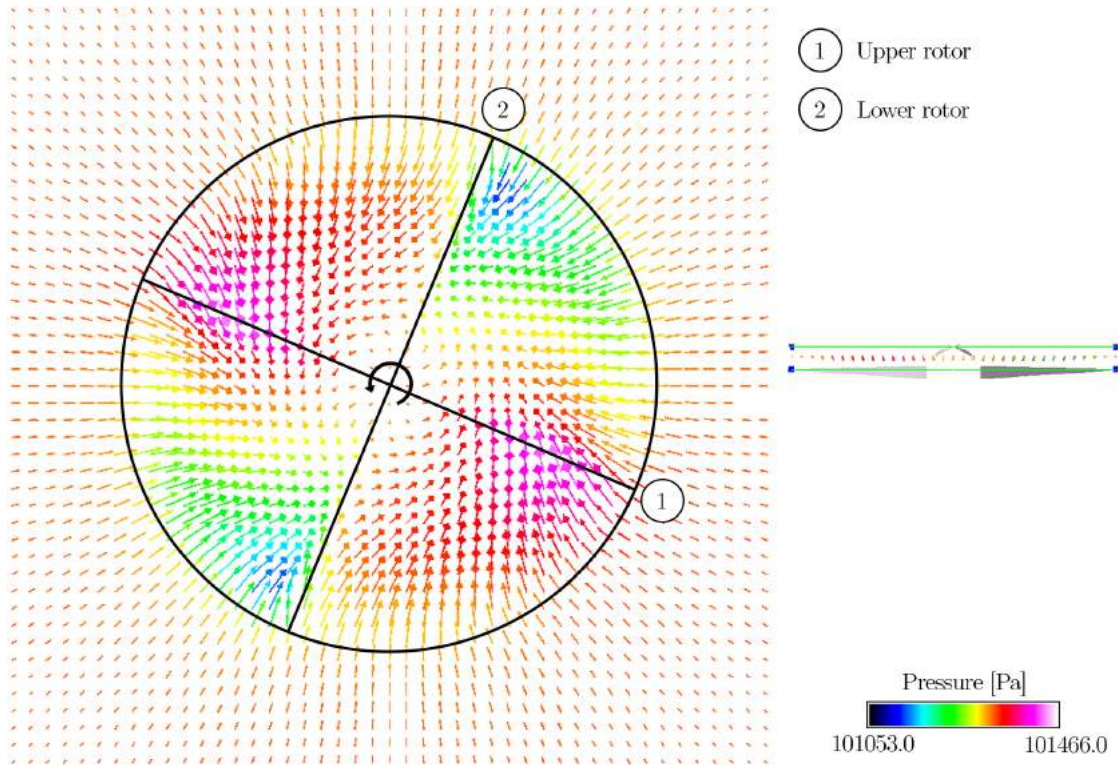


**Figure 7.12:** Velocity vectors with pressure contours between the rotors, free field hover

The path of the flow through the two rotors is visualized in Fig.(7.13). The induced flow at the wing tips due to tip losses were wagely seen from the top view more clearly shown here. It shows how the air is sucked in from the side and creates a circulation region due to the pressure difference.

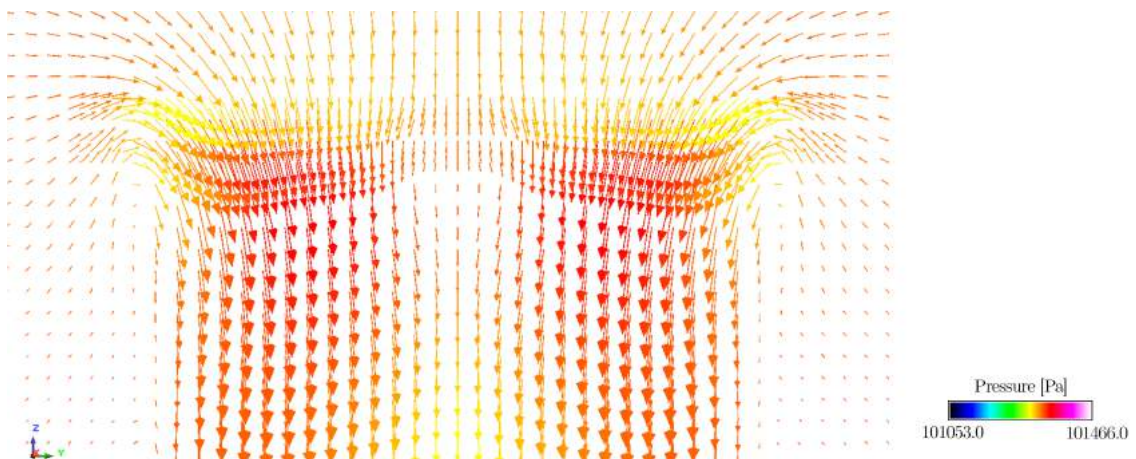


**Figure 7.13:** Velocity vectors with pressure contours from side, free field hover

Variable	1868 RPM	2100 RPM	2500 RPM	2800 RPM	3000 RPM
$T_1 [N]$	118.9	150.9	217.2	274.6	315.7
$T_2 [N]$	75.8	96.4	138.6	178.1	203.1
$T_{tot} [N]$	194.7	247.3	355.8	452.7	518.8

**Table 7.3:** Thrust at various rotor speeds, free field hover at  $p = 1013$  mbar

The converged thrust values for each rotor is displayed in Tab.(7.3) and plotted in Fig.(7.14) together with total thrust and a curve-fitted line against the squared RPM axis. The predicted thrust of the upper rotor increases more rapidly with rotor speed compared to the lower.

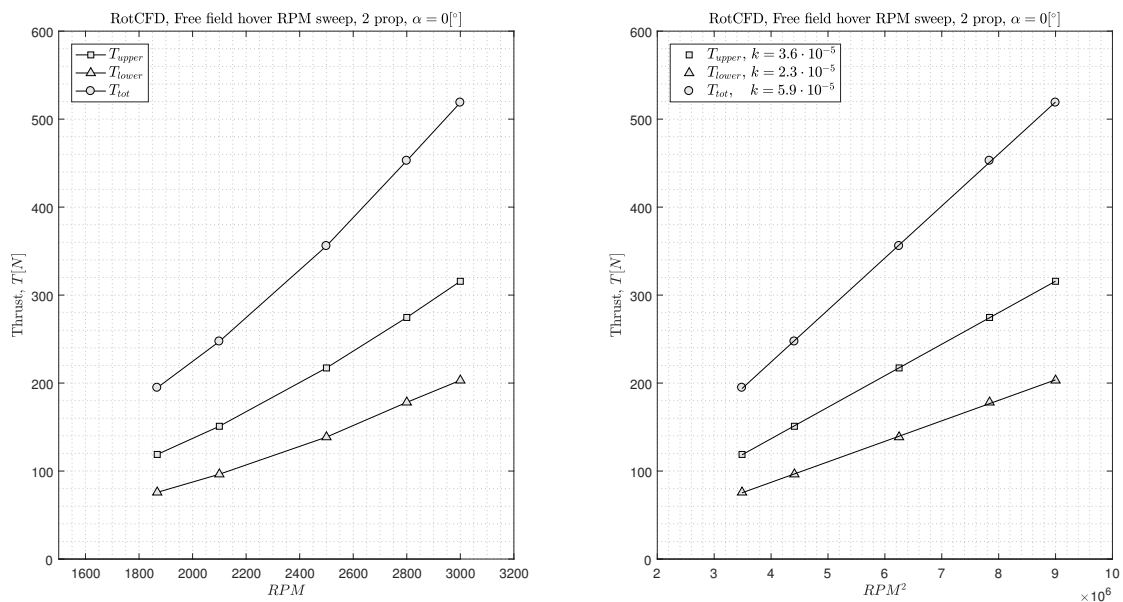


**Figure 7.14:** Free field, hover RPM sweep, RotCFD

The results seems reasonable. The closest RPM conducted in the wind tunnel runs at atmospheric pressure with two rotors was at 1200 RPM and corresponds to a thrust of 102  $N$  (run 71). According to the curve-fitted line for total thrust in Fig.(7.14), thrust at 1200 RPM free field, predicting with RotCFD, would correspond to  $\approx 73$   $N$ . Possible explanation of the delta thrust could be ground and wall effects from the tunnel as well numerical errors, which are kept in mind.

The velocity magnitude contour plot in Fig.(7.15) predict the flow wake below the rotor system, for 1868 and 3000 RPM respectively, after four seconds flow time. A maximum flow velocity of 33  $m/s$  were reached for 3000 RPM while 1868 RPM reached a maximum of  $\sim 20$   $m/s$ . Thus a  $\sim 65$  % increase in maximum velocity, increasing the angular velocity by 61 %.

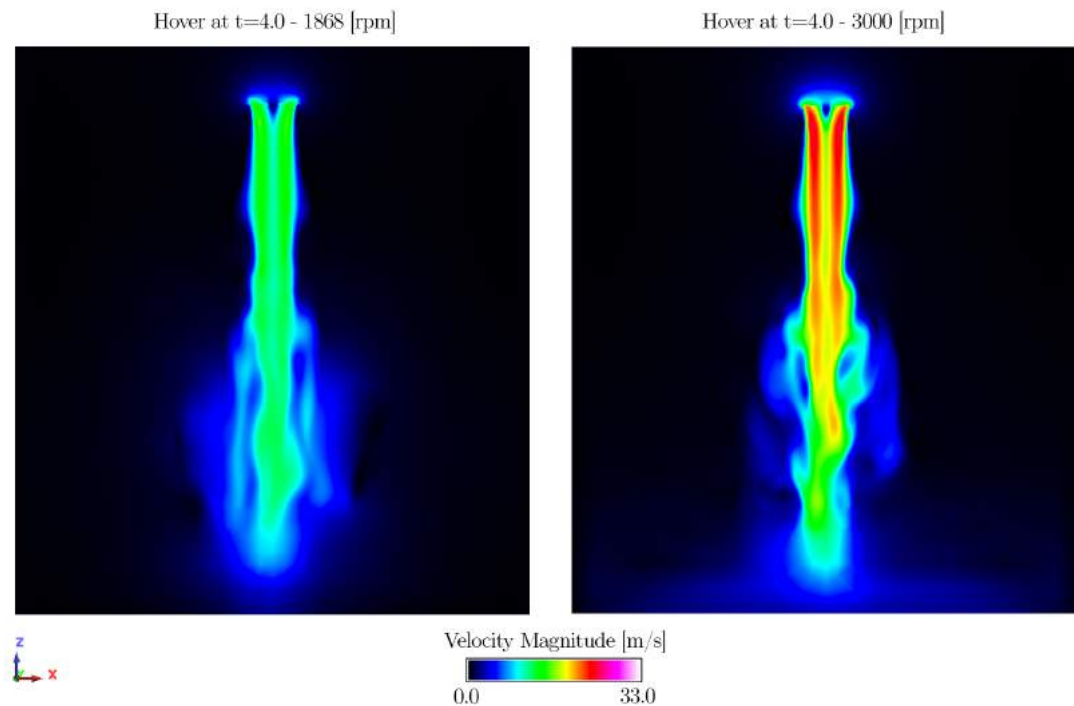


**Figure 7.15:** Velocity magnitude visualization, free field hover

#### 7.2.4 Tunnel effects

As a consequence, ground effect affects the rotor's aerodynamic performance, when simulating in a wind tunnel. Ground effect will lead to less power required to generate the same amount of thrust, as well as generate more thrust for the same power input. To explore how the results may differ, a free field and a tunnel simulation were done, both with a forward speed of  $3.5\text{ m/s}$ , at 7 millibar pressure. Delta values in Tab.(7.4) proposes that the tunnel effects at 7 millibar are negligible. Although a tunnel effect comparison were never done for 1013 millibar, where such effects are likely to be seen. Measuring the wind at 7 millibar was very difficult, and  $3.5\text{ m/s}$  was an approximated guess.

Variable	Free Field	Tunnel	Delta
$C_{T1}$	0.0042	0.0041	-0.0001
$C_{T2}$	0.0036	0.0037	0.0001
$T_1[N]$	0.72	0.71	-0.01
$T_2[N]$	0.61	0.61	0
$Q_1[Nm]$	-0.11	-0.11	0
$Q_2[Nm]$	-0.1	-0.10	0
$P_{tot1}[W]$	35.0	34.5	-0.5
$P_{tot2}[W]$	31.7	31.4	-0.3
$P_{id1}[W]$	8.93	8.53	-0.4
$P_{id2}[W]$	7.99	7.88	-0.11
$P_{tot}/P_{ideal1}[\%]$	391	404	13
$P_{tot}/P_{ideal2}[\%]$	397	398	1

**Table 7.4:** Tunnel effects,  $V_\infty=3.5$  m/s at  $p = 7\text{mbar}$ , 3000 RPM

### 7.3 Wind tunnel correlation

Additionally five tunnel runs were simulated, an RPM sweep at corresponding pressures, all with 3.5 m/s wind applied from the right boundary, downstream in  $x$ -direction, to be compared to experimental data, proposed in Sec.(6.4. Figs.(7.16),(7.17) treats the last proposed point to compare,  $p=13.73$  millibar at 3000 RPM. A maximum speed of 25.3 meters per second is obtained in the rotor wake, a relatively high speed despite the lowered pressure, compared to Fig.(7.15) in a free field environment. A similar behavior as in Fig.(7.13) is captured as well. Characteristic flow behavior such as the induced flow that causes tip losses and free stream effects are seen. The free stream drags the flow downstream, despite the low applied wind, seen in Fig.(7.17). As well the contour plot implies similar pressure characteristics with a maximum delta pressure of 0.12 millibar.

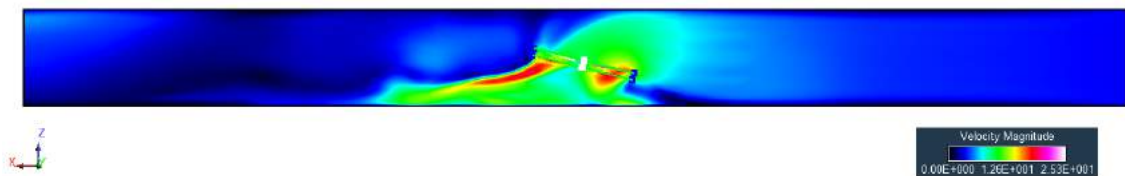


**Figure 7.16:** Velocity magnitude at  $p=13.73$  millibar,  $t=4$  s,  $\alpha = 14^\circ$ ,  $V_\infty=3.5$  m/s, 3000 RPM

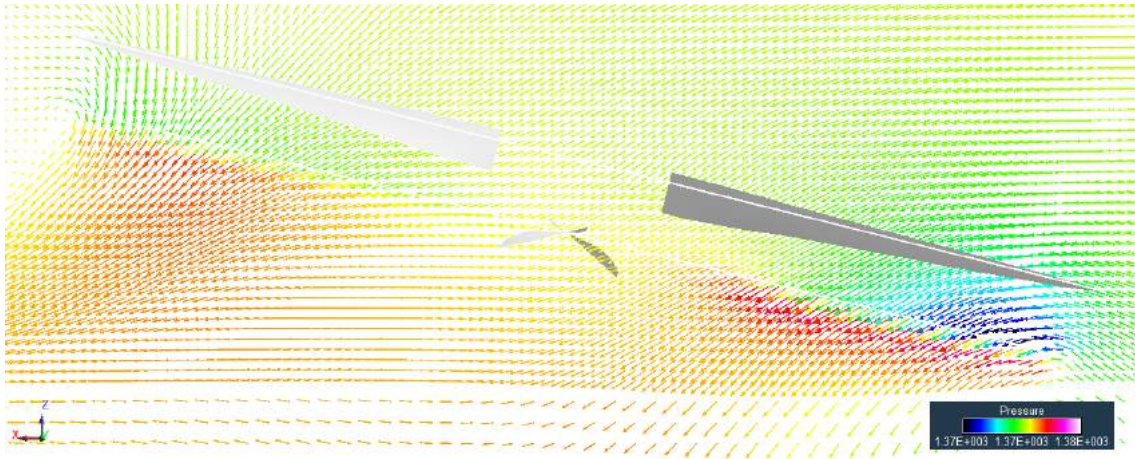


**Figure 7.17:** Velocity vectors with pressure contours at  $p=13.73$  millibar,  $t=4$  s,  $\alpha = 14^\circ$ ,  $V_\infty=3.5$  m/s, 3000 RPM

However the result was quite disappointing since data disagreed a lot, seen in Tab.(7.5). Only thrust data has been included but a similar behavior applied even for torque  $Q$  and power  $P$ . The thrust generated using RotCFD was about 54% less than the thrust from the experimental results. Also the increase in thrust against  $\text{RPM}^2$  (see curve-fitted slope) tend to decrease by a factor 2 in the numerical predicted thrust according to Fig.(7.18).

RPM	p (mbar)	$T_1$ [N]	$T_2$ [N]	$T_{tot,exp}$ [N]	$T_{tot,num}$ [N]
1860	9.99	0.34	0.32	1.61	0.66
2089	10.93	0.54	0.46	2.21	1.00
2483	12.27	0.88	0.75	3.38	1.63
2780	13.33	1.08	0.94	4.58	2.16
2976	13.73	1.38	1.18	5.70	2.68

**Table 7.5:** Correlation study, including numerical predicted thrust

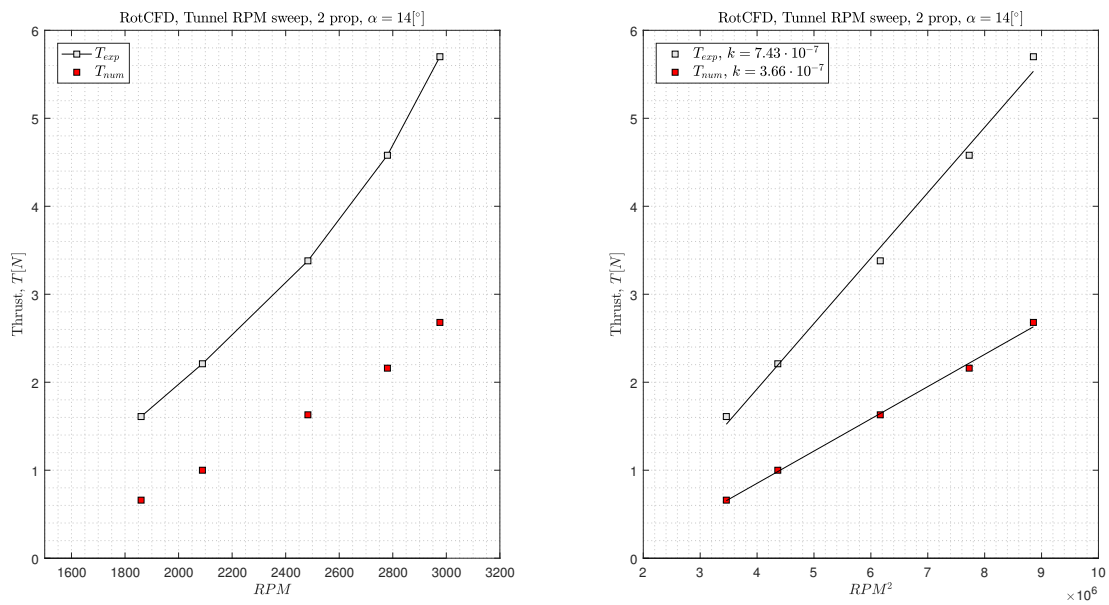


**Figure 7.18:** Experimental and numerical thrust prediction, tunnel at low pressure, RPM sweep, RotCFD

This may be due to a few reasons. Firstly, RotCFD's modeling ability may have been insufficient as well the grid might have been too coarse to capture all flow effects. Else, the RotCFD setup might have had errors as well. Secondly, the correct wind to be applied was not certain. Though the wind effect is likely not that significant to affect the thrust this much however. Lastly, it is difficult to conclude whether it is RotCFD or the experimental hardware setup that is incapable of acquire accurate data since the load cells tend to drift and are unable to read properly at these low pressures.



# 8

## Conclusions and Recommendations

### 8.1 Conclusions

Throughout the research, a recurring conclusion are the many difficulties of performing valid low pressure simulations. Issues with the hardware setup keeps occurring and inability to capture accurate data at pressures near vacuum have been seen. Load cells drifts may depend on multiple variables such as pressure, thermal heating, manufacturing errors, damaged load cells or using not enough sensitive load cells - likely a combination. Inconsistencies were particularly seen during the Fall testing 2016 such as the direction of rotor thrust changed in opposite direction when pressure went below  $\sim 30$  millibar. Due to a multitude of changing variables (discussed in Sec.(4.4)), there were difficulties to develop trends and conclusions when lowering the pressure to 7 millibar and a new testing procedure were necessary.

It was discovered that increased pressure increases lift a lot faster than an increase in rotor rotational speed as Fig.(7.9) implies. Although, the pressure at the landing sites is surely nothing that can be changed. Are there potential landing sites in depths with higher pressures on Mars? Will Mars's atmospheric pressure ever rise? One can only be optimistic for an increase. Considering the thin atmosphere at Mars, Tab.(7.4) proposes that wall and ground effects in the wind tunnel at such low pressure are negligible. Also the ability to measure the wind speed faded when the wind tunnel was depressurized. The pitot tube gave unreasonable velocity outputs and it turned out that it is very hard to measure wind speeds at 7 millibar.

The results in RotCFD did not match the experimental data and was quite disappointing, and reasons why may be many. Divergence may be due to an inability to replicate the case correctly in RotCFD, RotCFD's incapability to model the turbulence at low pressures or usage of a too coarse grid. Furthermore, the tunnel velocity at 7 millibar was not certain and there might have been velocity effects that affected the results. Another theory is that RotCFD actually did some fine modeling but the results acquired in the experimental testing were not correct. Likely to believe,

due to the inability to acquire accurate data at the lowest pressures. Overall, many factors make it hard to conclude whether errors lie in the testing facility or RotCFD. Since the experimental data could not be confidently stated that it was acquired accurately, it is very hard to conclude RotCFD's capability to reproduce experimental testing under Martian conditions.

In summary, to conduct accurate wind tunnel tests is itself a hard thing to do and requires a hi-tech facility. Then considering simulation at Mars instead of Earth, predicting aerodynamic performance for aerial vehicles under Martian conditions, makes the whole process even more complex.

### 8.2 Recommendations

Simulating Martian conditions seems to be more complex than expected. For future Martian testing, a suggestion would be to look for more suitable and hi-performing hardware that could match such conditions. The hardware used were not always the newest technology in its branch.

To conclude if thermal heating affects the load cells, several things could be done. Firstly, heat up the motor at constant RPM until temperature no longer changes, then depressurize and look for drifts in the data. Also possible, perform a heat run at 7 millibar when rotor cooling is significantly less for motor temperature effects. Lastly, heat up the load cells manually at 1013 millibar without the motor running to look for load cell drifts. For pressure effects, acquire zero points during a depressurization run, covering the entire pressure range.

Furthermore, a depressurization run without the motor running could lead to accurate wind speed measurements. By recording the load cells, while only pressure is changing, should give a perception of drift effects due to changing pressure since there will be no mechanical hysteresis nor thermal heating effects. Also, an intriguing next step, provided pitot tube measurements problems are solved, would be investigating free stream effects at 7 millibar, free field and tunnel, which were never done. To further conclude the presence of wall effects using RotCFD, discussed in Sec.(7.2.4), more effort is needed. A tunnel effect comparison was never done for 1013 millibar, where such effects are more likely to be seen. That would raise the possibility to show an immense effect, provided modeling is done correctly. An encouraging idea that could conclude that wall effects during testing under Martian conditions are negligible.

Will it be possible to simulate helicopter forward flight under Martian conditions? Many questions remain to be answered whether aerial vehicles can operate on Mars or not. Till then, human curiosity will lead us further towards the understanding of exploration on Mars.

# Bibliography

- [1] Young, L.A., Aiken, E. W., Derby, M. R., Johnson, J. L., Navarrete, J., Klem, J., Demblewski, R., Andrews, J. and Torres, R. “Engineering Studies into Vertical Lift Planetary Aerial Vehicles”, AHS International Meeting on Advanced Rotorcraft Technology and Life Saving Activities, Tochigi, Japan, November 2002.
- [2] Young, L. A., Aiken, E. W., Derby, M. R., Demblewski, R., and Navarrete, J., “Experimental Investigation and Demonstration of Rotary-Wing Technologies for Flight in the Atmosphere of Mars”, Proceedings of the 58th Annual Forum of the American Helicopter Society, Montreal, Canada, June 2002.
- [3] Koning W.J.F, “Wind Tunnel Interference Effects on Tilt Rotor Testing Using Computational Fluid Dynamics”, Master’s thesis at TU Delft, The Netherlands, 2015. Published.
- [4] Szolnoky Cunha, F., “Momentum Theory in Hover”, Instituto Superior Tecnico.
- [5] Helitek, S., “Rotor UNStructured Solver Application RotCFD Version 0.9.15(Beta) Build 401”, Ames, Iowa, November 2016
- [6] <https://mars.nasa.gov/mars2020/mission/timeline/prelaunch/landing-site-selection/>, NASA Mars Rover 2020 Website.
- [7] Corfeld, K., Strawn, R., and Long, L., “Computational Analysis of a Prototype Martian Rotorcraft Experiment”, 20th AIAA Applied Aerodynamics Conference, AIAA-2002-2815, St. Louis MO, June 2002.
- [8] Benedict, M., Winslow, J., Hasnain, Z., and Chopra, I., “Performance and Flowfield Measurements of a MAV-Scale Helicopter Rotor in Hover”, 70th American Helicopter Society Annual Forum, Montreal, Quebec, Canada, May 2014.
- [9] Selig, M. S., Deters, R. W., and Williamson, G. A., “Wind Tunnel Testing Airfoils at Low Reynolds Numbers”, 49th AIAA Aerospace Sciences Meeting, Orlando, FL, January 2011.

- [10] Rajagopalan, R.G., Baskaran,V., Hollingsworth, A., Lestari, A., Garrick, D., Solis, E., Hagerty, B., “RotCFD - A Tool for Aerodynamic Interference of Rotors: Validation and Capabilities”, AHS Future Vertical Lift Aircraft Design Conference, San Francisco CA, January 2012.
- [11] Dr. W. Warmbrodt, “Private Correspondence” NASA Ames Aeromechanics Department, Moffett Field, 2017.
- [12] Klein, H.P.; et al. (1992). “The Search for Extant Life on Mars”. In Kieffer, H.H.; Jakosky, B.M.; Snyder, C.W.; et al. Mars. Tucson: University of Arizona Press
- [13] [www.nasa.gov/](http://www.nasa.gov/), [www.mars.nasa.gov/](http://www.mars.nasa.gov/), [www.grc.nasa.gov/](http://www.grc.nasa.gov/), “NASA Online Database”, National Aeronautics and Space Administration, USA
- [14] Dr. S. Suman, “Notes from the Turbulence Modeling course”, Indian Institute of Technology, New Delhi, 2016
- [15] “Helicopter Flying Handbook”, U.S Department of Transportation, Federal Aviation Administration, 2012
- [16] McCoy, M., Wadcock, A.J., “Documentation of the Recirculation in a Closed-Chamber Rotor Hover Test”, NASA Ames Research Center, Moffett Field, August 2016
- [17] Grip., H.F., “Mars Helicopter: Guidance, Navigation, and Control”-seminar, NASA Ames Research Center. American Helicopter Society San Francisco Bay Area, 2017.

# A

## Appendix 1 - RotCFD Run Overview

## A.1 1013 millibar, free field - rpm sweep

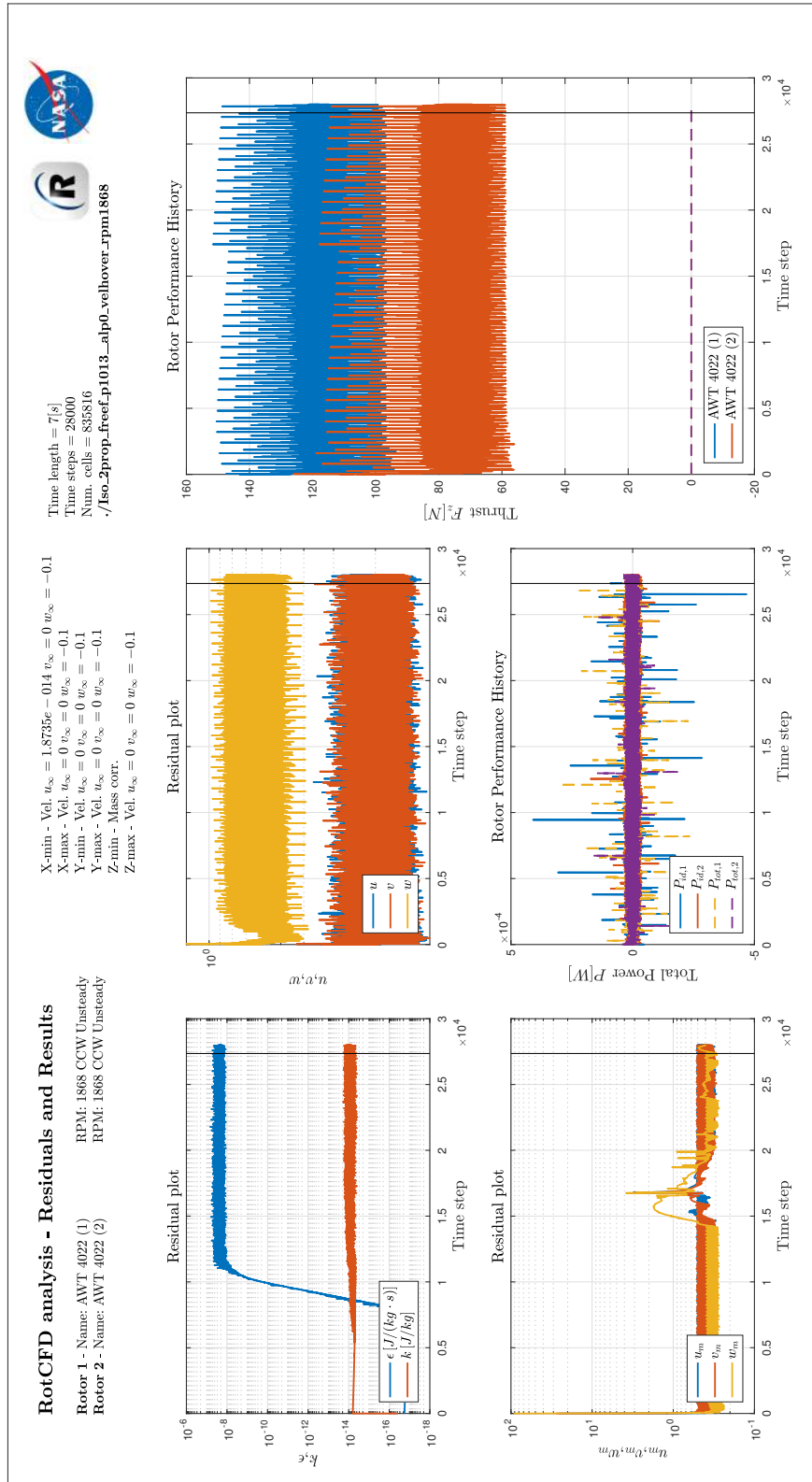


Figure A.1: 2 props, free field,  $p = 1013$  mbar,  $RPM = 1868$ ,  $\alpha = 0^\circ$

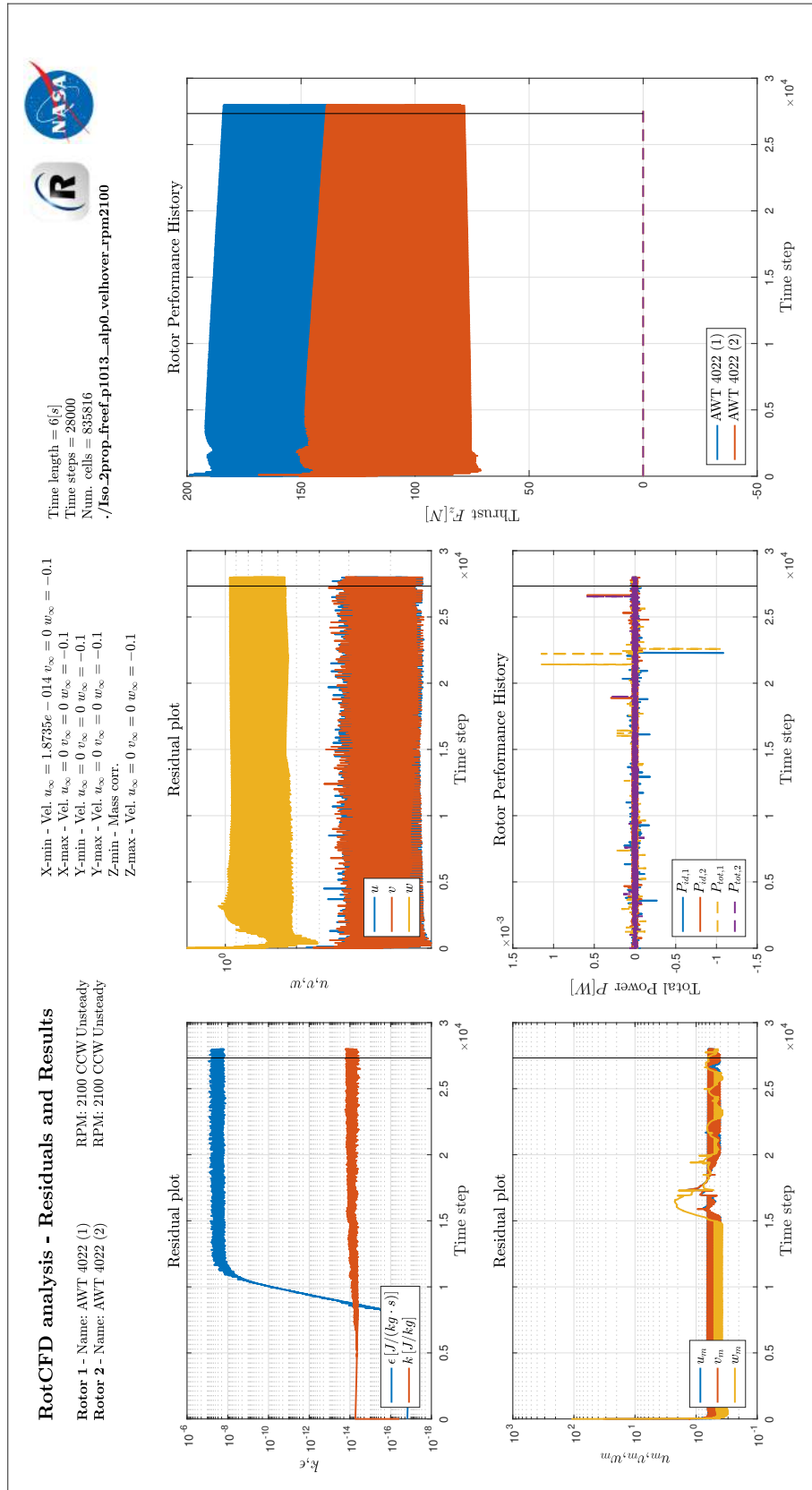


Figure A.2: 2 props, free field,  $p = 1013$  mbar,  $RPM = 2100$ ,  $\alpha = 0^\circ$

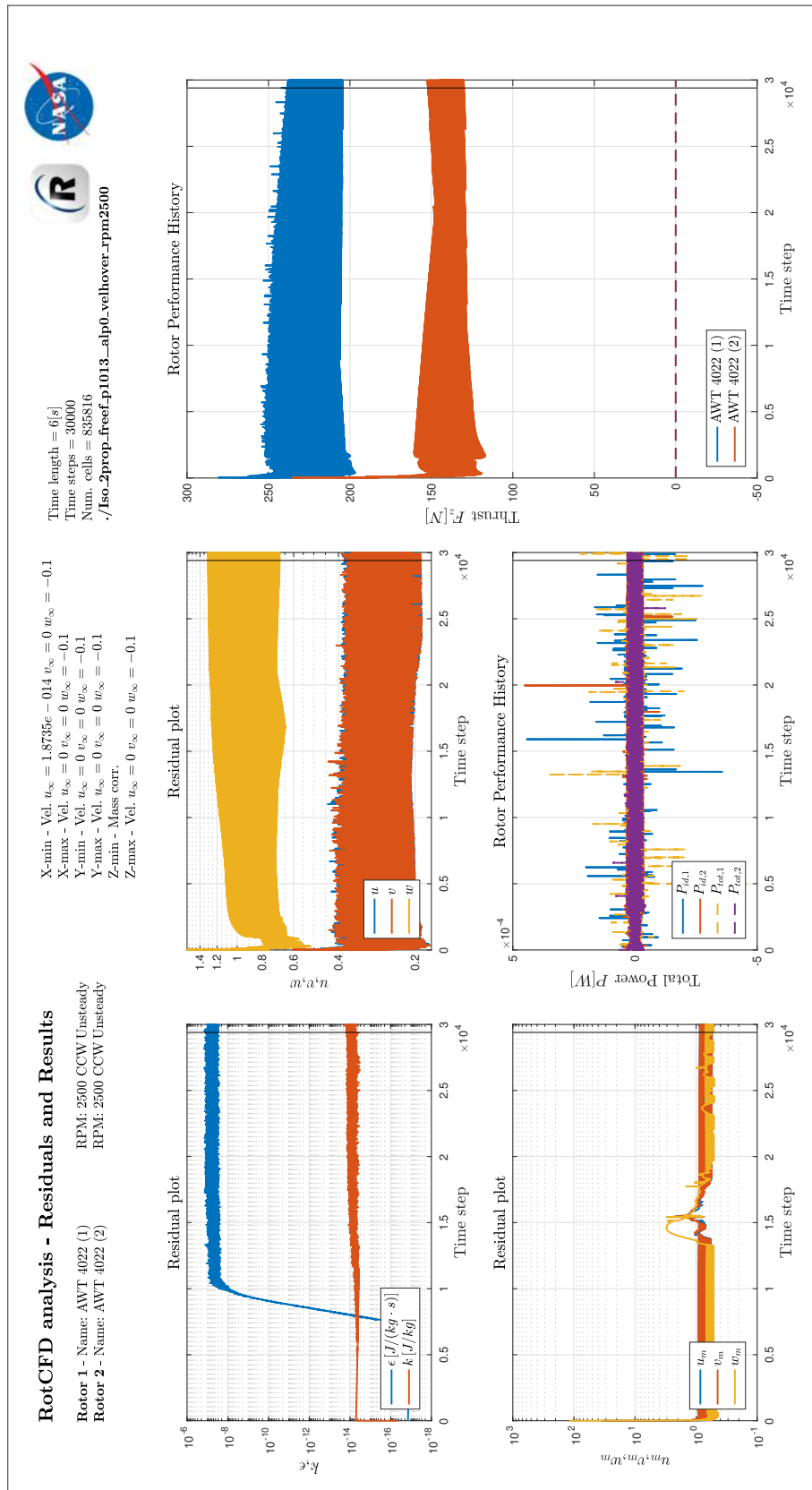


Figure A.3: 2 props, free field,  $p = 1013$  mbar,  $RPM = 2500$ ,  $\alpha = 0^\circ$

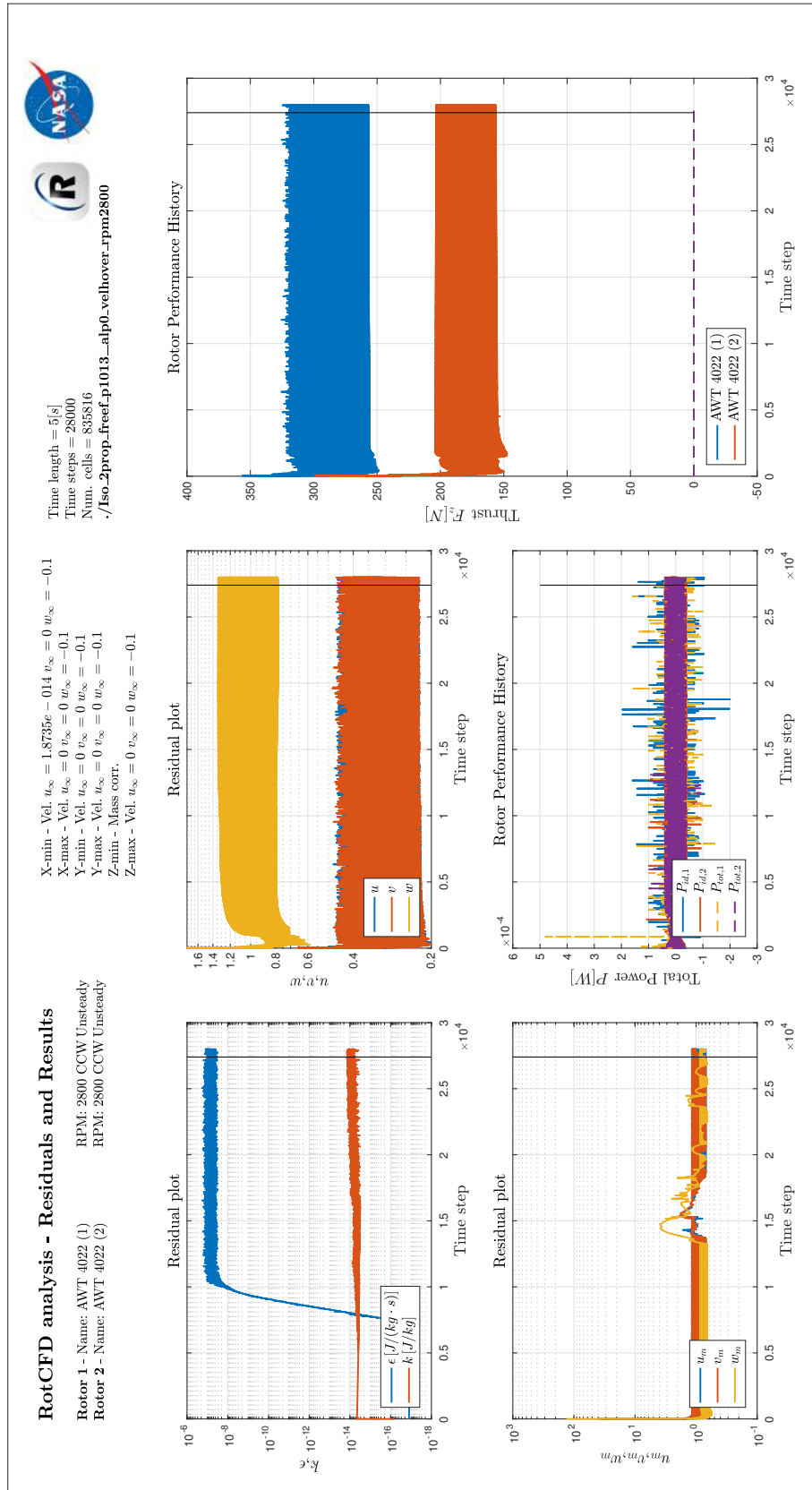


Figure A.4: 2 props, free field,  $p = 1013$  mbar,  $RPM = 2800$ ,  $\alpha = 0^\circ$

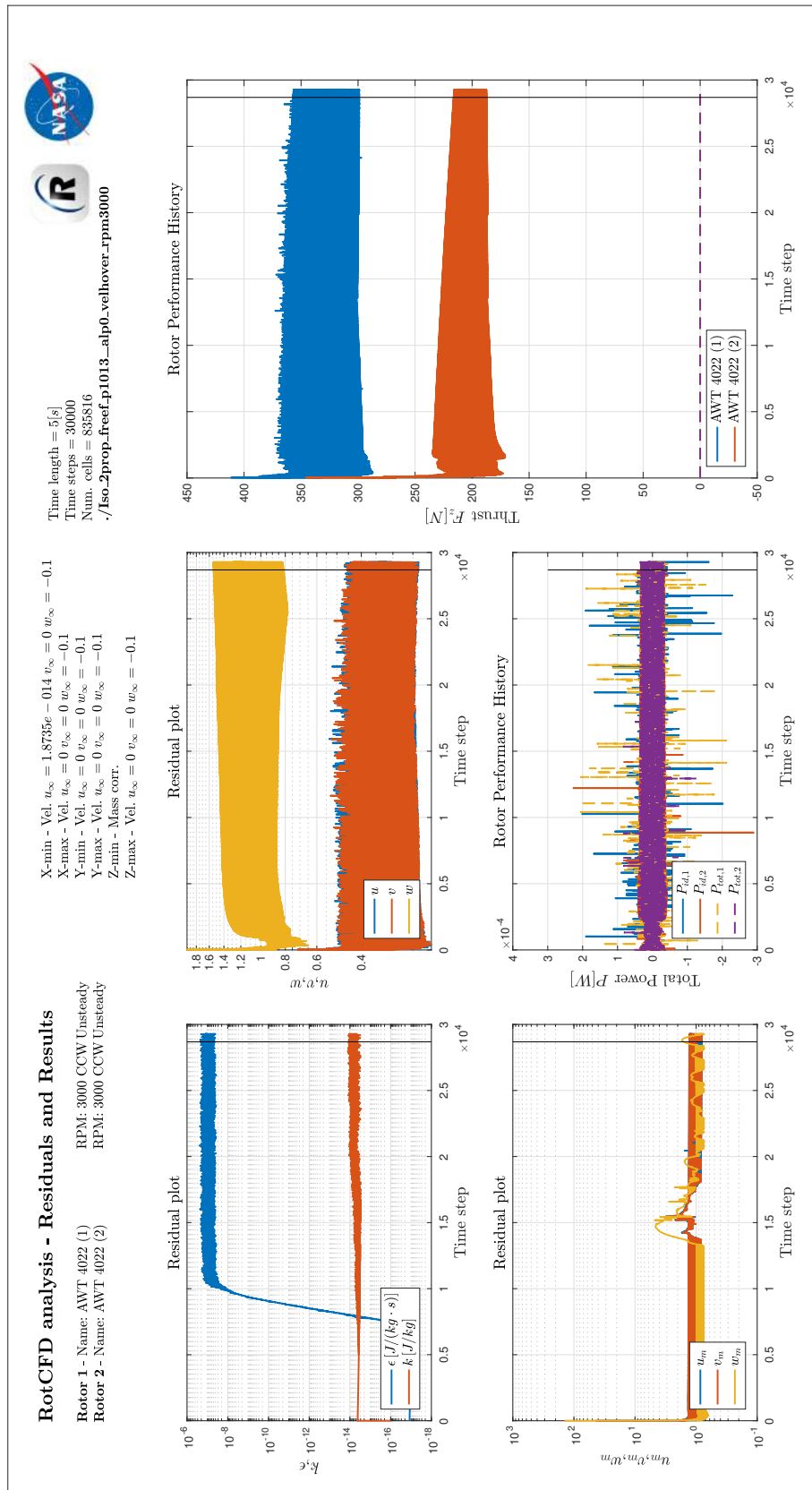


Figure A.5: 2 props, free field,  $p = 1013$  mbar,  $RPM = 3000$ ,  $\alpha = 0^\circ$

## A.2 Airfoil Tables comparison

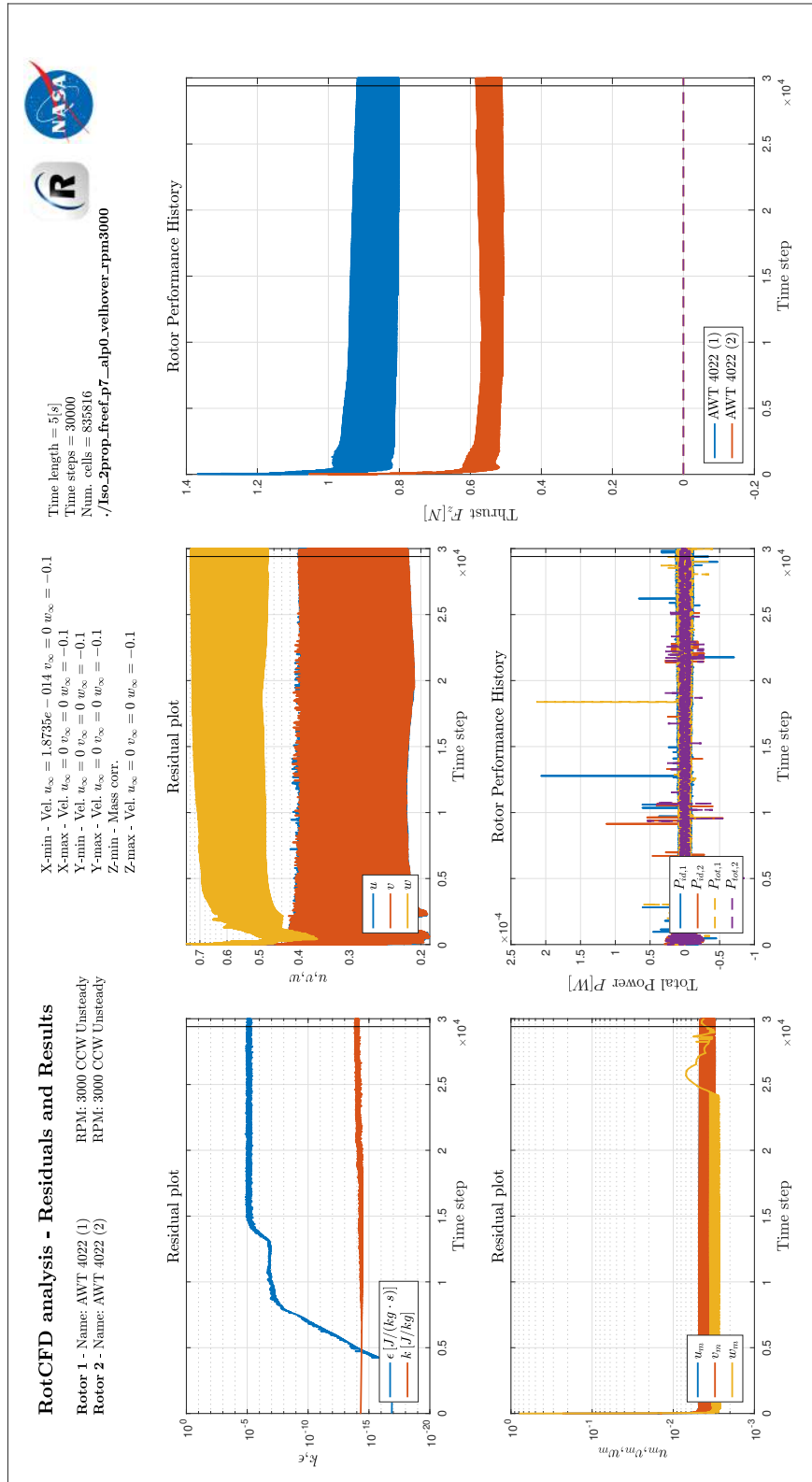


Figure A.6: 2 props, free field,  $p = 7$  millibar,  $RPM = 3000$ ,  $\alpha = 0^\circ$

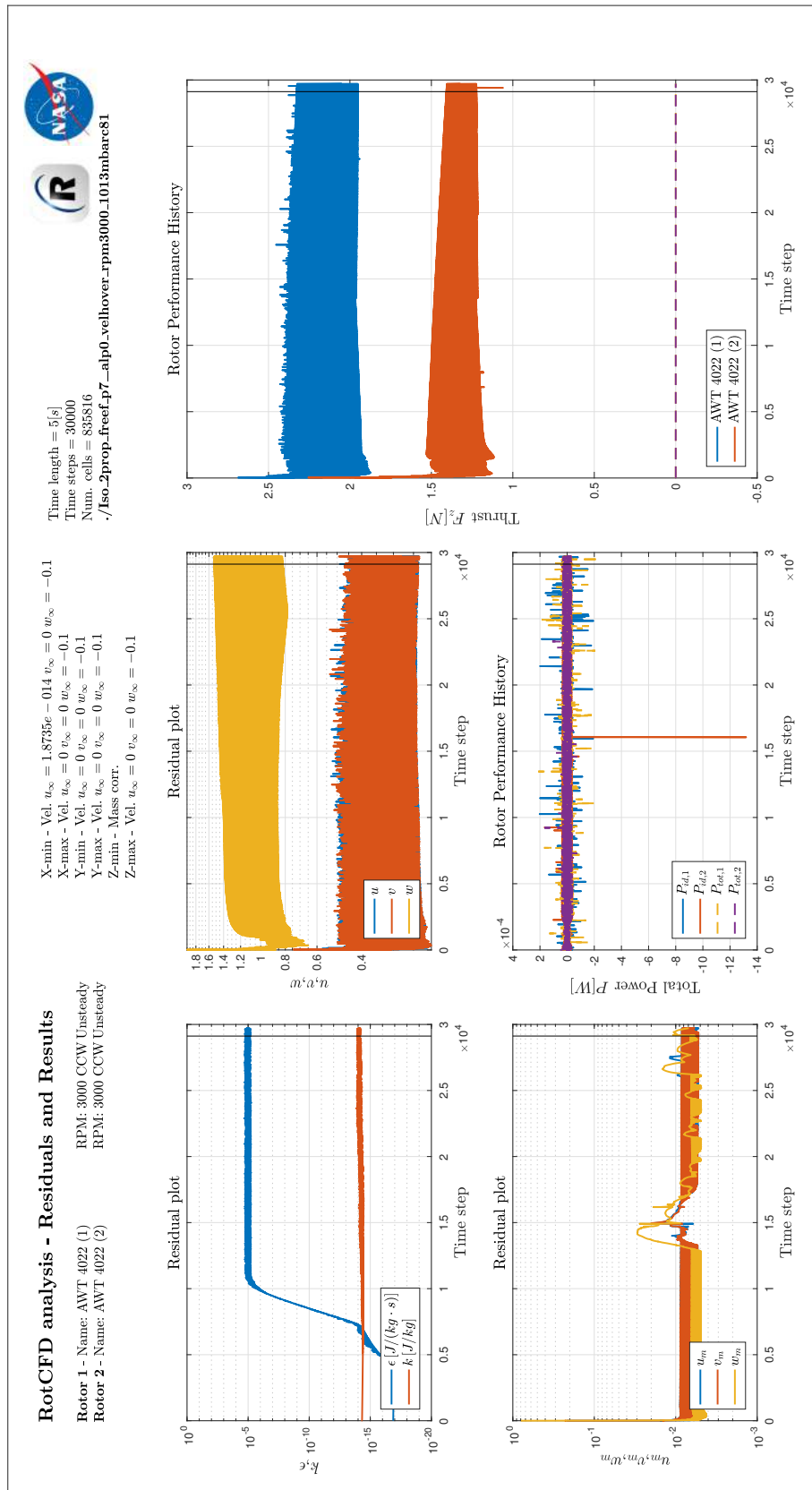


Figure A.7: 2 props, free field,  $p = 7$  millibar,  $RPM = 3000$ ,  $\alpha = 0^\circ$ , using 1013 mbar irfoil tables

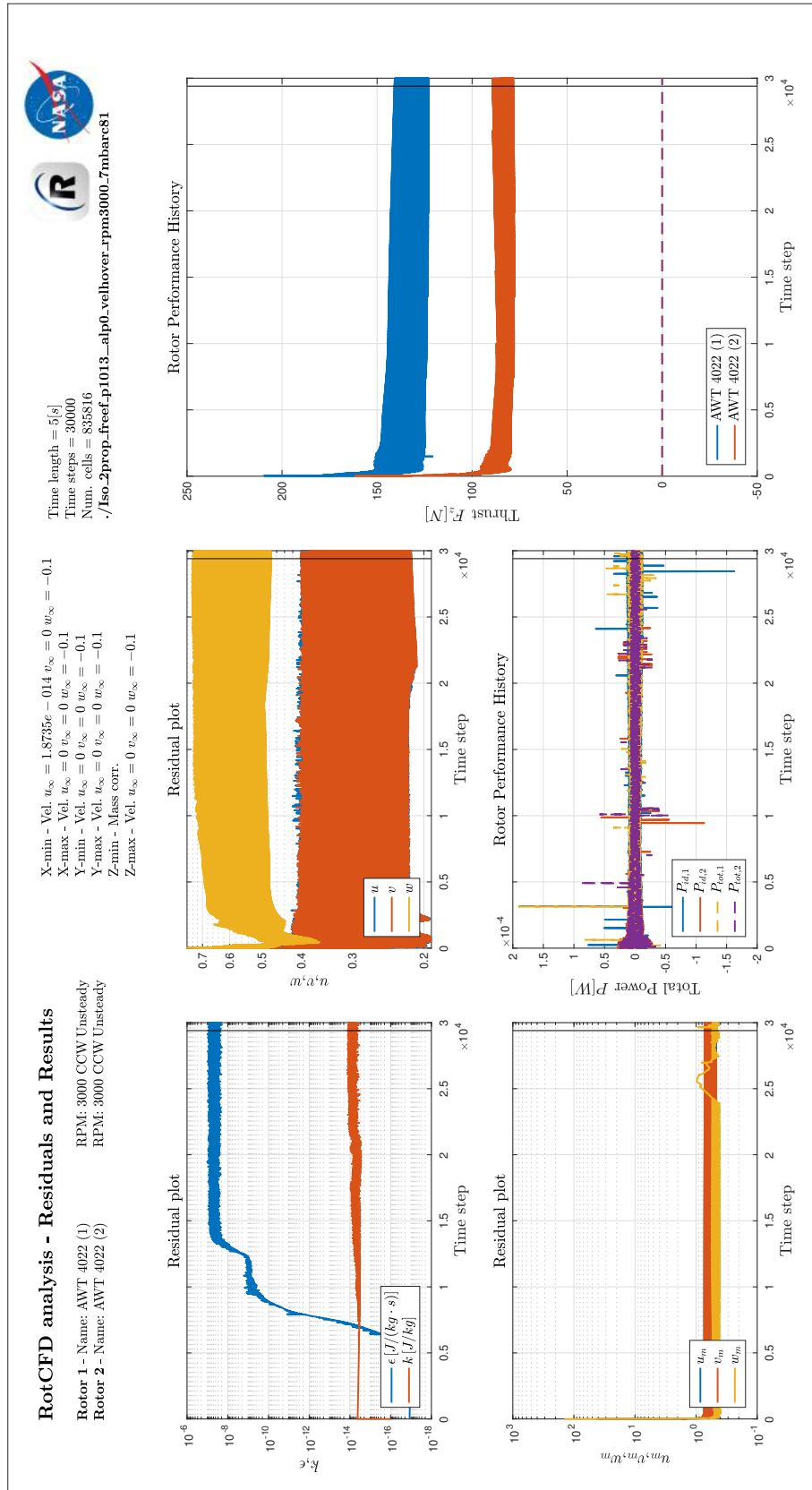


Figure A.8: 2 props, free field,  $p = 1013$  millibar,  $RPM = 3000$ ,  $\alpha = 0^\circ$ , using 7 mbar airfoil tables



# B

## Appendix 2 - Airfoil Tables Validation

Overview of the angle of attacks behaviour along the radius of the blades, rotor one and two respectively, for all simulated RotCFD cases.

### B.1 Free field hover

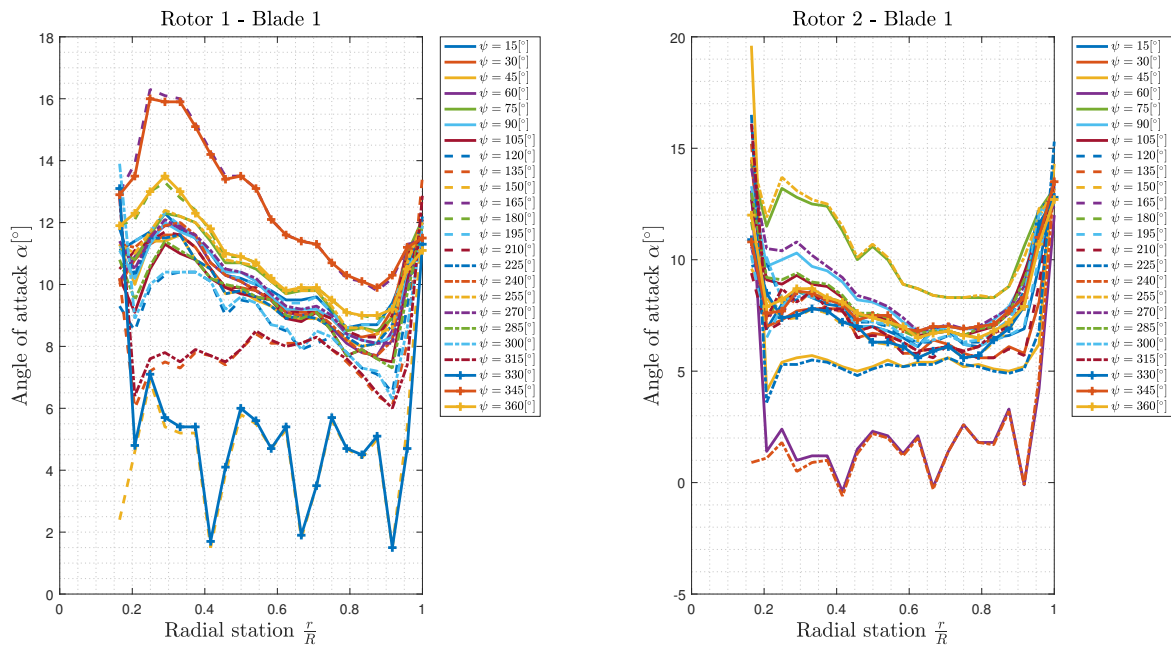


**Figure B.1:** Angle of attack plot for a free field simulation at  $p = 1013$  millibar, 1868 RPM

## B. Appendix 2 - Airfoil Tables Validation

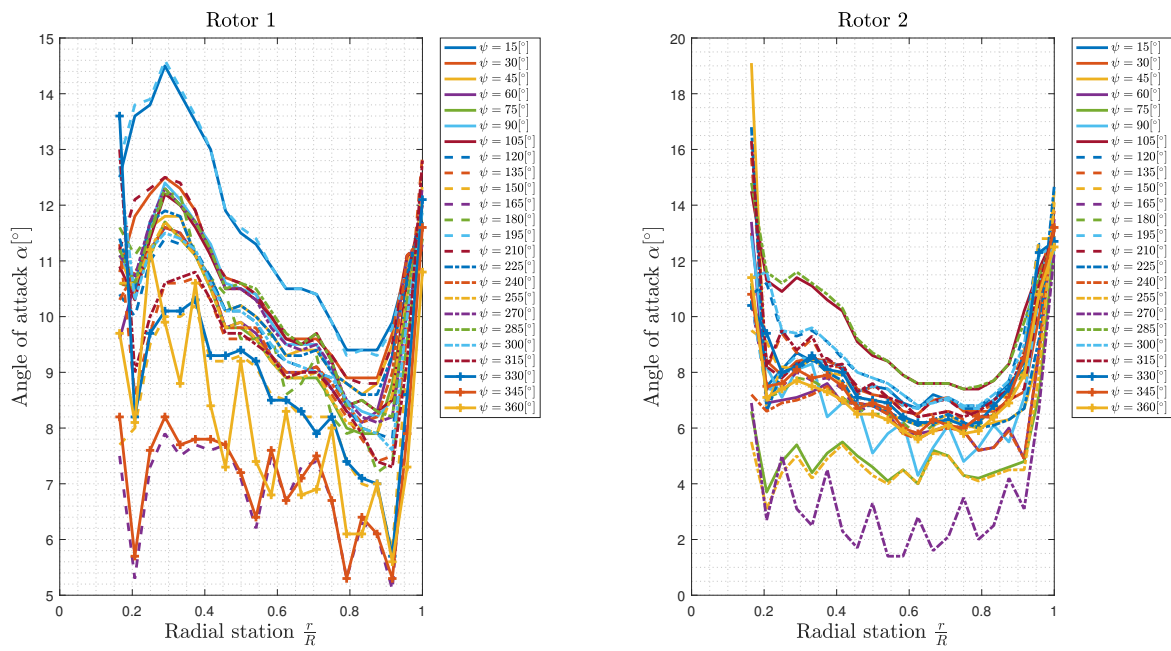


**Figure B.2:** Angle of attack plot for a free field simulation at  $p = 1013$  millibar, 2100 RPM

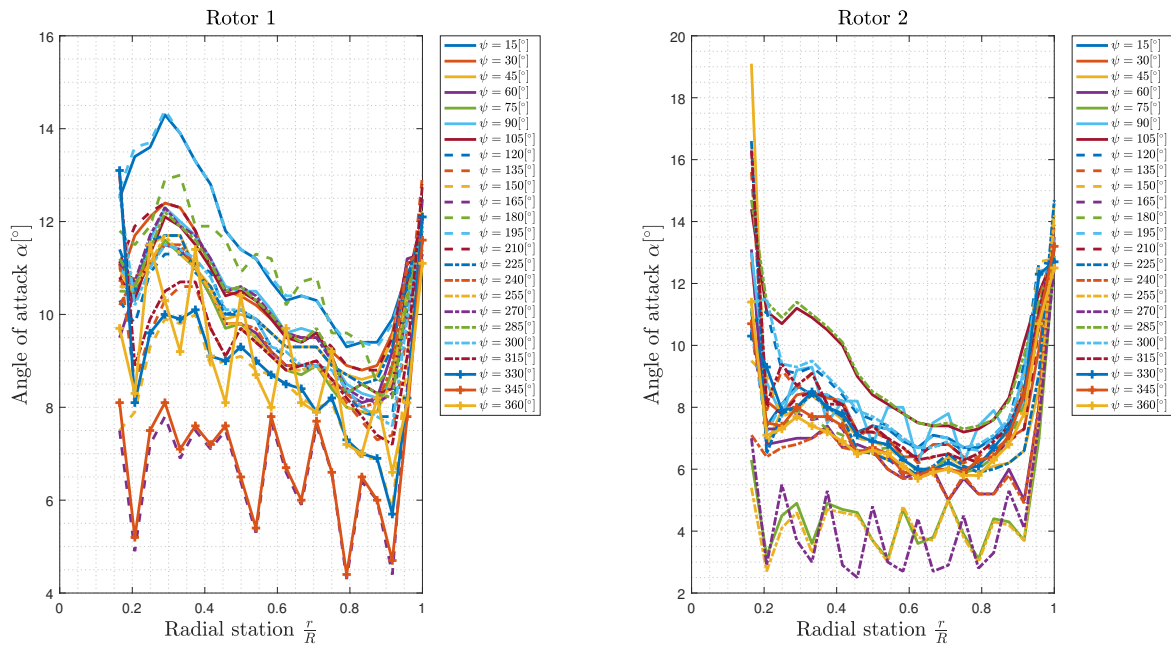


**Figure B.3:** Angle of attack plot for a free field simulation at  $p = 1013$  millibar, 2500 RPM

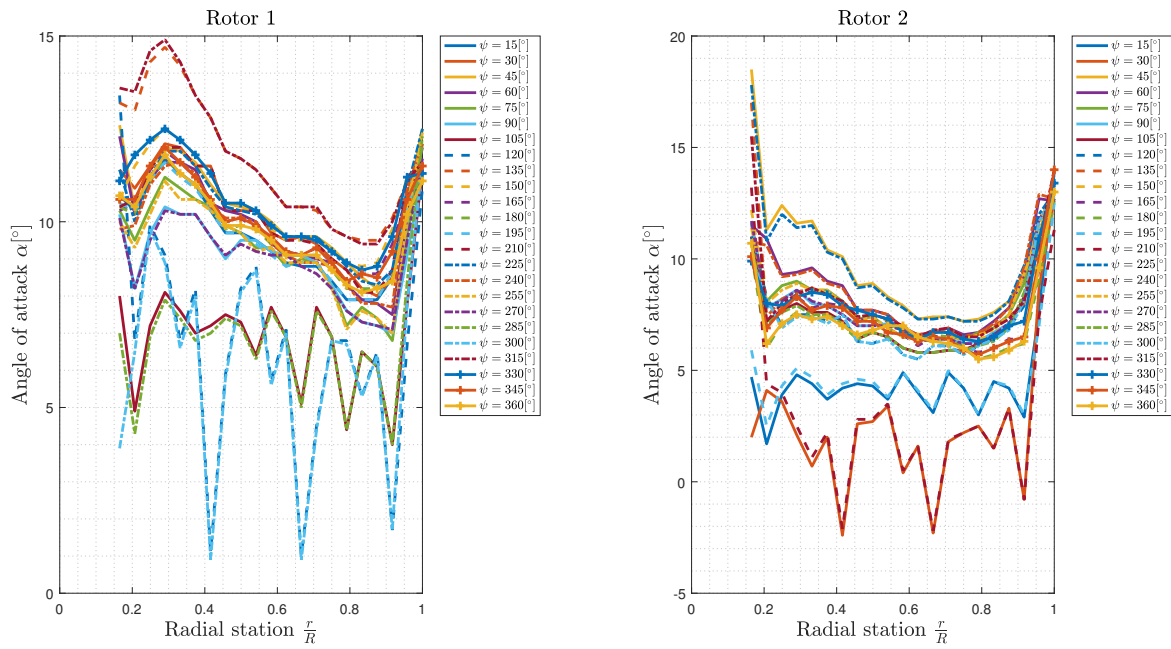


**Figure B.4:** Angle of attack plot for a free field simulation at  $p = 1013$  millibar, 2800 RPM

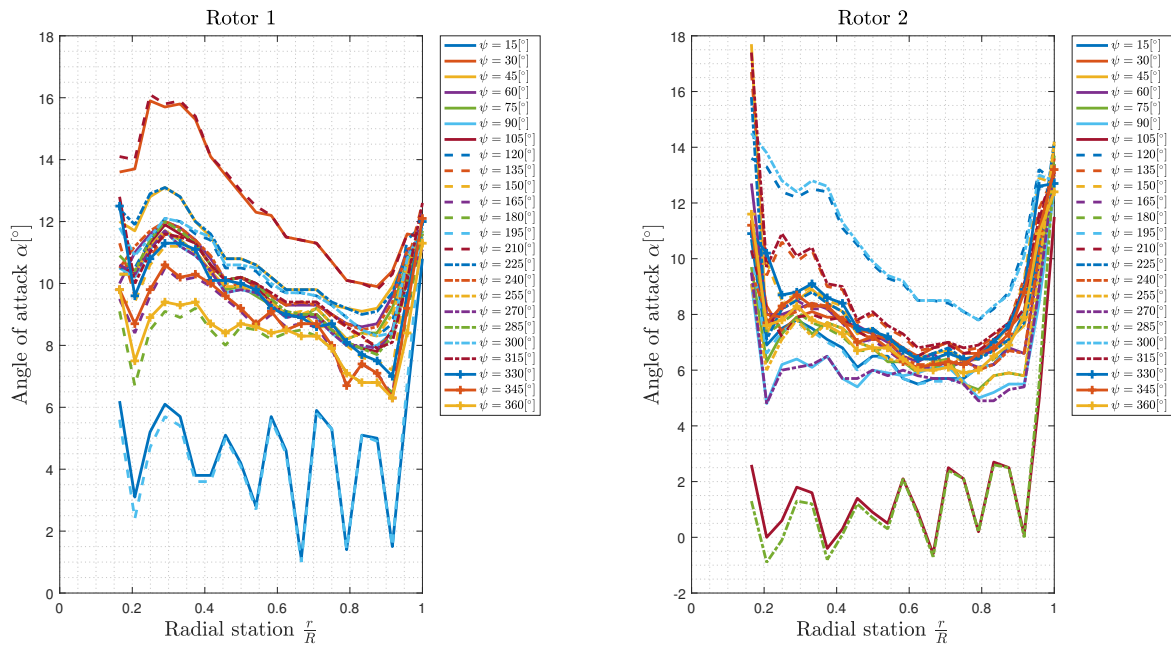


**Figure B.5:** Angle of attack plot for a free field simulation at  $p = 1013$  millibar, 3000 RPM

## B.2 Airfoil comparison

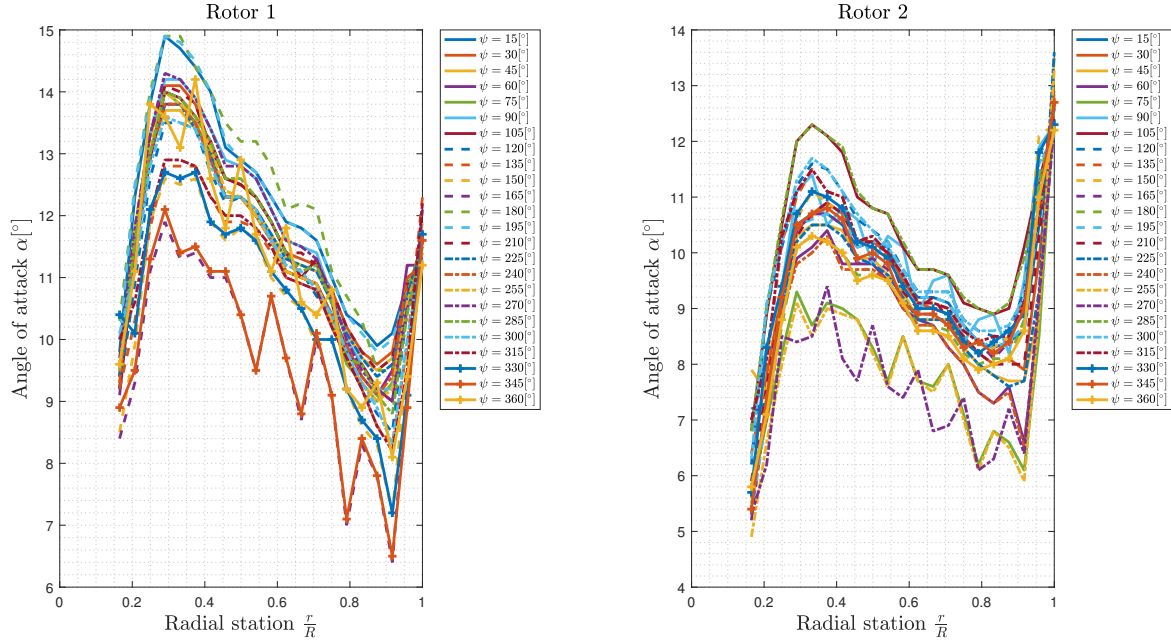


**Figure B.6:** Angle of attack plot for a free field simulation at  $p = 1013$  millibar using 7 millibar airfoil tables, 3000 RPM

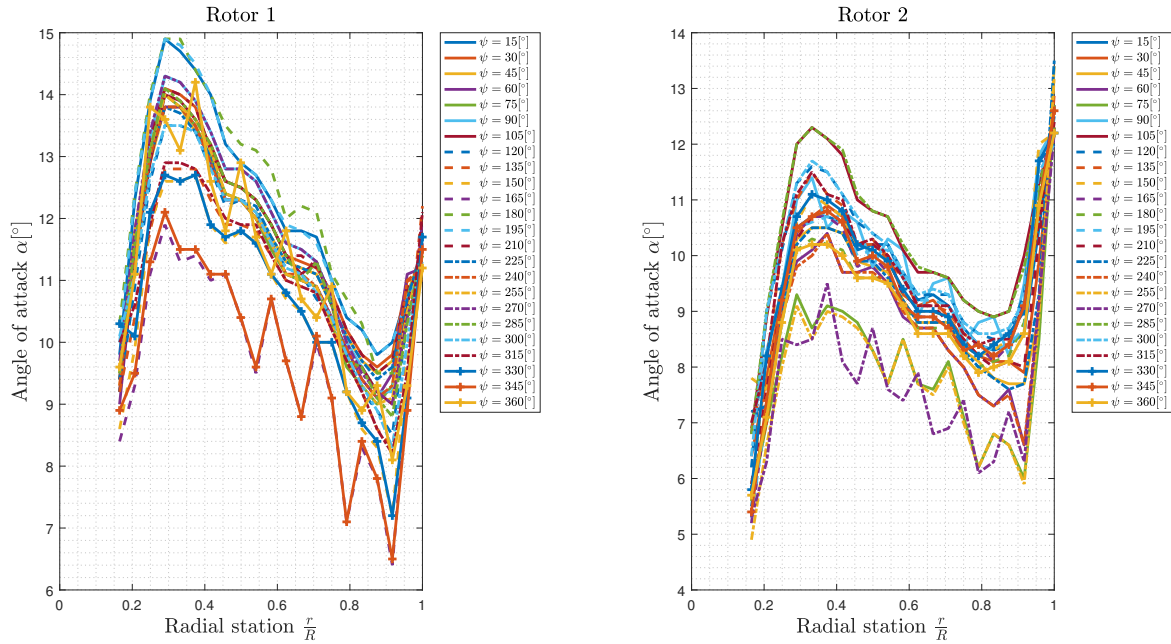


**Figure B.7:** Angle of attack plot for a free field simulation at  $p = 7$  millibar using 7 millibar airfoil tables, 3000 RPM

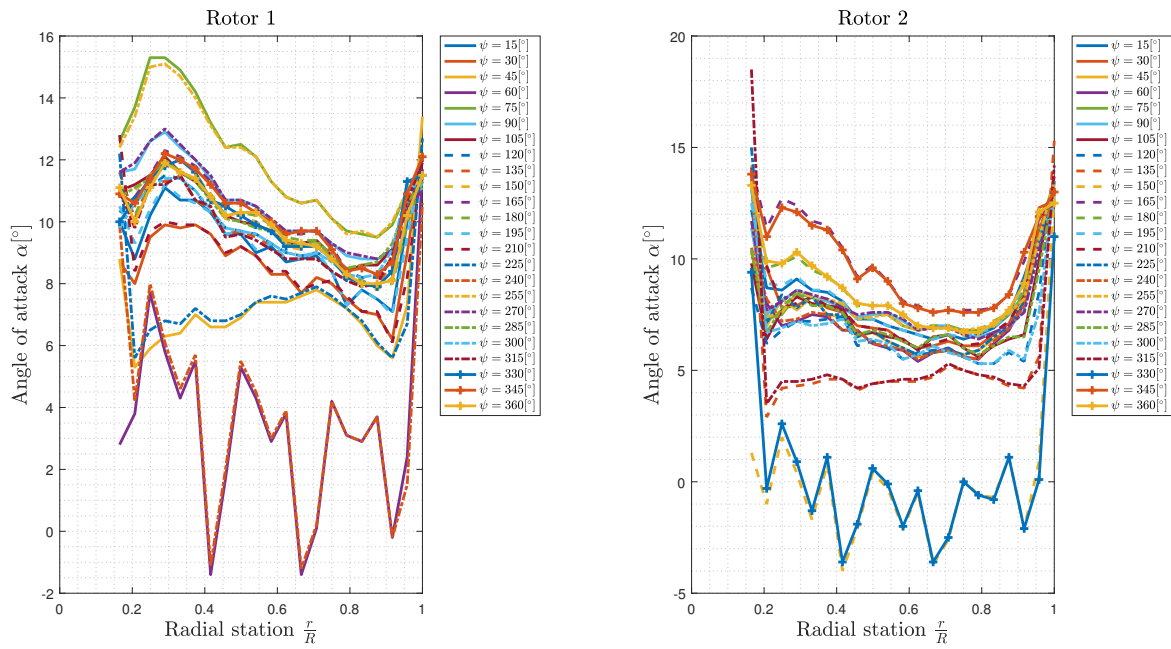


**Figure B.8:** Angle of attack plot for a free field simulation at  $p = 1013$  millibar using 1013 millibar airfoil tables, 3000 RPM

### B.3 Tunnel effects

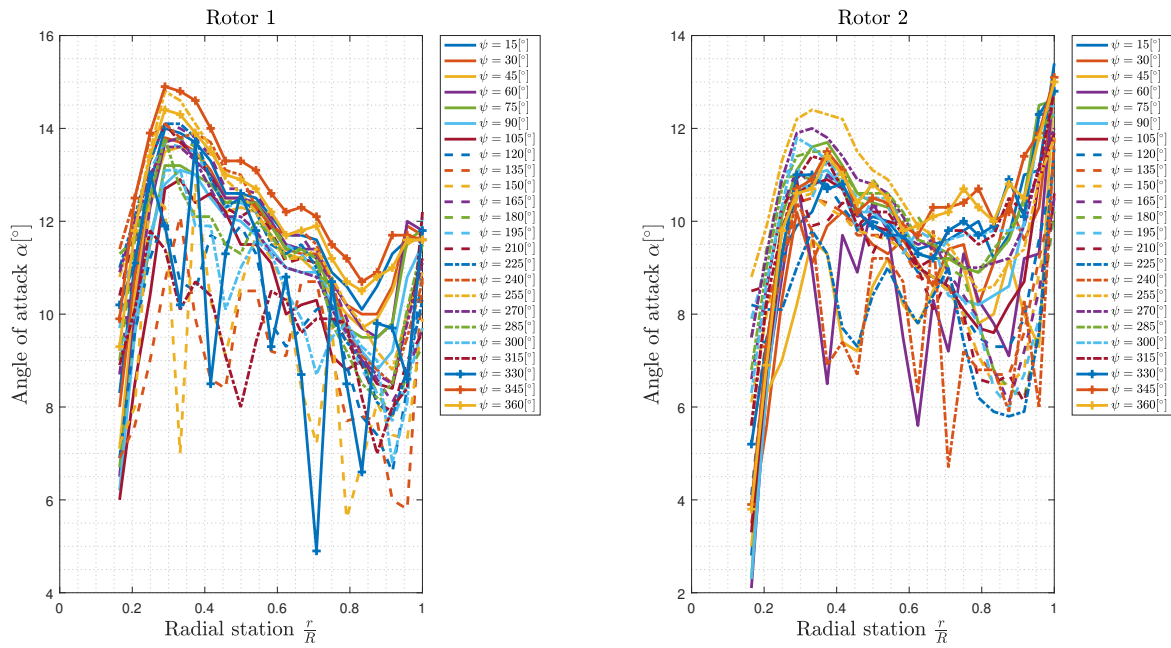


**Figure B.9:** Angle of attack plot for a free field simulation at  $p = 7$  millibar,  $\alpha = 14^\circ$ ,  $V_\infty = 3.5$  m/s, 3000 RPM

## B. Appendix 2 - Airfoil Tables Validation

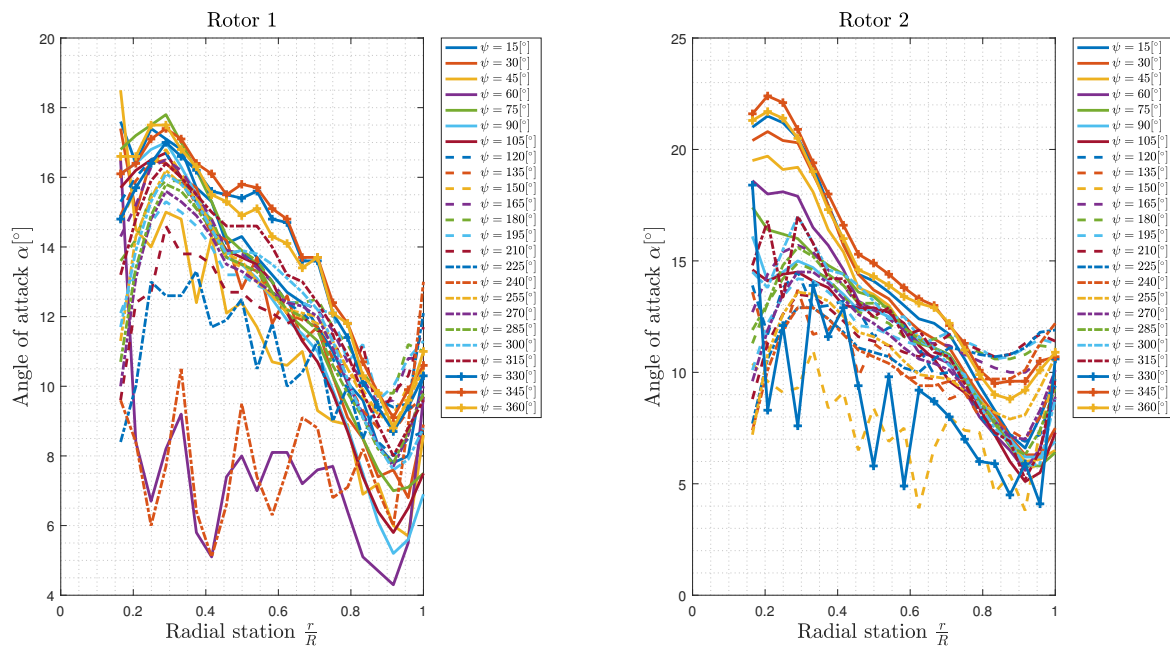


**Figure B.10:** Angle of attack plot for a tunnel simulation at  $p = 7$  millibar,  $\alpha = 14^\circ$ ,  $V_\infty = 3.5$  m/s, 3000 RPM